Doctoral Dissertation

Nanoengineered Bacteria for Cancer Immunotheranostics

SHEETHAL REGHU

Supervisor: Eijiro Miyako

Graduate School of Advanced Science and Technology

Japan Advanced Institute of Science and Technology

Materials Science

September 2023

ABSTRACT

Nanoengineered Bacteria for Cancer Immunotheranostics

Cancer prevalence has reached alarming proportions, impacting people across all genders, ages, and geographic regions. The World Health Organization (WHO) has reported that cancer, as a significant contributor to global mortality, accounts for roughly one out of every six deaths worldwide. The escalating burden of cancer calls for a comprehensive approach that encompasses various facets, including early detection methods, preventive measures, and efficacious treatment strategies. Despite the challenges posed by cancer, notable advancements have been achieved in recent years towards combating this complex disease. The efficacy of traditional cancer therapies in the ongoing fight against cancer is diminishing due to various factors, including the presence of heterogeneity within cancer cells, the development of treatment resistance, the occurrence of significant side effects, and the progression of metastasis. Consequently, there is a substantial demand to explore novel strategies that exhibit reduced toxicity and minimal adverse effects. Additionally, there remains a continuous need for the improvement of existing techniques and the exploration of innovative approaches to overcome these challenges.

Over the past few decades, the utilization of bacterial therapy for cancer treatment has garnered increasing attention and recognition due to its notable efficacy and comparatively reduced incidence of side effects. Despite being a century-old technique, bacterial therapy is currently experiencing a renaissance, gaining significant momentum as a viable approach in the field of oncology. This therapeutic modality encompasses the utilization of bacteria, either in their natural state or after incorporating genetic modifications. Bacterial therapy has emerged as a highly promising avenue in the field of cancer treatment, presenting opportunities for both standalone utilization and synergistic integration with other therapeutic modalities and has successfully advanced to the stage of conducting human clinical trials. Presently, the majority of investigations and genetic modifications in bacterial therapy predominantly focus on pathogenic bacteria, which raises concerns about the potential generation of virulent revertants. Consequently, there exists a pressing necessity to explore the discovery of non-pathogenic strains in order to circumvent these challenges. Promising results have been observed in studies utilizing non-pathogenic probiotic strains as a viable alternative to pathogenic and genetically modified strains. Consequently, further exploration of these bacterial alternatives and the development of novel modification techniques that ensure the preservation of their inherent characteristics become crucial. Hence, the objective of our project is to delve into this unexplored realm and employ chemical modifications to tailor bacteria according to our specific requirements, while maintaining their morphology and functionality unaltered.

The present work proposes the application of non-pathogenic anaerobic bacteria in bacterial therapy, with an emphasis on enhancing their functionality through chemical modifications. The thesis encompasses two major chapters that introduce innovative strategies for chemically modifying bacteria devoid of genetic modifications. These strategies involve the incorporation of specific properties essential for effective tumor targeting and localization, with the goal of improving tumor regression. The modified bacteria were employed in conjunction with photothermal therapy (PTT), synergistically aiming to achieve accelerated and enhanced tumor reduction outcomes. By developing such a system, it aims to effectively induce tumor regression and improve overall treatment outcomes. The findings elucidated in Chapter 2 demonstrate the chemical modification of probiotic bacteria named *Bifidobacterium bifidum* (BB*)* which inherently possesses anticancer properties. In this study, the bacteria were subjected to modifications aimed at enhancing their efficacy in tumor targeting studies. This was accomplished by incorporating a near-infrared (NIR) agent into the bacteria BB, resulting in the formation of modified bacteria that exhibit fluorescence and photothermal conversion efficiency. The desired outcome was achieved by subjecting BB to incubation with indocyanine green (ICG) dye encapsulated in cremophor EL(CRE), followed by subsequent washing. As a result, the bacteria underwent modification as the nanoparticles penetrated through the bacterial membrane, resulting in the modified bacteria, ICG-CRE-BB, which exhibited the desired augmentation in photothermal conversion efficiency. Subsequently, the modified bacteria were subjected to comprehensive characterization, comparing them with their pure form to analyze their altered properties. This was followed by *in-vitro* studies to evaluate their toxicity and anticancer properties. The *in-vitro* investigations demonstrated a significant increase in temperature when subjected to an NIR laser irradiation, along with minimal toxicity in the absence of laser irradiation. Upon exhibiting promising results *in-vitro*, the modified bacteria were subjected to *in-vivo* studies using Colon26 tumor syngeneic models, wherein they were administered via intratumoral injection into the tumor. The tumor treatment involved the synergistic use of modified bacteria and photothermal therapy (PTT), wherein laser irradiation was applied to the solid tumors. Using an NIR fluorescence bioimager, the accumulation of bacteria was observed explicitly in the hypoxic tumor environment. Furthermore, this observation was confirmed through the application of a colony assay. The outcomes

demonstrated the remarkable tumor localization capability of the bacteria, followed by significant tumor regression. This research offers promising prospects for employing biocompatible chemicals in the chemical modification of bacteria for application in cancer therapy. We firmly believe that further refinement and optimization, particularly in the context of anaerobic probiotic strains, holds the potential for clinical studies to explore the utilization of these modified bacteria.

The third chapter shows an alternative method of modification, namely the incorporation of monoclonal antibodies, which represents a groundbreaking strategy garnering significant attention in contemporary therapies. Notably, various types of checkpoint inhibitors have exhibited promising outcomes in accelerating the process of tumor regression. In this project, we expanded upon the modification approach utilized in the previous chapter and extended it to naturally fluorescent purple photosynthetic bacteria (PPSB). To identify the most suitable PPSB strain, extensive screening processes were conducted, evaluating factors such as toxicity, photothermal conversion, and fluorescence and *Rhodopseudomonas palustris* (RP) emerged as the most favorable candidate. Through a process of incubation and subsequent washing, a checkpoint inhibitor, anti-mouse programmed death ligand monoclonal antibody (anti-PD-L1), was covalently attached to RP (which has exhibited excellent efficacy in selectively targeting cancer cells in prior studies) using biocompatible anchor for membrane (BAM). This resulted in the formation of modified RP with anti-PD-L1 (anti-PD-L1–BAM–RP), enabling us to utilize the inherent fluorescence properties of RP in conjunction with the attached checkpoint inhibitor. A series of characterizations were conducted to compare the modified bacteria with their pure counterparts, aiming to identify any discernible differences. Subsequently, *in-vitro* studies were undertaken to investigate the cytotoxicity of both types of bacteria. They were conducted to assess the cytotoxicity of the modified bacteria and pure bacteria and it was observed that the modified as well as the pure bacteria demonstrated low cytotoxicity. Moreover, upon laser irradiation, the temperature elevation observed owing to the inherent fluorescence properties of the bacteria. Encouraging results prompted further evaluation of the modified bacteria in an *in-vivo* setting, with a focus on exploring their targeting effects and tumor regression capabilities. Tumor syngeneic mouse models were employed for this study, and an 808 nm NIR laser was used to irradiate the tumor after bacterial injection. Remarkably, significant tumor reduction was achieved within a short duration, showcasing the efficacy of this non-toxic anaerobic bacteria. Additionally, the precise localization of bacterial tumors was verified through the utilization of a bioimager and a colony assay. We hold the belief that delving into the realm of anaerobic bacteria and augmenting them with synthetic therapeutic materials holds tremendous potential for the development of an ideal combination in bacterial therapy.

In conclusion, we firmly believe that this research on the chemical modification of non-pathogenic bacteria to augment their therapeutic efficacy for application in cancer treatment holds tremendous potential and represents a paradigm-shifting advancement in knowledge. It is imperative that we explore alternatives to the currently employed pathogenic strains and delve into the untapped potential of non-pathogenic anaerobic strains. Our studies have instilled in us a strong belief that this approach has a bright future and the potential to match or even surpass existing therapies. This novel tool can significantly strengthen our arsenal in the fight against this formidable disease.

Keywords: Cancer, bacteria, near infrared, immunotherapy, chemical functionalization, phototherapy, laser

Referee-in-chief: Prof. Dr. Eijiro Miyako

Japan Advanced Institute of Science and Technology

Referees: **Prof. Dr. Kazuaki Matsumura**

Japan Advanced Institute of Science and Technology, Japan

Prof. Dr. Motoichi Kurisawa

Japan Advanced Institute of Science and Technology, Japan

Prof. Dr. Takumi Yamaguchi

Japan Advanced Institute of Science and Technology, Japan

Dr. Alberto Bianco

Centre national de la recherche scientifique (CNRS), France

Table of contents

Contents

List of Tables and Figures

Chapter 1 General Introduction

1.1 Research Interest

Cancer is a critical public health issue with a global impact, and its incidence has been steadily increasing over the years. According to the World Health Organization (WHO) report, cancer is the second biggest cause of mortality, after cardiovascular disease, inflicting about 10 million fatalities in 2020, or nearly one out of every six deaths. Lungs, breast, colorectal, prostate and rectum cancers are the most prevalent types of cancer. Many cancers can be cured if they are diagnosed early and treated properly. The strategy for treatment will vary depending on the type and stage of the disease, as well as the patient's physical condition and other circumstances. Conventional anticancer therapies such as chemotherapy, surgery and radiation therapy are gradually losing their sheen in the battle against cancer, as they face a myriad of shortcomings which have hampered their widespread usage. The resistance, metastasis, heterogeneity, and recurrence of cancer cells to radiotherapy and chemotherapy render many conventional therapeutic approaches redundant against several malignant tumors. The ability of cancer cells to evade the immune response is another reported cause of therapeutic failure.[1] Consequently, these anticancer therapeutic approaches and strategies need to be constantly revised to address the increasing healthcare demands. Over the past few decades, immunotherapy, or the use of immune system components to specifically target and eradicate cancer, has gained significant momentum as a treatment option. Pioneering the idea of leveraging the immune system for this objective dates back more than a century, when a physician named William Coley successfully treated some of his cancer patients with an amalgamation of attenuated and/or live bacteria, controversially known as "Coley's toxins".[2,3] The emergence of synthetic biological techniques has enabled the genetic modification of different bacterial strains to enhance their efficacy in cancer treatment.[4] According to a top-tech engineering perspective, the ultimate goal of cancer therapy is to create miniature,

programmable "robot factories" that can target tumors with precision, navigate autonomously, sense the environment, be easily monitored externally, and respond to external stimuli.[2] Due to bacteria's unique capability to colonize tumors, bacteria therapy has garnered considerable interest.[5]

1.1.1 Bacteria Therapy

Bacteria therapy refers to the application of bacteria as a form of medical treatment for diseases. These are live medications that are injected into patients and can be either genetically modified bacteria strains or naturally occurring bacteria, like probiotics, that possess therapeutic characteristics. Studies are currently being conducted to better understand the advantages and disadvantages of employing bacteria as a medical treatment because this field is relatively unexplored. Probiotics, which are naturally occurring, non-pathogenic bacteria that reside in the human body, are one major topic of investigation. Probiotics are currently being studied for their potential applications in domains such as dermatology and immunology. The use of genetically engineered bacteria is another field of investigation in bacteria therapy. The feasibility of utilizing genetically modified bacteria to selectively target disease-causing entities such as cancers is being investigated by scientists. Preclinical studies have demonstrated the effectiveness of this approach, and ongoing research is now focused on creating safe and reliable bacterial therapies for human use. Besides the aforementioned research fields, scientists are also examining the potential dangers linked with bacterial therapy, such as the risk of infections or other unfavorable consequences. The progress of research in the field of bacteria therapy for cancer treatment over time is depicted in Figure 1.1.

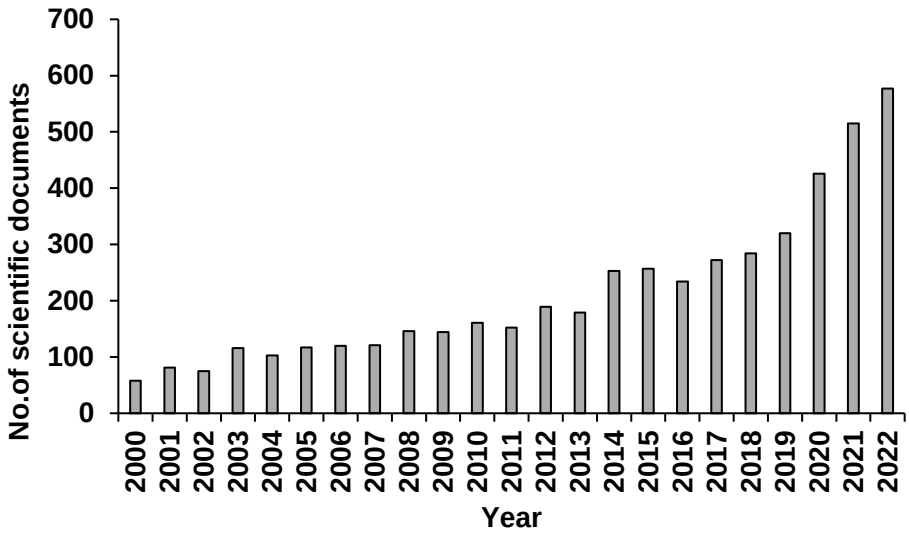

Figure 1.1 Comparison of the number of publications with "bacteria therapy in cancer treatment" in the period 2000-2022 (Data collected in 2023-03 from abstract, title or keywords in Scopus).

Table 1:1 Advantages and disadvantages of bacteria therapy

Advantages	Disadvantages
Reduced occurrence of side effects: Offers the potential to minimize side effects when compared to conventional therapies, mainly chemotherapy.	Safety concerns: Using genetically modified bacteria for therapy may face regulatory challenges and require thorough testing and approval processes.
Personalized treatments: can be customized for each patient, considering their genetic profile and disease characteristics.	Limited knowledge: Complex interactions between bacteria and the human body, including long-term effects and risks, still hold many unknowns.
Versatility: Genetic modification or engineering of bacteria allows for the production and delivery of a spectrum of therapeutic agents	Efficient delivery: Challenges in efficiently delivering viable bacteria to the desired location.
Reduced or negligible impact on healthy cells: By enabling targeted delivery, bacteria therapeutic agents can be transported directly to the affected area, thereby reducing exposure to nearby healthy tissues.	Resistance development: Develop resistance through genetic mutations or acquiring resistance genes.
Combination therapy: can be integrated with other treatment options, including chemotherapy, radiation, and immunotherapy.	Standardization: Maintaining consistent and predictable outcomes by controlling bacteria cell viability for treatment.

1.2 Research background

Certain bacteria are beneficial to human health because of the important function they perform in maintaining homeostasis.[6] Recent studies have identified links regarding changes in bacterial species or their abundance in the body and the emergence and progression of numerous diseases, including gastrointestinal disorders, obesity, and even cancer. [6–9] Natural bacteria have been harnessed both directly and indirectly to treat illness over the course of human history. The massive growth in the field of synthetic material modification and genetic engineering technologies in recent decades has paved the way for strengthening bacterial therapeutics, consequently boosting its potential to treat refractory and incurable diseases.[6,10–12] Numerous bacterial genera, such as *Escherichia, Listeria, Salmonella, Bifidobacterium, Streptococcus, Proteus,* and *Clostridium* have been extensively studied for their unique capacity to selectively gather in tumors and have also been explored as potential anticancer therapeutics.[2] These studies are driven by the goal of utilizing bacteria's tumor-targeting abilities to develop precise and efficient delivery systems for anticancer therapies.

1.3 Objective of this study

The primary objective of this study is to investigate the nanoengineering of bacteria for application in cancer therapy. The aim is to develop a bacterial system that can effectively elicit tumor regression while minimizing or eliminating any undesirable side effects. To mitigate the potential risks associated with the use of pathogenic bacteria, such as *Listeria, Salmonella,* and *Clostridium* strains in bacterial therapy studies, we selected non-toxic, anaerobic bacterial strains that have

exhibited favorable characteristics for chemical modification in our investigations. This study employed a chemical modification approach for the engineering of bacteria, without resorting to genetic manipulations. The process was straightforward, yet highly effective, resulting in the incorporation of key properties such as photothermal conversion efficiency, fluorescence, and potent anticancer activity into the bacterial system. The newly engineered bacteria were subjected to initial anticancer studies *in vitro*, which demonstrated promising results. Subsequently, *in vivo* studies were conducted on tumor mice models, where the bacterial system exhibited excellent tumor regression efficacy. Our goal is to advocate for the utilization of non-toxic bacterial strains in further research and development in this field. We firmly believe that such strains have significant potential as effective tools for cancer therapy and can potentially rival or surpass currently available techniques in terms of efficacy. However, it should be noted that they are currently limited in terms of clinical studies undertaken thus far and further exploration in this area is required.

The thesis is organized into two separate chapters, each elucidating a unique approach to bacteria modification:

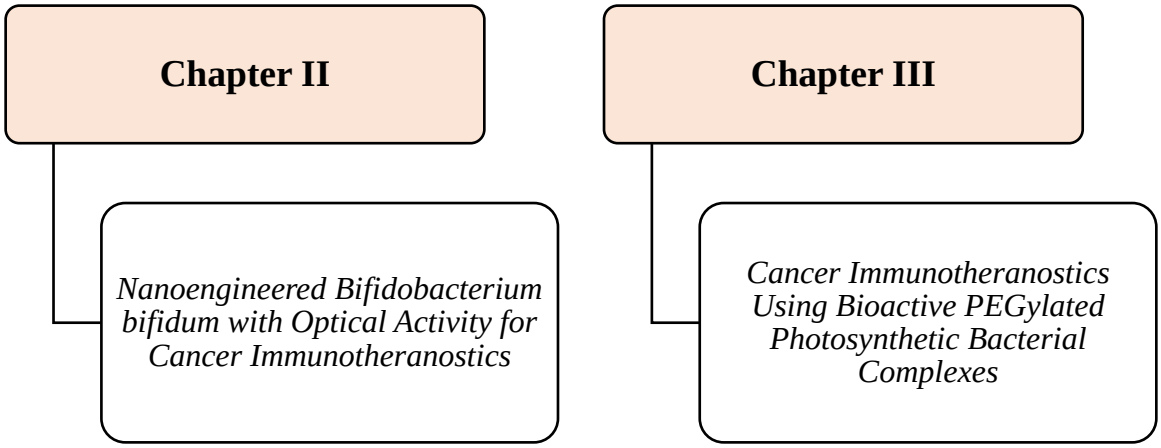

1.4 Future scope

Based on recent research findings, the potential of bacteria therapy as a treatment modality appears highly promising and has demonstrated superiority over other established therapies. Further exploration of certain bacterial species as potential biomarkers for the diagnosis of cancer holds significant promise in the medical field. There is a need to further investigate and advance the development of bacteria that inherently possess anti-cancer properties. Given that most of the bacteria currently employed in cancer therapy are inherently toxic and are being modified genetically to eliminate their harmful effects, the continuous progress in genetic modification may unveil a vast potential for utilizing these bacteria in the treatment of cancer. To prevent the emergence of virulent revertants from genetically modified bacterial strains, it is crucial to investigate non-toxic bacterial strains that possess the ability to treat cancer, and to identify the most appropriate strains for therapeutic use. Recent studies, including our own, have demonstrated effective approaches for utilizing non-pathogenic and non-toxic bacteria in cancer treatment,

achieving comparable outcomes to those observed with toxic strains. Advancements in these approaches might alleviate concerns regarding bacterial toxicity and genetic manipulation, potentially paving the way for safer and more effective cancer therapies. Thorough exploration of this field has the potential to provide paradigm-shifting insights into cancer research, leading to the development of effective treatments that may ultimately bring an end to this debilitating disease.

1.5 References

(1) Yahya, E. B.; Alqadhi, A. M. Recent Trends in Cancer Therapy: A Review on the Current State of Gene Delivery. *Life Sci.* **2021**, *269*, 119087.

(2) Forbes, N. S. Engineering the Perfect (Bacterial) Cancer Therapy. *Nat. Rev. Cancer* **2010**, *10* (11), 785–794.

(3) DeLucia, D. C.; Lee, J. K. Development of Cancer Immunotherapies. *Cancer Treat. Res.* **2022**, *183*, 1 – 48.

(4) Chen, J.; Li, T.; Liang, J.; Huang, Q.; Huang, J.-D.; Ke, Y.; Sun, H. Current Status of Intratumour Microbiome in Cancer and Engineered Exogenous Microbiota as a Promising Therapeutic Strategy. *Biomed. Pharmacother.* **2022**, *145*.

(5) Chen, F.; Zang, Z.; Chen, Z.; Cui, L.; Chang, Z.; Ma, A.; Yin, T.; Liang, R.; Han, Y.; Wu, Z.; Zheng, M.; Liu, C.; Cai, L. Nanophotosensitizer-Engineered Salmonella Bacteria with Hypoxia Targeting and Photothermal-Assisted Mutual Bioaccumulation for Solid Tumor Therapy. *Biomaterials* **2019**, *214*, 119226.

(6) Yu, Y.; Lin, S.; Chen, Z.; Qin, B.; He, Z.; Cheng, M.; Sun, M.; Sun, J. Bacteria-Driven Bio-Therapy: From Fundamental Studies to Clinical Trials. *Nano Today* **2023**, *48*.

(7) Cao, X. Intestinal Inflammation Induced by Oral Bacteria. *Science* **2017**, *358* (6361), 308–309.

(8) Sun, J. Enteric Bacteria and Cancer Stem Cells. *Cancers (Basel).* **2010**, *3* (1), 285–297.

(9) Massier, L.; Chakaroun, R.; Tabei, S.; Crane, A.; Didt, K. D.; Fallmann, J.; von Bergen, M.; Haange, S.-B.; Heyne, H.; Stumvoll, M.; Gericke, M.; Dietrich, A.; Blüher, M.; Musat, N.; Kovacs, P. Adipose Tissue Derived Bacteria Are Associated with Inflammation in Obesity and Type 2 Diabetes. *Gut* **2020**, *69* (10), 1796–1806.

(10) Wu, L.; Bao, F.; Li, L.; Yin, X.; Hua, Z. Bacterially Mediated Drug Delivery and Therapeutics: Strategies and Advancements. *Adv. Drug Deliv. Rev.* **2022**, *187*, 114363.

(11) Watson, A. J. M.; Collins, P. Treatment of Inflammatory Bowel Disease with Genetically Engineered Bacteria. *Gastroenterology* **2010**, *139* (2), 685–687.

(12) Chen, Y.; Liu, X.; Guo, Y.; Wang, J.; Zhang, D.; Mei, Y.; Shi, J.; Tan, W.; Zheng, J. H. Genetically Engineered Oncolytic Bacteria as Drug Delivery Systems for Targeted Cancer Theranostics. *Acta Biomater.* **2021**, *124*, 72–87.

Chapter 2 Nanoengineered Bifidobacterium bifidum with Optical Activity for Cancer Immunotheranostics

2.1 INTRODUCTION

Therapeutic applications in cancer have entered a new age owing to the engineering of living bacteria.[2,13–15] Because of their particular tumor-targeting properties under hypoxic environments and their highly controllable cytotoxicity production, anaerobic bacteria are currently being tested in a number of engineered bacterial treatment clinical studies for cancer.[16] In order to mitigate bacterial toxicity and boost anticancer efficiency, however, complex genetic engineering approaches are used to bacterial treatments, as conventional approaches frequently employ naturally harmful bacteria with minimal medical value, such as *Salmonella typhimurium, Listeria monocytogenes* and *Clostridium novyi.*[2,13–19] Moreover, the creation of potentially pathogenic revertants as a result of genetic modification remains a cause for concern.[20]

Nanotechnological techniques are potential for increasing bacterial therapeutic performance and synergistic properties.[20–23] The potential of bacterial cancer therapy can be considerably increased in particular by photothermal conversion that is dependent on nanotechnological approaches.[24–27] Chen et al., for instance, described the chemical cross-linking of the exterior of the bacterial cell membrane of S. typhimurium using indocyanine green (ICG)-loaded nanoparticles as a photothermal agent for tumor hyperthermia.[5] Nonetheless, traditional nanotechnological techniques continued to use gene editing to reduce toxicity and improve bacterial efficiency. Furthermore, earlier approaches showed that direct anchoring with strong nanoparticles via chemical processes or polydopamine nanocoating on the bacterial cell membrane was required. The viability and natural division of the cells may be hampered by these surface decorations, such as numerous visible nanoparticles or a reasonably dense polydopamine coating on the bacterial membrane. Furthermore, these procedures demand the multistep synthesis of nanoparticles as well

as the alteration of bacterial cells. Hence, the creation of simplified and biologically non-interfering nanofunctionalizations of non-pathogenic natural bacteria, which do not require complex genetic alterations, is of great value for nanotechnology-based transformative bacterial cancer treatments.

There is a great deal of interest in employing nanotechnology to investigate and remotely regulate immune responses.[28–30] Accordingly, functional nanoparticles have been developed for the extended release of immunotherapeutic medicines, thereby enhancing a number of immunostimulatory effects. The ability of nanoparticles to specifically target tumors falls short in achieving the necessary anticancer efficacy when relying solely on immune cells. The efficacy of immunotherapy using conventional nanoparticle technologies is primarily influenced by improved penetration and retention effects, as well as biomarker-dependent ligand-receptor interactions. The integration of functional nanoparticles with bacteria therapy could be a game changer for extremely tumor-specific immunostimulatory control.[27,31] To properly manage immunological activities for therapies, the main challenges at the present are to investigate simpler nanofunctionalizations with nonpathogenic natural bacteria and new nanomicrobial technologies.

In this research, we establish a practical approach for the development of nanoparticle-functionalized bacteria for photothermal immunotherapies. By the usage of a biologically penetrable near-infrared (NIR) laser, the developed ICG encapsulating Cremophor EL (CRE) nanoparticles could be utilized to effectively "nanoengineer" nonpathogenic *Bifidobacterium* for cancer optotheranostics. (Figure 2.1a). Unique optical absorbance and fluorescence characteristics, excellent biocompatibility, robust photothermal conversion, remarkable tumor selectivity, and powerful anticancer activity were all displayed by optically activated functional bacteria. In addition to the tumor-targeting efficacy of bacteria, the NIR fluorescence (FL) of

light-induced functional bacteria aided fluorescent tumor detection. With the aid of immune responses, this approach could be employed efficiently to eradicate colorectal cancer cells in mice.

2.2 Materials and Methods

2.2.1 Bacterial strains and growth

The bacterial strain utilized in this research was acquired from the National Institute of Technology and Evaluation Biological Resource Center (NBRC; Chiba, Japan). *Bifidobacterium bifidum* (BB; NBRC 100015) was grown in NBRC medium no. 385 at a temperature of 37 ^{o}C while ensuring anaerobic conditions. All reagents necessary for bacterial culturing were acquired from FUJIFILM Wako Pure Chemical (Osaka, Japan).

2.2.2 Preparation of nanoengineered bacteria

Indocyanine green (ICG, 1 mg/mL; Tokyo Chemical Industry, Tokyo, Japan), Nile Red (NR, 1 mg/mL; Tokyo Chemical Industry, Tokyo, Japan), or 4,4- difluoro-4-bora-3a,4a-diaza-s-indacene (BODIPY, 1 mg/mL; Sigma-Aldrich, St. Louis, MO, USA) was dissolved in PBS with 5% cremophor EL (Nacalai Tesque, Kyoto, Japan) using sonication to obtain ICG–CRE, NR–CRE, and BODIPY–CRE. NR–CRE and BODIPY–CRE suspensions were filtered (0.45 μm-polytetrafluoroethylene syringe filter, Osaka Chemical, Osaka, Japan). The medium containing BB was centrifuged at 2,300 × g for 5 min within a temperature range of 4–15 °C, followed by washing with PBS. Subsequently, the concentration of the bacterial suspension was adjusted to 2 × 10^9 CFU/mL and subjected to centrifugation. Then ICG–CRE (ICG concentration = 1 mg/mL), NR–CRE (NR concentration ~ 0.5 μg/mL), or BODIPY–CRE (BODIPY concentration ~ 3.7 μg/mL) was added to the bacterial pellet, and the resulting cell suspension was incubated at a

temperature of 37 °C overnight. After overnight incubation, the samples were centrifuged to eliminate any unbound dye molecules, and the modified bacterial cells were subsequently re-suspended in PBS. The viability of nanoengineered bacteria was assessed using both a bacterial counter (DUAA01NP- H; PHC, Tokyo, Japan) and an active colony assay.

2.2.3 Optical characterizations

The absorbance spectra of the bacterial solutions were measured at a temperature of 20 °C using a UV–Vis–NIR spectrophotometer (V-730 BIO; Jasco, Tokyo, Japan). The fluorescence of bacterial dispersions was quantified using a fluorescence spectrometer (FP-8600 NIR Spectrofluorometer; Jasco, Tokyo, Japan). Amount of loaded and internalized ICG into bacteria was determined by measuring the collected supernatant of washed BB after modification of ICG–CRE using a UV–Vis–NIR spectrophotometer.

2.2.4 Structural characterizations

High-resolution TEM (H-7600; Hitachi, Tokyo, Japan) operating at an acceleration voltage of 100 kV was employed to visualize the morphology and structure of ICG–CRE, ICG–CRE–BB, and BB. This was accomplished through the utilization of negative staining. TEM observations were performed by the Hanaichi Ultra Structure Research Institute Co., Ltd. (Aichi, Japan).

2.2.5 Photothermal conversion tests

Bacterial dispersions (100 μL) or PBS buffer (100 μL) (FUJIFILM Wako Pure Chemical) were subjected to irradiation using an 808 nm NIR laser (CivilLaser, Hangzhou, Zhejiang, China) at 1.2 W (~ 61.1 mW/mm^2; spot diameter, approximately 5 mm), 0.6 W (~ 30.6 mW/mm^2), or 0.3 W (~ 15.3 mW/mm^2) under the indicated conditions. The temperature of the solutions was measured in real time using a temperature sensor (AD-5601A; A&D, Tokyo, Japan).

2.2.6 Cell culture and cell viability assays

Murine colon carcinoma (Colon26) and human normal diploid fibroblast (MRC5) cell lines were acquired from the Japanese Collection of Research Bioresources Cell Bank (Tokyo, Japan). Murine macrophage cell line (RAW264.7) was procured from Riken Bio Resource Center (Ibaraki, Japan). The Colon26 cell line was cultured in Roswell Park Memorial Institute (RPMI) 1640 medium (Gibco, Grand Island, NY, USA) containing 10% fetal bovine serum (FBS), 2 mM L-glutamine, 1 mM sodium pyruvate, gentamycin, and penicillin-streptomycin (100 IU/mL). MRC5 and RAW264.7 cells were cultured in Dulbecco's modified Eagle's medium (DMEM, Gibco, Grand Island, NY, USA) containing 10% FBS, 2 mM l-glutamine, 1 mM sodium pyruvate, gentamycin, penicillin-streptomycin (100 IU/mL), and Hank's balanced salt solution (Life Technologies, Carlsbad, CA, USA). The cells were maintained at 37 °C in a humidified chamber containing 5% CO_2 and were cryopreserved in multiple vials using liquid nitrogen. Cell viability was assessed using a Cell Counting Kit (CCK-8; Dojindo Laboratories, Kumamoto, Japan) according to the manufacturer's instructions. Briefly, cells (7×10^3 cells/well) were seeded in 96-well plates and allowed to adhere overnight. Subsequently, the cells were then subjected to bacteria exposure and laser irradiation, as indicated. Following a washing step using fresh medium, the cells were subjected to incubation with the CCK-8 solution at a temperature of 37 °C for 3 h. Absorbance at 450/690 nm was then assessed using a microplate reader (Infinite 200 PRO M Plex; Tecan, Männedorf, Switzerland).

2.2.7 In vitro cytotoxicity of bacteria

To assess the in vitro cytotoxicity of BB, CRE–BB, and ICG–CRE–BB, normal human cells (MRC5) or cancer cells (Colon26) were seeded overnight in 96-well plates at a density of 7×10^3 cells/well. The various bacterial suspensions were co-cultured with these adhered cells for a duration of 24h. Afterwards, cells were washed with fresh medium and the viability was assessed using a CCK-8 kit following the previously described method.

2.2.8 Laser-induced cytotoxicity

The Colon26 or MRC5 cells were seeded in 96-well plates at a density of 7×10^3 cells/well. After adhering overnight, the cells were subjected to treatment with PBS (100 μL) containing BB, CRE–BB, ICG–CRE, or ICG–CRE–BB with 808 nm laser irradiation at a power of 1.2 W (~ 61.1 mW/mm^2) for a duration of 3 min. Concentrations of ICG and BB were approximately adjusted to 22.9 μg/mL and 1.0×10^9 CFU/mL, respectively. The control (PBS without bacteria) was also irradiated. Throughout the laser irradiation process, the temperature of a cells-seeded plate with nanoengineered bacteria was placed in an incubator, where the temperature was carefully maintained at 37 °C. Following the completion of laser irradiation, the bacteria were thoroughly washed away, after which the cells were sub-cultured with fresh medium and incubated for another 24 hours. Subsequently, cell viability was assessed using the CCK-8 kit.

2.2.9 Fluorescence microscopy imaging

The BB, CRE–BB, or ICG–CRE–BB bacterial solutions (10 μL, 1×10^9 CFU/mL) was plated on a glass coverslip (AGC Techno Glass, Shizuoka, Japan) and then observed using a fluorescence microscopy system (IX73) and cellSens V3.1 software (Olympus) equipped with a mirror unit

(IRDYE800-33LP-A-U01; Semrock, Lake Forest, IL, USA) and an objective (×40 magnification, aperture 0.95; UPLSAPO40X, Olympus) at 20 °C.

2.2.10 Confocal laser scanning microscopy

The NR–CRE–BB, BODIPY–CRE–BB, or BB bacteria solution (1 mL, 1×10^9 CFU/mL) was incubated in a poly-L-lysine coated glass bottom dish (Matsunami Glass Industry, Osaka, Japan) for 30 min at 20 °C. The bacteria underwent five washes with PBS buffer (1 mL) and were observed at 20 °C using a confocal laser scanning microscopy (FV-1000, Olympus) through an objective (×100 magnification, aperture 1.35; UPLANSAPO100XS, Olympus). The images were examined by FluoView V4.2 software (Olympus).

2.2.11 In vivo phototherapy

The animal experiments were carried out following the approved protocols by the Institutional Animal Care and Use Committee of JAIST (No. 01-002). Female BALB/cCrSlc mice (n = 12; 4 weeks old; average weight = 15 g) were obtained from Japan SLC (Hamamatsu, Japan). Mice bearing the Colon26 cell-derived tumors were generated by injecting culture medium/Matrigel (Dow Corning, Corning, NY, USA) mixture (v/v = 1:1; 100 μL) containing 4×10^6 cells into the left and right flanks of the mice. Once the tumor volumes reached approximately 400 mm^3 after a duration of around 2 weeks, the mice were administered intratumoral injections of PBS (100 μL) or PBS containing bacteria (100 μL; 5.0×10^8 CFU) or ICG–CRE (100 μL). Concentrations of ICG and BB are approximately 45.8 μg/mL and 2.0×10^9 CFU/mL, respectively. The tumors located on the right flank were irradiated for 3 min on alternate days (a total of six times) using the 808 nm laser (713 mW, 36.3 mW/mm^2) after sample injection. Using a clamp, the laser beam was directed towards the center of the solid tumor. During the irradiation process, thermographic

measurements were performed using IR thermography (i7; FLIR, Nashua, NH, USA). Tumor development and overall health (body weight and viability) were monitored on alternate days. Additionally, the tumor volume was estimated using the equation: $V = L \times W^2/2$, where L and W denote the length and width of the tumor, respectively. Upon reaching a tumor volume exceeding 2,000 mm^3 on either side of the mice, which was determined as the endpoint, the mice were euthanized following the guidelines of the Institutional Animal Care and Use Committee of JAIST.

2.2.12 Fluorescent bio-imaging

To monitor the chronological changes in FL intensity caused by the tumor targeting effect of ICG–CRE–BB in mice, Colon26 tumor-bearing mice (female; 7 weeks; n = 4; average weight = 18 g; average tumor size = 400 mm^3; BALB/cCrSIc; Japan SLC) were injected intratumorally or intravenously with PBS containing ICG–CRE–BB (100 μL, 5×10^8 CFU) or PBS alone. The mice were euthanized, and the major organs, including heart, liver, spleen, lung, kidney, and tumor, were imaged using an in vivo fluorescence imaging system (VISQUE™ InVivo Smart-LF, Vieworks, Anyang, Republic of Korea) with a 3 sec exposure time and ICG filter (Ex, 740–790 nm; Em, 810–860 nm) at 0.5, 3, 24, 48, 72, and 96 h post-injection. The FL images were acquired and analyzed using CleVue™ software (Vieworks).

2.2.13 Biodistribution of nanoengineered bacteria in tumor model

The Colon26 tumor-bearing mice (female, 7 weeks; n = 4; average weight = 18 g; average tumor size ~400 mm^3; BALB/cCrSIc; Japan SLC) were intravenously injected in the tail vein with culture medium (100 μL) containing ICG–CRE–BB (1×10^7 CFU/mL) or PBS (100 μL). After 120 h, the organs and tumors were carefully excised and weighed. After homogenizing thoroughly with a homogenizer pestle in 1 mL of PBS solution at 4 °C, the mixture was shaken for 20 min at a speed

of 380 rpm/min at 15 °C. The supernatant was serially diluted with PBS 10^2 time or 10^3 times, and each dilution mixture was individually plated (50 μL) onto an a Trypticase–Phytone–Yeast (TPY) agar plate. The TPY medium (per liter) contained 10 g of trypticase [Becton, Dickinson and Company (BD), Franklin Lakes, NJ, USA], 5 g of peptone (Sigma-Aldrich), 5 g of glucose (FUJIFILM Wako Pure Chemical), 2.5 g of yeast extract (BD), 1 mL of Tween 80 (FUJIFILM Wako Pure Chemical), 0.5 g of L-cysteine (FUJIFILM Wako Pure Chemical), 2 g of K2HPO4 (FUJIFILM Wako Pure Chemical), 0.5 g of $MgCl_2 \cdot 6H_2O$ (FUJIFILM Wako Pure Chemical), 0.25 g of $ZnSO_4 \cdot 7H_2O$ (FUJIFILM Wako Pure Chemical), 0.15 g of $CaCl_2$ (FUJIFILM Wako Pure Chemical), and 0.03 g of $FeCl_3$ (FUJIFILM Wako Pure Chemical). TPY agar is the TPY medium supplemented by agar in a concentration of 15 g/L. The pH value of the medium was around pH 6.0. The inoculated agar plates were anaerobically incubated for 1 day at 37 °C and the formed bacterial colonies were imaged and were manually counted.

2.2.14 Immunohistochemistry staining of tumor tissues

The Colon26 tumor-bearing mice were euthanized the day after the administration of intratumoral injection of PBS (100 μL), BB (100 μL, 5×10^8 CFU), CRE–BB (100 μL, 5×10^8 CFU), or ICG–CRE–BB (100 μL, 5×10^8 CFU), and laser irradiation. The control groups were not irradiated. Thereafter, the tumor tissues from the different treatment groups were harvested for IHC staining. The IHC analysis was performed by Biopathology Institute Co., Ltd. (Oita, Japan) using standard protocols. Briefly, primary tumors were surgically removed, fixed in 10% formalin, processed for paraffin embedding, and cut into 3–4-μm-thick sections. After incubation with primary antibodies (listed in Table 2.1), the sections were stained with hematoxylin and examined using light microscopy (IX73).

Table 2:1 Antibodies used in this study

Antibody	Type	Source	Catalog No.	Application
F4/80	Mouse Monoclonal	BMA Biomedicals	T-2028	IHC (1:50)
CD3	Rabbit Monoclonal	Abcam	ab16669	IHC (1:100)
Caspase-3	Rabbit Polyclonal	Cell Signaling Technology	9661S	IHC (1:100)
TNF-α	Rabbit Polyclonal	Abcam	ab6671	IHC (1:100)
Anti-digoxigenin-peroxidase	Sheep Polyclonal	Merck Millipore	S7100	Tunel

2.2.15 In vitro TNF-α expression

The concentration of expressed TNF-α was measured using RayBio® Mouse TNF-alpha ELISA kit (RayBiotech, Norcross, GA) according to the manufacturer's instructions. Briefly, RAW264.7 cells (4×10^4 cells/mL) were seeded in 24-well plates and allowed to adhere overnight. The cells were then exposed to bacteria and laser irradiation, as indicated. After collecting samples from wells, each sample was carefully centrifuged to remove bacteria, and their supernatants were further used for ELISA assay. Absorbance at 450 nm was then determined using a microplate reader. Lipopolysaccharides from Escherichia coli O157 (FUJIFILM Wako Pure Chemical) was used as a positive control.

2.2.16 Blood tests

The CBC and biochemical parameters were investigated by the Japan SLC and Oriental Yeast Co., Ltd (Tokyo, Japan). The tail vein of BALB/cCrSlc mice (female, 10 weeks; n = 5; average weight = 21 g; Japan SLC) was injected with PBS containing BB (200 μL, 1×10^6 CFU), CRE–BB (200 μL, 1×10^6 CFU), ICG–CRE–BB (200 μL, 1×10^6 CFU), or PBS (200 μL). After 30 days, blood samples were collected from the inferior vena cava of these mice.

2.2.17 Statistical analysis

All experiments were conducted in triplicates and repeated three or more times. Quantitative values were expressed as the mean ± standard error of the mean (SEM) of at least three independent experiments. Statistical differences were analyzed using Student's two-sided t-test and one-way or two-way analysis of variance (ANOVA).

2.3 RESULTS AND DISCUSSION

2.3.1 Characterizations of nano-engineered bacteria

Due to their remarkable tumor targeting abilities, *Bifidobacterium* strains, such as *Bifidobacterium bifidum* (BB) and *Bifidobacterium longum*, have often been utilized as effective microbial tools, such as drug delivery systems in hypoxia-driven tumor biotherapy.[32,33] In fact, live anaerobic bacteria including *Bifidobacterium* strains, employ distinctive mechanisms to specifically target solid tumors.[2,13,14] Upon systemic administration, therapeutic bacteria distribute to both tumor and healthy tissues. Nevertheless, bacteria present in the bloodstream and other normal tissues are eliminated, whereas those residing in the tumor persistently proliferate, often reaching significantly higher numbers of colony-forming units compared to the initially administered dosage, owing to their preference for a hypoxic environment. The selective colonization of bacteria in solid tumors is believed to be influenced by the immunosuppressive and biochemically distinct microenvironment that arises due to pathological alterations associated with these tumors. While *Bifidobacterium* strains normally necessitate genetic manipulation using synthetic plasmids to acquire anticancer properties, these strains demonstrate inherent high tumor-targeting efficacy and low toxicity, without the requirement for genetic manipulations. Hence, natural BB was selected as the model platform for nanoengineering. Figure 2.1b and c show a schematic illustration of the

preparation of nanoengineered BB. Among the numerous attractive photothermal converters available,[34–36] ICG was chosen as the model photoactivatable reagent due to its status as an Food and Drug Administration (FDA)-approved NIR fluorescent agent.[37]

Furthermore, NIR light-activatable ICG has found widespread use in clinical settings for a variety of biomedical applications, including diagnosis and phototherapies. This is primarily attributed to its exceptional transparency within the optical wavelength range, allowing effective penetration through biological tissues. Nonetheless, ICG tends to agglomerate within physiological environments, such as aqueous buffered solutions and blood serum, due to its anionic and hydrophobic nature. The tendency of IGG to agglomerate in physiological environments, despite its powerful optical properties as an NIR agent, frequently hinders its desired biomedical applications. Thus, we nanoformulated ICG using 5% CRE to avoid its aggregation in aqueous PBS solution during its internalization into the bacteria cells. Additionally, CRE, an FDA-approved amphiphilic synthetic polymer (polyoxyethylene castor oil derivative), is commonly employed as a drug delivery carrier for several poorly water-soluble molecules.[37,38]

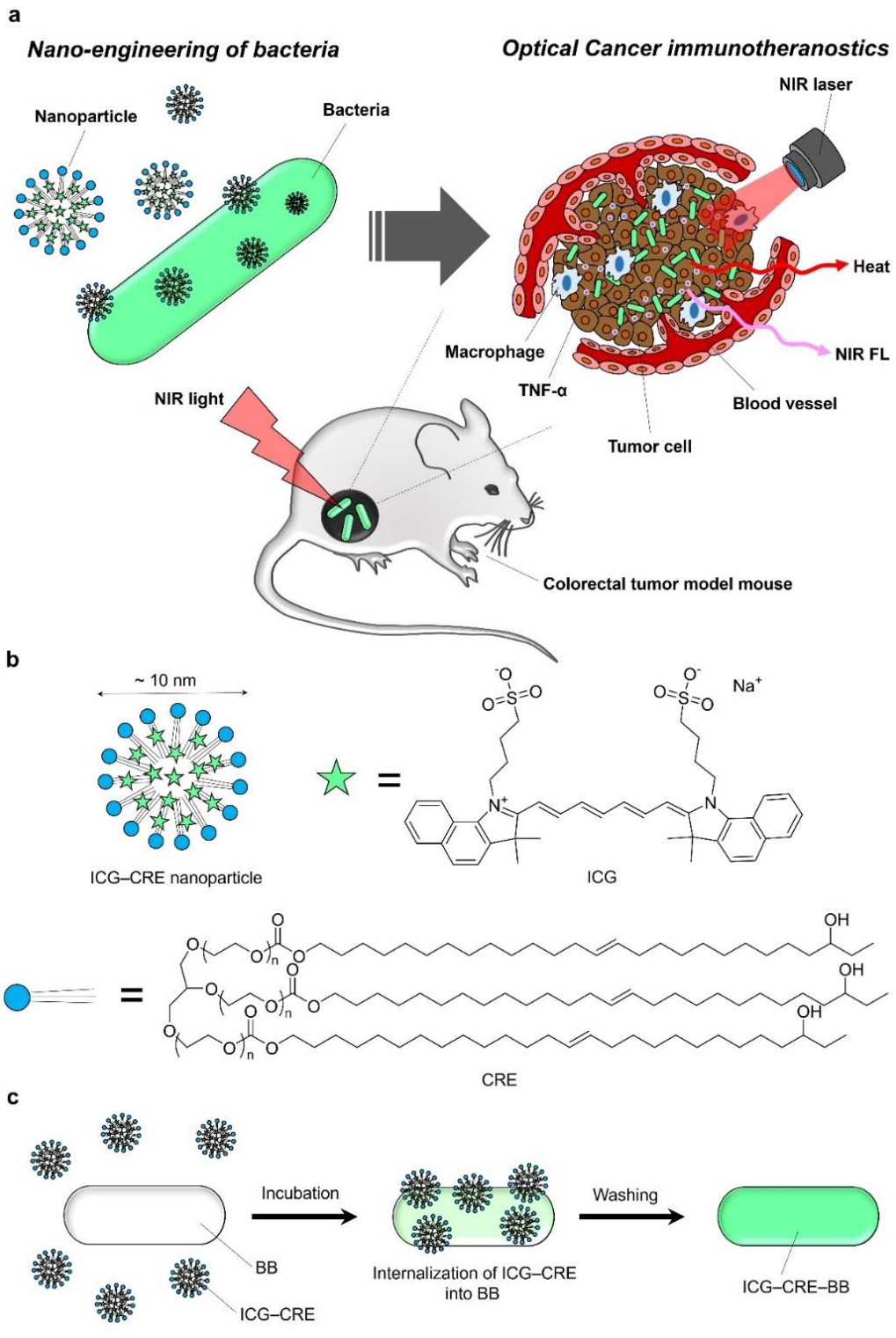

Figure 2.1 (a) Concept of nanoengineered bacteria with optical activity for photothermal cancer immunotheranostics. (b) Schematic illustration of ICG−CRE nanoparticle. (c) Scheme of ICG−CRE−BB synthesis.

CRE nanoparticles encapsulating ICG molecules (ICG−CRE) can be spontaneously synthesized by a straightforward one-step sonication process because of the self-assembly nature of amphiphilic CRE molecules (Figure 2.1b and Figure 2.2). ICG−CRE-functionalized BB (ICG−CRE−BB) can also be easily prepared in only two steps, namely incubation and washing processes (Figure 2.1c). Flexible soft nanoparticles are possibly transportable through the bacterial cell membrane.[39,40]As expected, the synthesized ICG−CRE showed as a transparent greenish-colored solution (Figure 2.2a, right vial), while ICG alone formed visible aggregations in PBS after being incubated at 20 °C for several minutes (Figure 2.2 left vial).

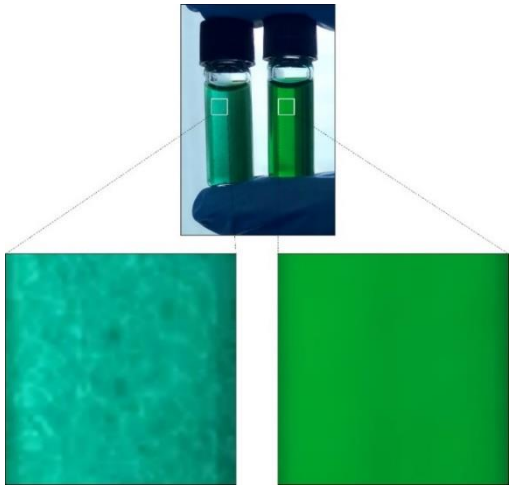

Figure 2.2 Photo of aqueous solutions of ICG in PBS (left) and ICG–CRE in PBS (right). ICG forms visible aggregations in PBS.

Dynamic light scattering (DLS) results showed that the ICG−CRE exhibited a monodispersed hydrodynamic diameter (~10.6 nm) (Figure 2.3).

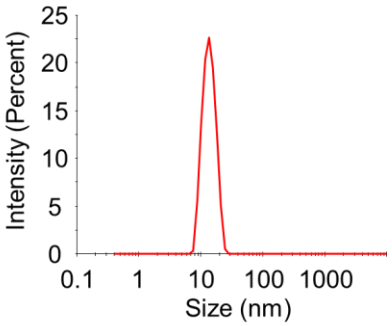

Figure 2.3 DLS size distribution of ICG−CRE

The average hydrodynamic diameter of CRE nanoparticles (~10.4 nm), without ICG, was similar to that of the ICG−CRE. In transmission electron microscopy (TEM), the ICG− CRE nanoparticles were regular in size and shape. (~5−13 nm) (Figure 2.4).

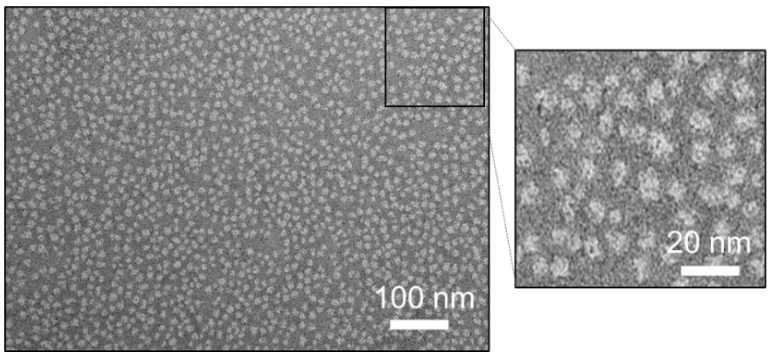

Figure 2.4: TEM images of ICG−CRE. Upper right image represents higher magnification of the boxed area.

Significantly, the prepared ICG−CRE−BB seemed as a cloudy green suspension, in contrast to the natural white color of pristine BB (Figure 2.5). The ICG−CRE−BB dispersion also demonstrated the ability to selectively absorb light in the NIR region, which is a characteristic derived from ICG molecules (Figure 2.6a).

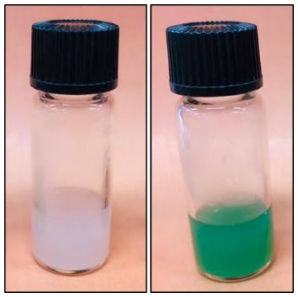

Figure 2.5 Photos of the bacterial suspensions (left, BB; right, ICG−CRE−BB).

The content of the loading and the internalization of ICG was 45.8 μg/mL and 22.9 μg/mL against 2.0×10^9 CFU/mL and 1.0×10^9 CFU/mL of BB, respectively. Upon NIR excitation at 700 nm, ICG−CRE−BB also displayed fluorescence (FL). Notably, the FL of ICG−CRE−BB was observed to be blue-shifted compared with ICG−CRE, possibly due to electron transfer or energy transfer, or both, occurring between the biomolecules and dyes within the cells during the photoinduction process (Figure 2.6b).[41]

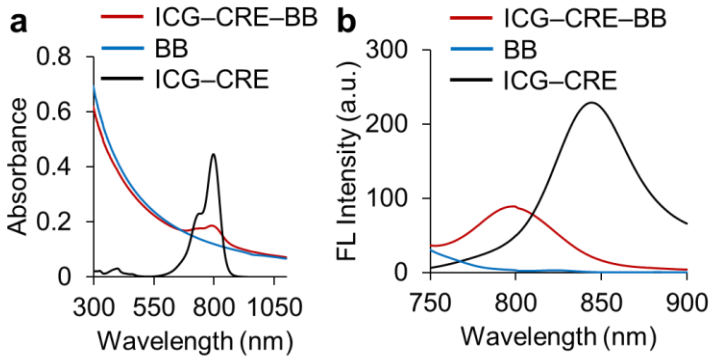

Figure 2.6 (a) UV−vis−NIR absorbance spectra of ICG−CRE−BB (ICG, 45.8 μg/mL; BB, 2.5×10^7 CFU/mL), ICG−CRE (ICG = 45.8 μg/mL), and BB (2.5×10^7 CFU/mL). (b) FL spectra of ICG−CRE−BB (ICG, 45.8 μg/mL; BB, 2.5×10^7 CFU/mL), ICG−CRE (ICG = 12.5 μg/mL), and BB (2.5×10^7 CFU/mL).

In any case, fluorescent optical microscopy showed sufficient NIR FL in ICG−CRE−BB (Figure 2.7), while natural BB did not exhibit any FL (Figures 2.6b and 2.8).

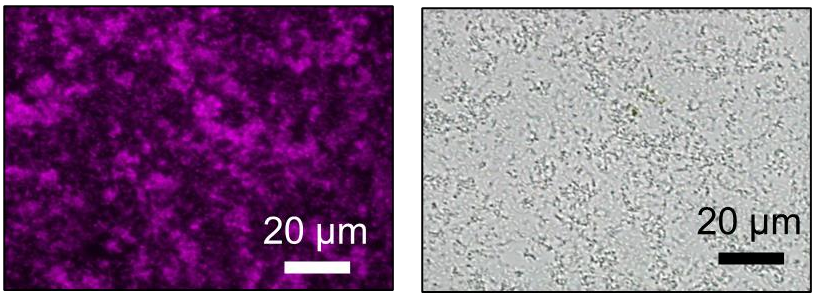

Figure 2.7 In vitro NIR fluorescent (upper) and differential interference contrast (DIC) (bottom) imaging of ICG−CRE−BB. Bacterial concentration is 1.0×10^9 CFU/mL.

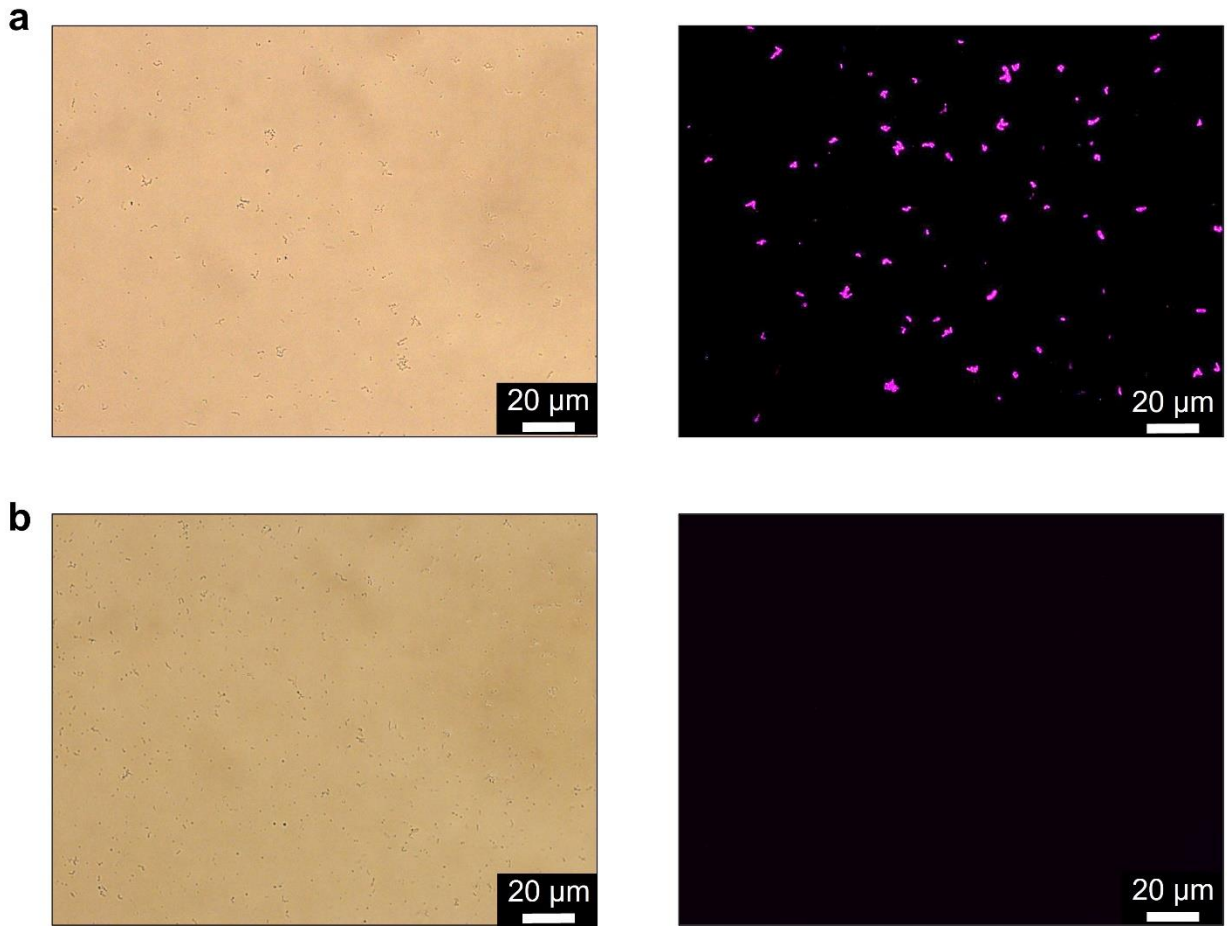

Figure 2.8 In vitro bright-field (left) and NIR fluorescent (right) imaging of (a) ICG–CRE–BB and (b) BB. Bacterial concentration is 1.0×10^6 CFU/ml. These bright-filed images do not represent the perfect bacterial location for each fluorescent image because of Brownian motion of bacteria under microscopy.

Remarkably, effective loading of ICG−CRE in BB was achieved at 37 °C in comparison with the incubation at 4 °C. This difference is presumably because of the temperature response nature of the bacterial membrane (Figure 2.9). In fact, a lower temperature significantly enhances the rigidification of the bacterial membrane which may impede in the incorporation of ICG−CRE with the bacteria.[42]

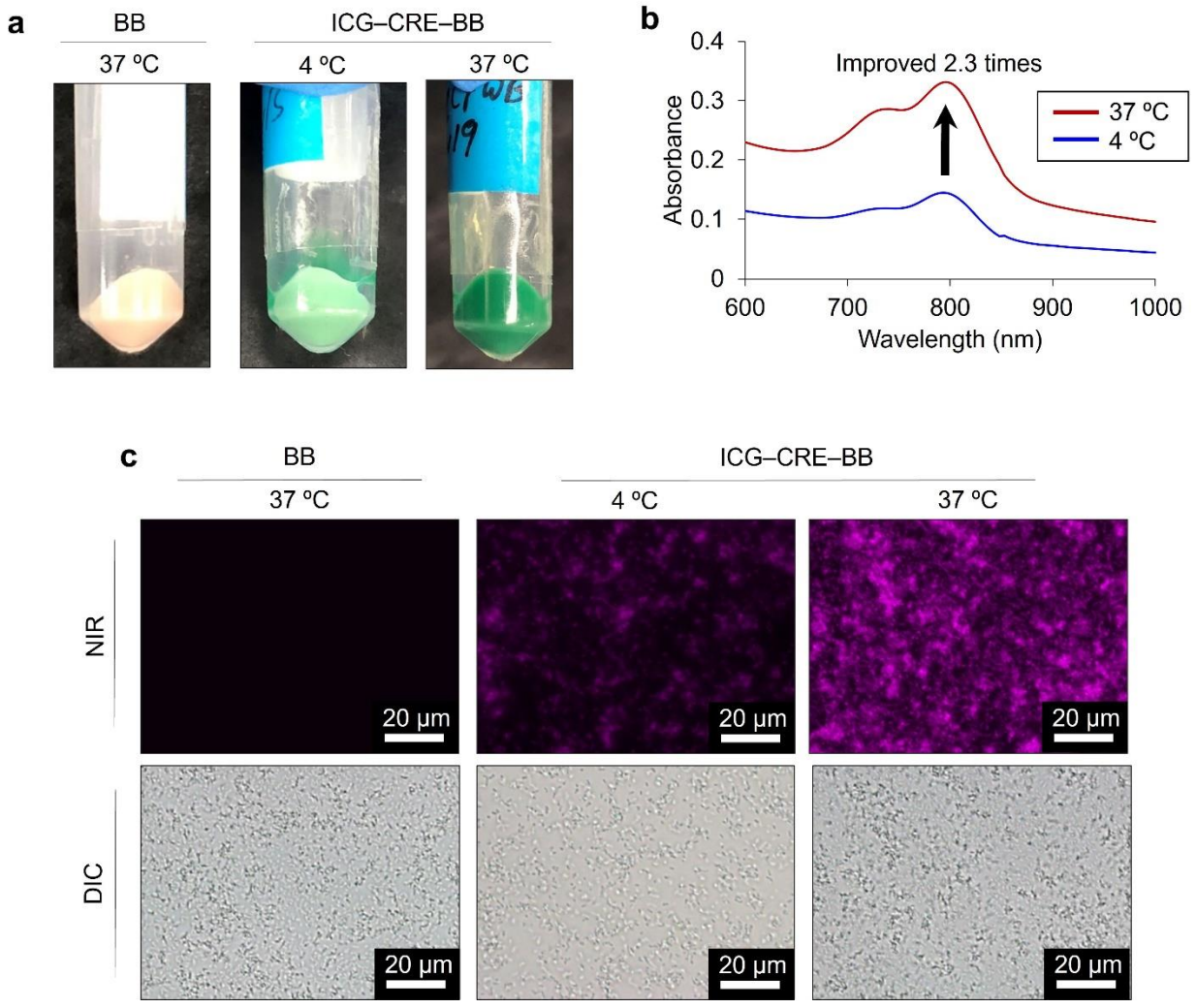

Figure 2.9 Effect of incubation temperature on loading efficiency of ICG–CRE with BB. (a) Images of BB and ICG–CRE–BB pellets. ICG–CRE–BB were prepared at different incubation temperature. (b) UV−vis−NIR absorbance spectra of ICG–CRE–BB prepared at different temperature. (c) Differential interference contrast (DIC) and NIR fluorescent imaging of BB and ICG–CRE–BB prepared at different temperature.

Moreover, in order to clarify the distribution of dye molecules loaded CRE nanoparticles within bacteria, 3D colocations were examined using confocal laser scanning microscopy (Figure 2.10). Before the observation, conventional red and green FL-colored hydrophobic organic dyes such as Nile Red (NR) and 4,4-difluoro-4-bora-3a,4a-diaza-s-indacene (BODIPY) were encapsulated in CRE nanoparticles for the preparation of nanoengineered bacteria. The concentrations of the

loading of NR and BODIPY were 0.34 μg/mL and 1.1 μg/mL, respectively, against 2.0×10^9 CFU/mL of BB. 3D images clearly showed that the entire bacterial body was stained with both the organic dye molecules following the same modification as ICG−CRE with BB. These findings indicate that dye-loaded nanoparticles can be passed through the membrane and achieve even distribution within the bacterial cell.

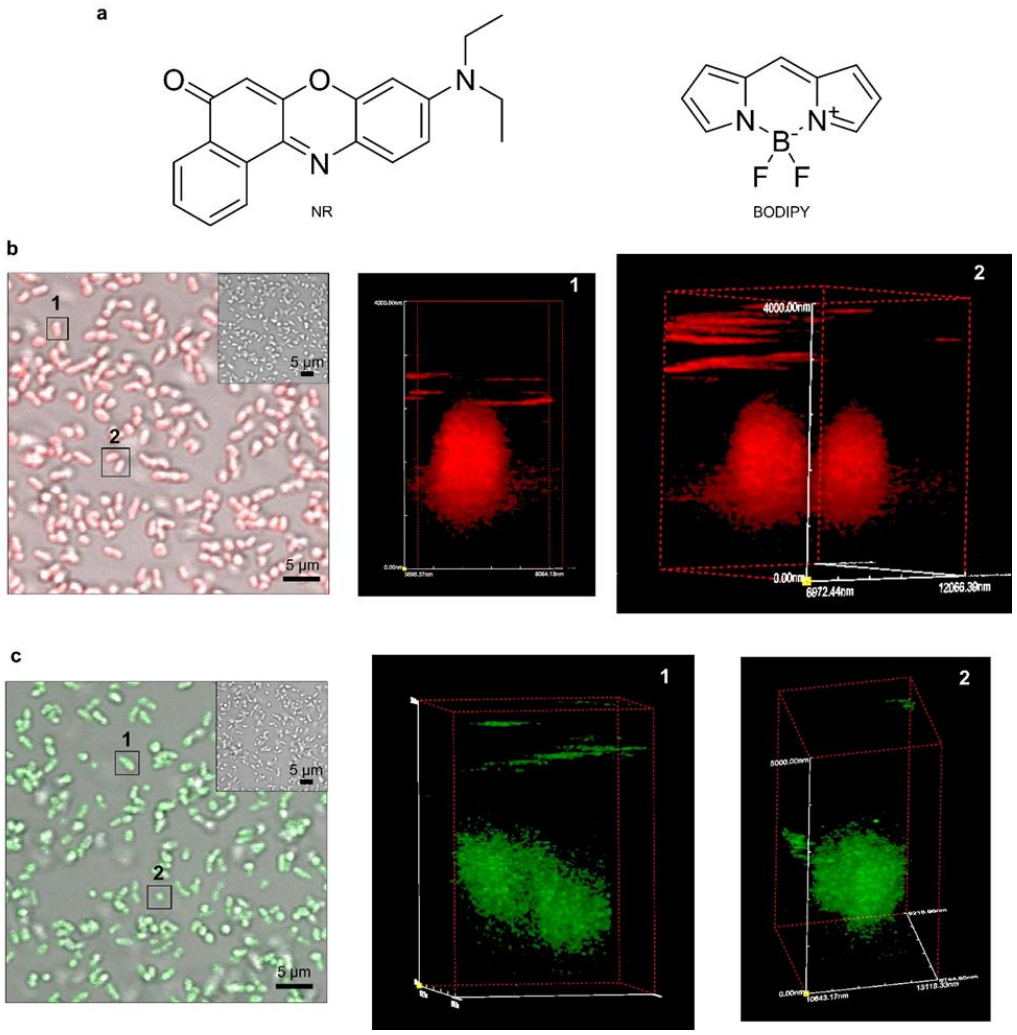

Figure 2.10 Confocal laser scanning microscopy of NR–CRE–BB and BODIPY–CRE–BB. (a) Chemical structures of NR (left) and BODIPY (right). DIC/fluorescent merge and 3D images of (b) NR–CRE–BB and (c) BODIPY–CRE–BB. The numbers (1 or 2) represent the location for analyzing 3D colocation. Upper-right inlet of DIC/fluorescent merge images are the control natural BB without nanoengineering.

Besides, TEM images showed that, during the modification process, the ICG−CRE nanoparticles were localized on the surface of BB and no morphological changes were observed in BB either during or after this process (Figures 2.11 and 2.12).

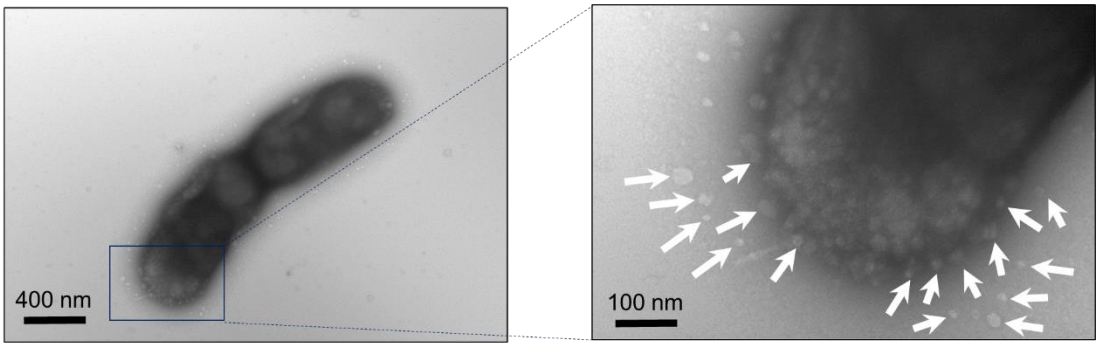

Figure 2.11 TEM images of ICG−CRE−BB.

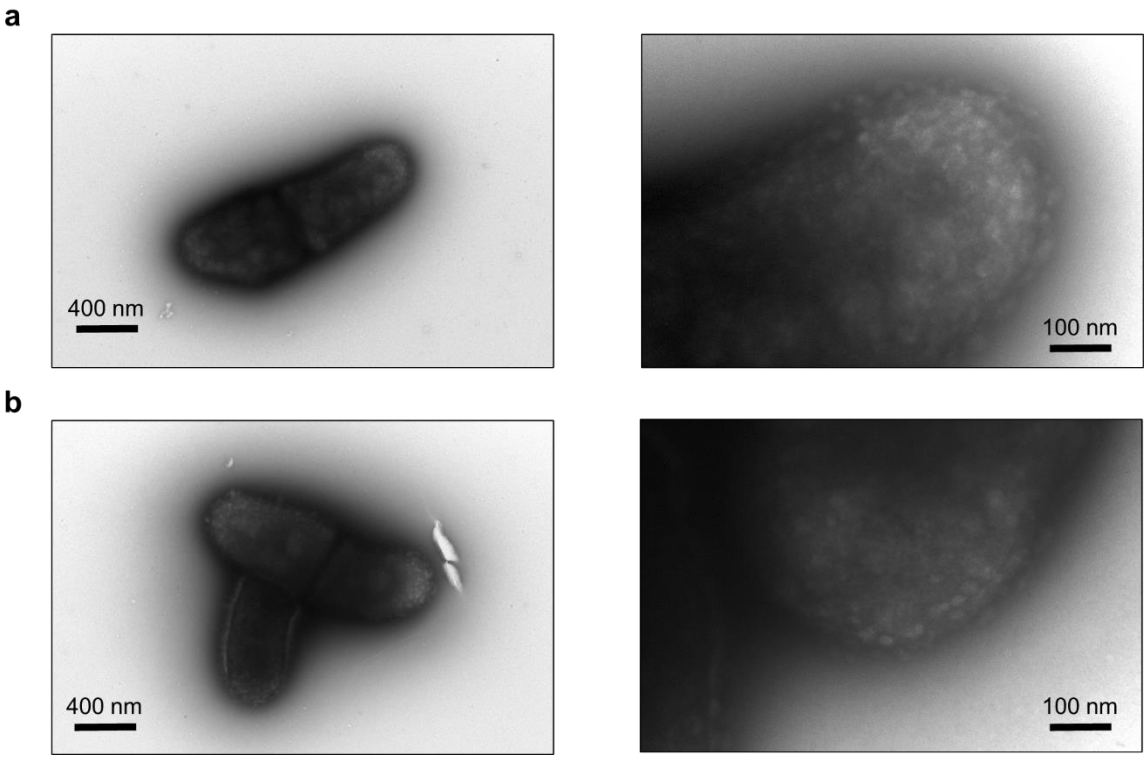

Figure 2.12 TEM images of (a) BB alone and (b) prepared ICG–CRE–BB after washing (left, low magnification; right, high-magnification).

The average viability of the ICG−CRE− BB was approximately 80% after modification. DLS also revealed that the size of the ICG−CRE−BB (~913 nm) was almost identical to that of natural BB (~909 nm) after modification (Figure 2.13). These results clearly showed that ICG−CRE can be safely loaded into BB cells using simple incubation and washing procedures.

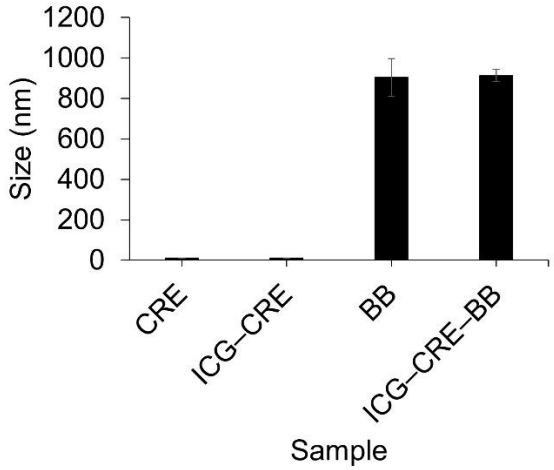

Figure 2.13 DLS size distribution of CRE, ICG–CRE, BB, and ICG–CRE–BB. Polydispersity index of CRE, ICG–CRE, BB, and ICG–CRE–BB is 0.445, 0.451, 0.582, and 0.593, respectively.

ICG exhibits remarkable properties in converting near-infrared (NIR) light energy into heat, by itself, via energy transfer. Compared to other regions of the electromagnetic spectrum, NIR light has the advantage of deeper tissue penetration enabling its interaction with targets located deeper inside the body. ICG exhibits a high absorption peak particularly in the range of 800-900 nm, aligning precisely with the ideal transparency window of biological tissues. Thus, it can be used as a functional dye with photoexothermic and opto-diagnostic properties upon laser irradiation in the NIR range.[41,43] The temperature changes (ΔT) of the ICG−CRE−BB suspensions were evaluated after irradiation at 808 nm NIR, at 1.2 W (~61.1 mW/mm^2). It was observed that the

temperature of the suspension exhibited a significant increase up to ~52.4 °C (maximum ΔT) within after 2 min of laser irradiation owing to the photothermal conversion of ICG (Figure 2.14).

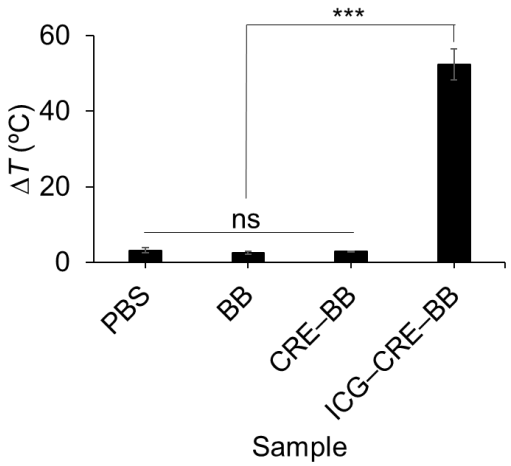

Figure 2.14 Temperature elevation of the various sample solutions after irradiation with 808 nm laser at 1.2 W (~61.1 mW/mm^2) for 2 min. Concentrations of ICG and BB are approximately 22.9 μg/mL and 1.0 × 10^9 CFU/mL, respectively. Data are represented as mean ± standard errors of the mean (SEM); n = 3 independent experiments. ns, not significant; ***, $p < 0.001$.

The average ΔT values of the control experiments, obtained using PBS or PBS dispersions of BB or CRE-functionalized BB without ICG dye (CRE−BB), were very slight, at 3.2, 2.6, and 2.8 °C, respectively. Significantly, the ΔT of the laser-induced ICG−CRE−BB could readily controlled by adjusting the laser power (Figure 2.15).

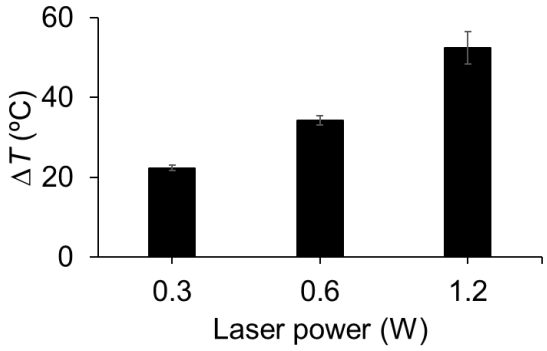

Figure 2.15 Temperature difference (ΔT) of ICG−CRE−BB after laser irradiation for 2 min at different laser powers. The concentrations of ICG and BB are approximately 22.9 μg/mL and 1.0×10^9 CFU/mL, respectively.

Notably, ΔT of ICG−CRE−BB also represented higher than that of ICG−CRE after laser irradiation for 2 min at each laser power possibly due to the aforementioned energy or electron transfer mechanism (Figure 2.16).[41] The photothermal conversion efficiency of ICG−CRE−BB was ~38%, surpassing that of conventional photoexothermic nanoparticles like metal nanoparticles, carbon dots, and semiconducting polymer nanoparticles (Table 2.2).[44–46] Thus, we believe that the NIR light-induced ICG−CRE−BB has the potential to serve as a promising NIR theranostic agent for the treatment of deep-tissue cancer.

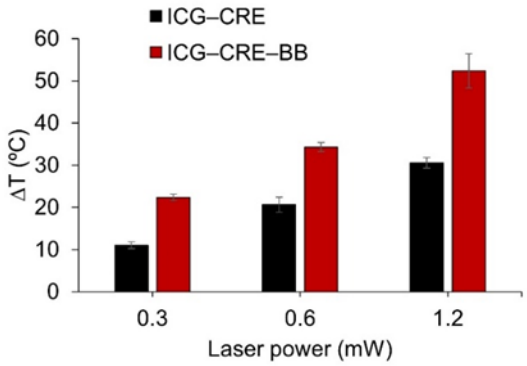

Figure 2.16 Temperature difference (ΔT) of ICG–CRE–BB and ICG–CRE after laser irradiation for 2 min at different laser powers. The concentrations of ICG and BB are approximately 22.9 μg/mL and 1.0×10^9 CFU/mL, respectively. Data are represented as mean ± SEM; n = 3 independent experiments.

Table 2:2 The photothermal conversion efficiency of materials in previous reports

Material	Photothermal conversion efficiency (%)	Reference
ICG–CRE–BB	38	This study
Gold nanorods	21	38
Gold nanoshells	13	38
Copper selenide	22	38
Carbon dots	31	39
Semiconducting polymer nanoparticles	37	40

To investigate whether ICG−CRE−BB can be used for cancer therapy, the cytotoxicity of ICG−CRE−BB was assessed using mouse rectal carcinoma (Colon26) and human normal diploid fibroblast (MRC5) cell lines (Figures 2.17a and 2.17b).

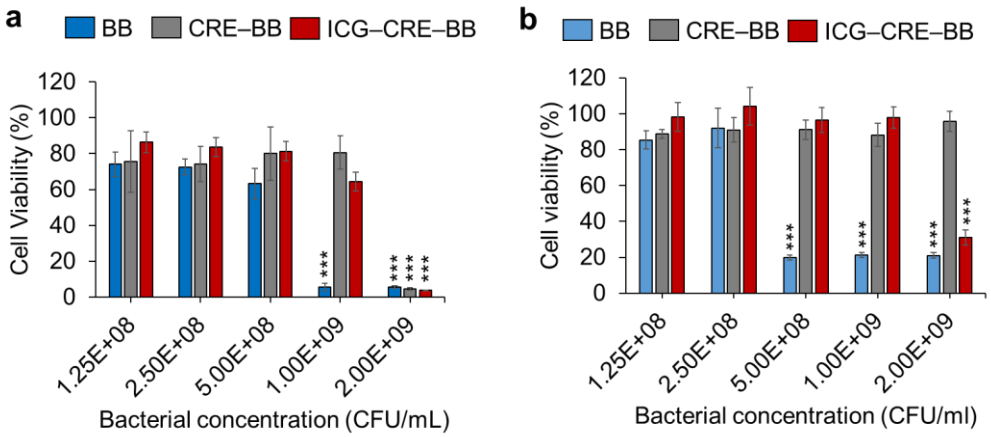

Figure 2.17 Cytotoxicity of bacteria. (a) The viability of Colon26 cancer cell line was tested 24 h after treatment with ICG−CRE−BB, CRE−BB, and BB at different bacterial concentrations. (b) The viability of MRC5 cell line was tested 4 h after treatment with ICG–CRE–BB, CRE–BB, and BB at different bacterial concentrations. Data are represented as mean ± SEM; n = 5 independent experiments. ***, $p < 0.001$ vs control w/o bacteria (Student's t-test).

Regardless of the method of nanomodification employed, none of the bacterial suspensions exhibited significant cytotoxicity at low bacterial concentrations (<2.5×10^8 CFU/mL) across any of the tested cell lines. More importantly, ICG−CRE−BB and CRE−BB displayed lower cytotoxicity than BB at a bacterial concentration of 1×10^9 CFU/mL, probably due to the enhanced biocompatibility caused by polyethylene glycol moieties in the CRE structure.[47] Subsequently, we evaluated the complete blood counts (CBCs) and blood biochemical parameters of mice 30 days after administering them with PBS or PBS dispersions containing ICG−CRE−BB, CRE−BB, or BB (Tables 2.3−2.5). No significant differences observed between the parameters of the bacteria-injected and control PBS-injected mouse groups. Herein, we concluded that none of the bacterial

dispersions exhibited toxicity at low concentrations *in vivo*. Next, laser-induced cytotoxicity of the biocompatible bacteria on Colon26 and MRC5 cell lines was investigated using NIR laser irradiation (Figures 2.18a and 2.18b). Cell seeded plates containing the samples were exposed to laser irradiation in a 37°C incubator. The ICG−CRE−BB and ICG−CRE dispersions demonstrated effectively elimination of the cells after irradiation at 1.2 W (~61.1 mW/mm^2) for 1 or 3 min, due to the powerful photothermal conversion property of ICG−CRE−BB and ICG−CRE as cancer cells are normally sensitive to heat.[48] In contrast, the control groups (PBS, BB, and CRE−BB) exhibited no cytotoxicity at any of the laser irradiation time.

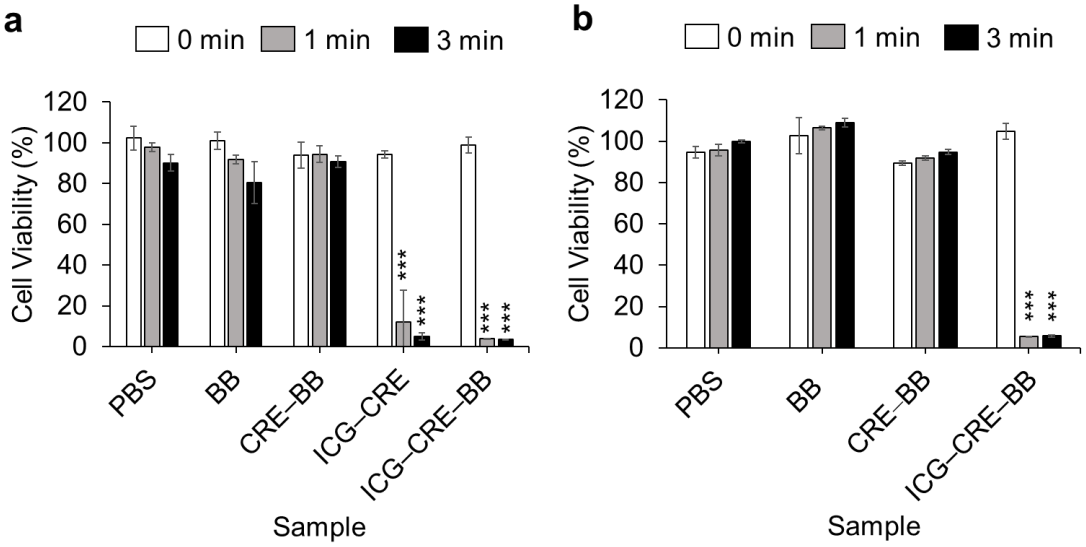

Figure 2.18 (a) Cell viability of Colon26 cancer cell line treated with laser-irradiated PBS (control), BB, CRE−BB, ICG−CRE, and ICG−CRE−BB at different irradiation times. The concentrations of ICG and BB are approximately 22.9 μg/mL and 1.0 × 10^9 CFU/mL, respectively. The cell viability was tested 24 h after irradiation [laser power =1.2 W (~61.1 mW/mm^2)]. (b) Cell viability of MRC5 cell line treated with laser-irradiated PBS (control), ICG–CRE–BB, CRE–BB, and BB at different irradiation times. The concentration of bacteria is 1 × 10^9 CFU/mL. The cell viability was tested 24 h after irradiation [laser power = 1.2 W (~ 61.1 mW/mm^2)]. Data are represented as the mean ± SEM; n = 3 independent experiments. ***, $p < 0.001$ vs control w/o laser irradiation (Student's t-test).

Table 2:3 CBCs and biochemical parameters of the mice injected with PBS or BB dispersion after 30 days

Measured value	Entry	Unit	PBS (n = 5)	BB (n = 5)	P value
CBC	WBC	$\times 10^2$ /μL	58.2 ± 4.35	58.4 ± 5.57	> 0.05
	RBC	$\times 10^4$ /μL	893 ± 17.81	915.2 ± 30.02	> 0.05
	HGB	g/dL	13.74 ± 0.26	14.42 ± 0.42	> 0.05
	HCT	%	41.64 ± 0.95	42.8 ± 1.39	> 0.05
	MCV	fL	46.6 ± 0.16	46.78 ± 0.16	> 0.05
	MCH	pg	14.72 ± 0.12	15.76 ± 0.10	> 0.05
	MCHC	g/dL	33.36 ± 0.15	33.72 ± 0.15	> 0.05
	PLT	$\times 10^4$ /μL	71.28 ± 2.39	70.52 ± 0.97	> 0.05
Biochemical parameters	TP	g/dL	4.02 ± 0.09	4.02 ± 0.04	> 0.05
	ALB	g/dL	2.7 ± 0.04	2.74 ± 0.04	> 0.05
	BUN	mg/dL	19.2 ± 0.89	19.4 ± 0.66	> 0.05
	CRE	mg/dL	0.124 ± 0.01	0.132 ± 0.01	> 0.05
	Na	mEq/L	153.8 ± 1.56	153.2 ± 0.97	> 0.05
	K	mEq/L	4.22 ± 0.26	4.08 ± 0.30	> 0.05
	Cl	mEq/L	118 ± 0.32	118.6 ± 0.87	> 0.05
	AST	IU/L	66.6 ± 3.03	66.2 ± 4.25	> 0.05
	ALT	IU/L	43.2 ± 0.73	42.2 ± 2.71	> 0.05
	LDH	IU/L	302.4 ± 22.23	363.8 ± 27.52	> 0.05
	AMY	IU/L	1712.8 ± 28.52	1708.8 ± 85.29	> 0.05
	CK	IU/L	174.6 ± 28.67	171.6 ± 12.01	> 0.05

Data are represented as the mean ± SEM; n = 5 biologically independent mice. Statistical analyses were performed using the two-way ANOVA test.

Abbreviations: ALB, albumin; ALT, alanine transaminase; AMY, amylase; AST, aspartate aminotransferase; BUN, blood urea nitrogen; Cl, chlorine; CK, creatine kinase; CRE, creatinine; CRP, C-reactive protein; HCT, hematocrit; HGB, hemoglobin; K, potassium; LDH, lactate dehydrogenase; MCH, mean corpuscular hemoglobin; MCHC, mean corpuscular hemoglobin concentration; MCV, mean corpuscular volume; Na, sodium; PLT, platelet; RBC, red blood cell; TP, total protein; WBC, white blood cell.

Table 2:4 CBCs and biochemical parameters of the mice injected with PBS or CRE–BB dispersion after 30 days.

Measured value	Entry	Unit	PBS (n = 5)	CRE–BB (n = 5)	P value
CBC	WBC	$\times 10^2$ /μL	58.2 ± 4.35	58.2 ± 2.40	> 0.05
	RBC	$\times 10^4$ /μL	893 ± 17.81	892.6 ± 28.97	> 0.05
	HGB	g/dL	13.74 ± 0.26	14.02 ± 0.44	> 0.05
	HCT	%	41.64 ± 0.95	41.46 ± 1.42	> 0.05
	MCV	fL	46.6 ± 0.16	46.44 ± 0.22	> 0.05
	MCH	pg	14.72 ± 0.12	15.7 ± 0.08	> 0.05
	MCHC	g/dL	33.36 ± 0.15	33.84 ± 0.28	> 0.05
	PLT	$\times 10^4$ /μL	71.28 ± 2.39	72.28 ± 2.17	> 0.05
Biochemical parameters	TP	g/dL	4.02 ± 0.09	4.06 ± 0.05	> 0.05
	ALB	g/dL	2.7 ± 0.04	2.74 ± 0.02	> 0.05
	BUN	mg/dL	19.2 ± 0.89	19.26 ± 0.36	> 0.05
	CRE	mg/dL	0.124 ± 0.01	0.12 ± 0.01	> 0.05
	Na	mEq/L	153.8 ± 1.56	151.8 ± 0.58	> 0.05
	K	mEq/L	4.22 ± 0.26	4 ± 0.18	> 0.05
	Cl	mEq/L	118 ± 0.32	118.2 ± 0.58	> 0.05
	AST	IU/L	66.6 ± 3.03	65.2 ± 6.04	> 0.05
	ALT	IU/L	43.2 ± 0.73	43 ± 2.86	> 0.05
	LDH	IU/L	302.4 ± 22.23	303.2 ± 32	> 0.05
	AMY	IU/L	1712.8 ± 28.52	1702 ± 56.48	> 0.05
	CK	IU/L	174.6 ± 28.67	129.3 ± 22.45	> 0.05

Data are represented as the mean ± SEM; n = 5 biologically independent mice. Statistical analyses were performed using the two-way ANOVA test.

Abbreviations: ALB, albumin; ALT, alanine transaminase; AMY, amylase; AST, aspartate aminotransferase; BUN, blood urea nitrogen; Cl, chlorine; CK, creatine kinase; CRE, creatinine; CRP, C-reactive protein; HCT, hematocrit; HGB, hemoglobin; K, potassium; LDH, lactate dehydrogenase; MCH, mean corpuscular hemoglobin; MCHC, mean corpuscular hemoglobin concentration; MCV, mean corpuscular volume; Na, sodium; PLT, platelet; RBC, red blood cell; TP, total protein; WBC, white blood cell.

Table 2:5 CBCs and biochemical parameters of the mice injected with PBS or ICG–CRE–BB dispersion after 30 days.

Measured value	Entry	Unit	PBS (n = 5)	ICG–CRE–BB (n = 5)	P value
CBC	WBC	$\times 10^2$ /μL	58.2 ± 4.35	58 ± 2.77	> 0.05
	RBC	$\times 10^4$ /μL	893 ± 17.81	883.8 ± 10.16	> 0.05
	HGB	g/dL	13.74 ± 0.26	13.88 ± 0.17	> 0.05
	HCT	%	41.64 ± 0.95	40.98 ± 0.49	> 0.05
	MCV	fL	46.6 ± 0.16	46.38 ± 0.16	> 0.05
	MCH	pg	14.72 ± 0.12	15.7 ± 0.05	> 0.05
	MCHC	g/dL	33.36 ± 0.15	33.84 ± 0.10	> 0.05
	PLT	$\times 10^4$ /μL	71.28 ± 2.39	70.76 ± 0.88	> 0.05
Biochemical parameters	TP	g/dL	4.02 ± 0.09	4.18 ± 0.12	> 0.05
	ALB	g/dL	2.7 ± 0.04	2.84 ± 0.05	> 0.05
	BUN	mg/dL	19.2 ± 0.89	19.44 ± 0.89	> 0.05
	CRE	mg/dL	0.124 ± 0.01	0.114 ± 0.01	> 0.05
	Na	mEq/L	153.8 ± 1.56	153 ± 0.71	> 0.05
	K	mEq/L	4.22 ± 0.26	4.12 ± 0.13	> 0.05
	Cl	mEq/L	118 ± 0.32	119.2 ± 0.80	> 0.05
	AST	IU/L	66.6 ± 3.03	65.6 ± 2.36	> 0.05
	ALT	IU/L	43.2 ± 0.73	42.4 ± 0.81	> 0.05
	LDH	IU/L	302.4 ± 22.23	351 ± 39.32	> 0.05
	AMY	IU/L	1712.8 ± 28.52	1725.8 ± 4.85	> 0.05
	CK	IU/L	174.6 ± 28.67	100.3 ± 14.09	> 0.05

Data are represented as the mean ± SEM; n = 5 biologically independent mice. Statistical analyses were performed using the two-way ANOVA test.

Abbreviations: ALB, albumin; ALT, alanine transaminase; AMY, amylase; AST, aspartate aminotransferase; BUN, blood urea nitrogen; Cl, chlorine; CK, creatine kinase; CRE, creatinine; CRP, C-reactive protein; HCT, hematocrit; HGB, hemoglobin; K, potassium; LDH, lactate dehydrogenase; MCH, mean corpuscular hemoglobin; MCHC, mean corpuscular hemoglobin concentration; MCV, mean corpuscular volume; Na, sodium; PLT, platelet; RBC, red blood cell; TP, total protein; WBC, white blood cell.

Furthermore, internalization and distribution of ICG−CRE−BB in Colon26 cells were investigated using optical microscopy (Figure 2.19), which revealed intracellular ICG−CRE−BB uptake in cells after incubation with ICG−CRE−BB at 37°C for 4 h. Indeed, NIR FL of ICG−CRE−BB (pink colored dots) was uniformly distributed in cytosols of the cells. Nuclei of the cells were not stained with ICG−CRE−BB. The control cells without ICG−CRE−BB treatment did not exhibit any FL at all. Subsequently, after incubation of cells with ICG−CRE−BB at 4 °C for 4 h, the images showed that NIR FL derived from ICG−CRE−BB was relatively weak, indicating that the cell internalization was energy dependent.[49] Therefore, endocytosis is a possible cellular uptake pathway for these ICG−CRE−BB. These results indicate the high biocompatibility, unique intracellular permeability, excellent NIR fluorescence, and strong photothermal properties of ICG−CRE−BB, thus indicating its potential as a "nanoengineered fighter" in cancer optotheranostics.

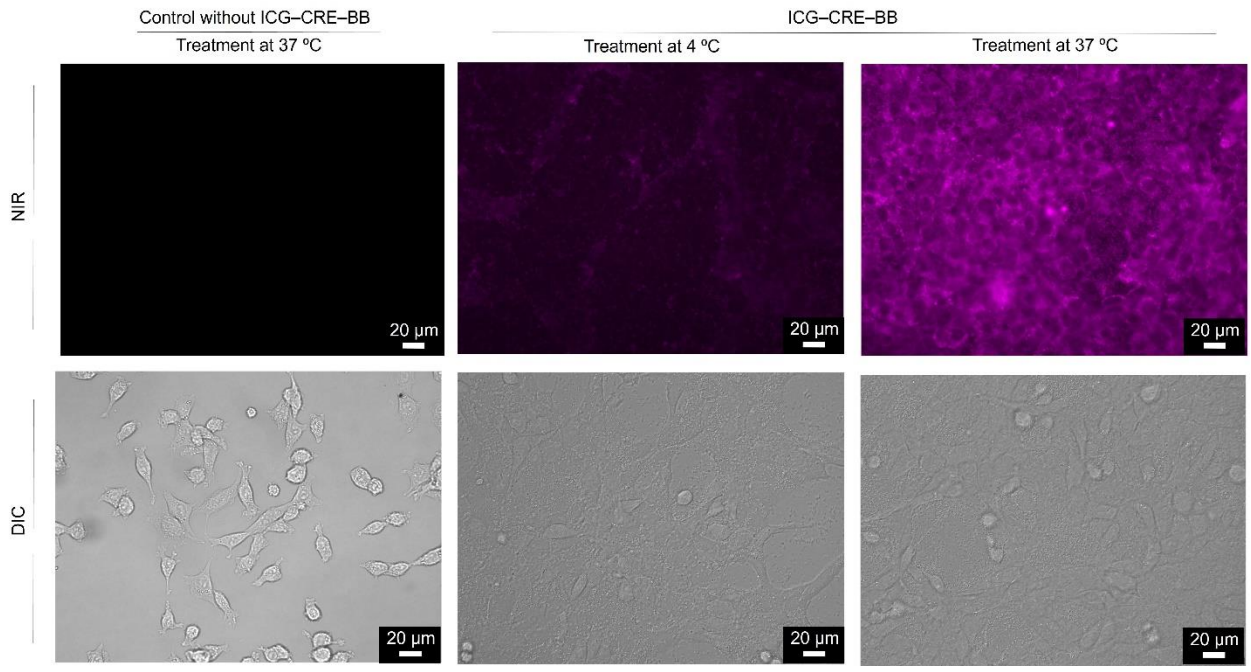

Figure 2.19 Optical micrographs of Colon26 cells (2.5×10^5 cells/mL) after 4-h incubation with and without ICG–CRE–BB (1.0×10^7 CFU) at 4 °C or 37 °C in a fridge or 5% CO_2.

2.3.2 In vivo anticancer efficacies of bacterial treatments

We explored the potential capacity of NIR FL of ICG−CRE−BB in mice for cancer optical diagnostics (Figure 2.20). ICG−CRE−BB was administered via intratumoral injection, and their systemic distribution was monitored at the indicated time intervals using an NIR fluorescence imaging system. As shown in Figure 2.20a, FL of ICG−CRE−BB was observed in the tumor and remained visible for a long period (at least 96 h). Nevertheless, no FL was detected in the vital organs, such as lungs, liver, kidneys, heart, and spleen, at 96 h post injection, which was mainly attributed to the tumor hypoxia specificity of BB (Figure 2.20b).[32] On the contrary, both tumors and vital organs of PBS-injected mice exhibited no FL. The remarkable tumor selectivity of ICG−CRE−BB was further confirmed by colony assay following intravenous injection (Figure

2.21). Following that, we examined the in vivo therapeutic anticancer efficacy of the bacteria using a tumor syngeneic model (Figures 2.22).

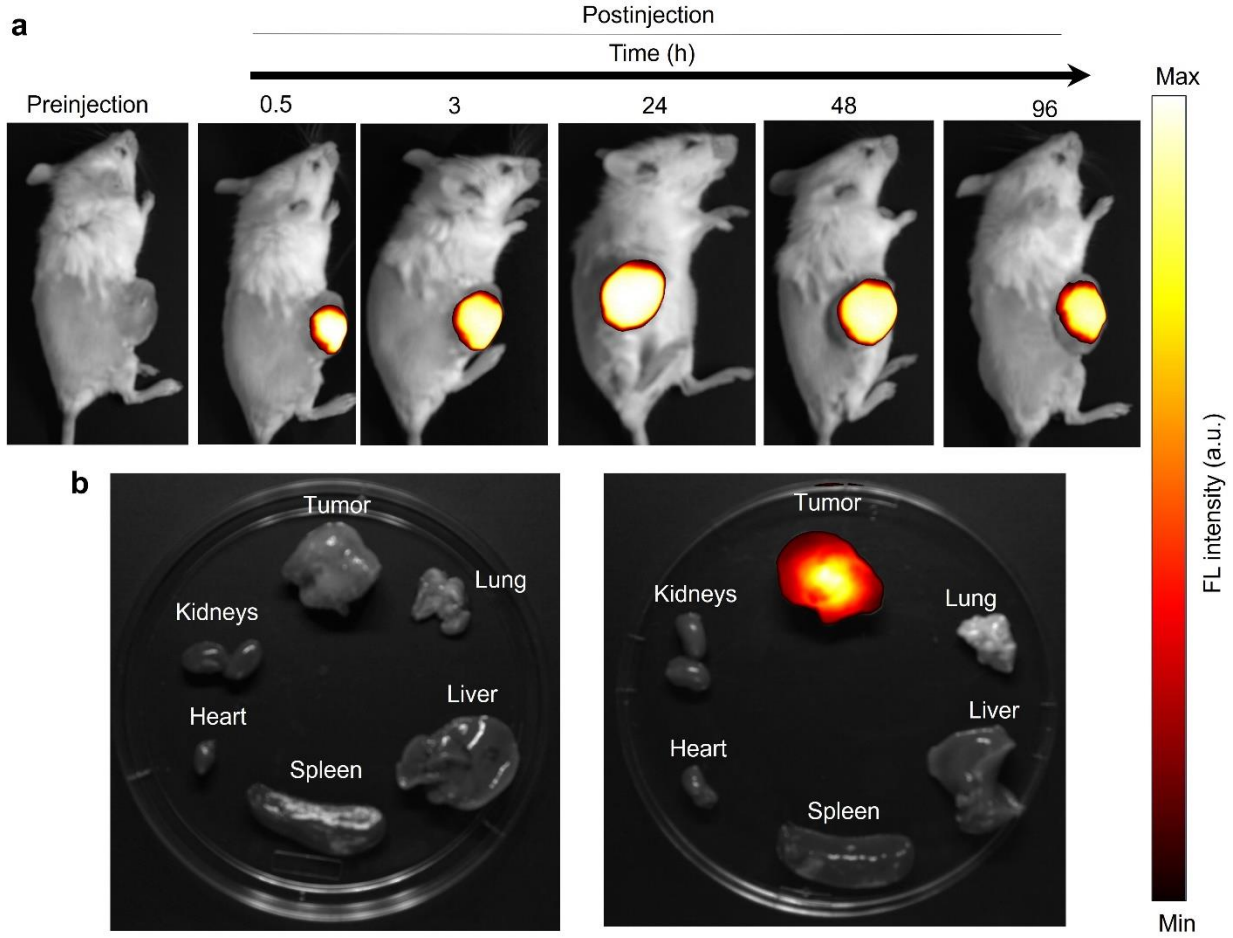

Figure 2.20 Biological distribution of ICG–CRE–BB. (a) FL imaging of Colon26 tumor-bearing mice after intratumoral injection of ICG–CRE–BB (100 μL, 5×10^8 CFU). (b) NIR FL imaging of tumor and major organs 96 h post-intratumoral injection of PBS (left) and ICG–CRE–BB (right).

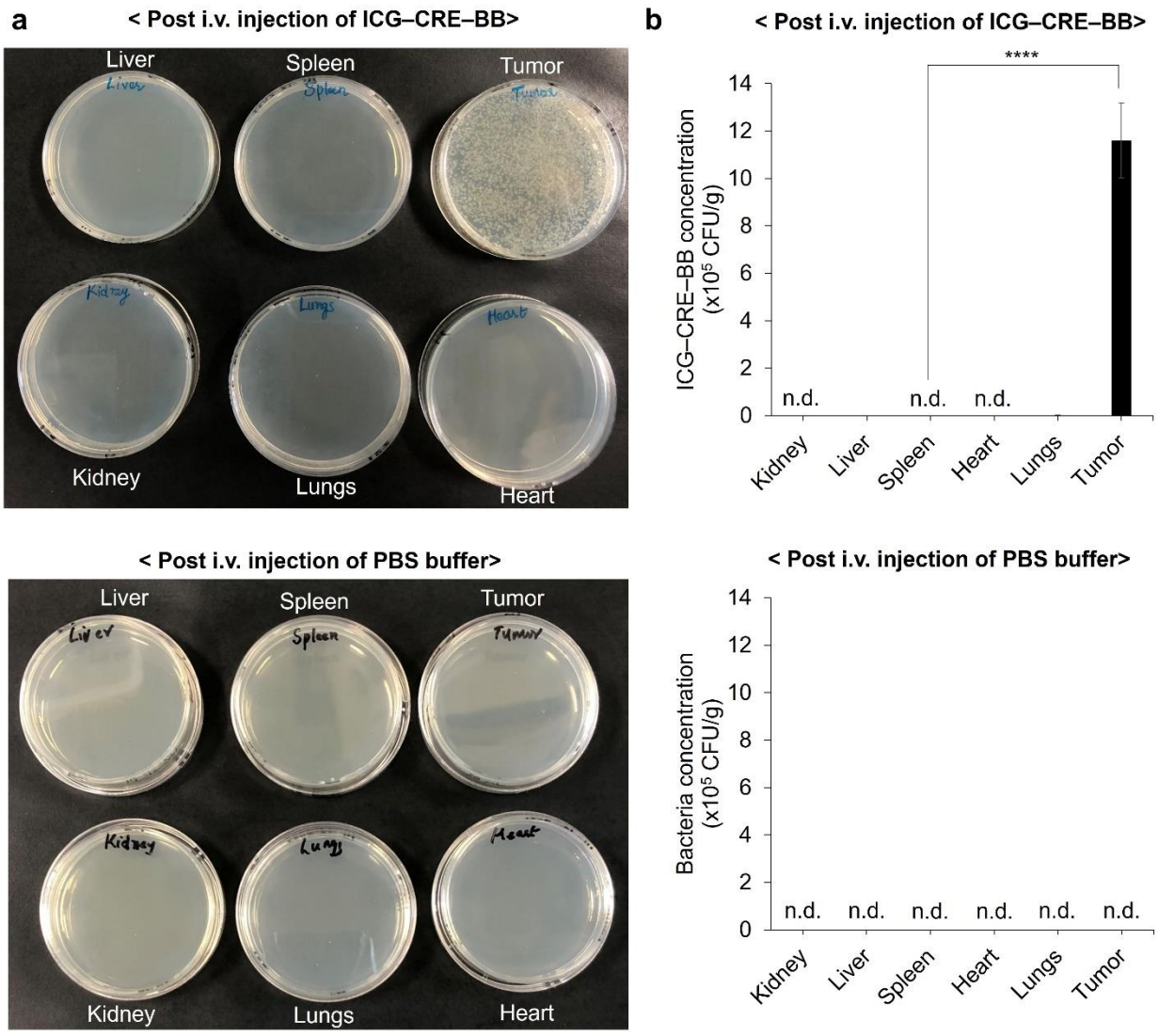

Figure 2.21 Tumor targeting effect of ICG–CRE–BB. (a) Bacteria colony of organs/tumors of Colon26 tumor-bearing mice over time after intravenous (i.v.) injection of ICG–CRE–BB (100 μL, 1×10^6 CFU) or PBS (100 μL) for 120 h. (b) Colony number of Colon26 tumor-bearing mice after i.v. injection of ICG–CRE–BB (100 μL, 1×10^6 CFU) or PBS (100 μL) for 120 h. Data are represented as means ± standard errors of the mean (SEM); n = 3 independent experiments. n.d., not detectable; ****, $p < 0.0001$.

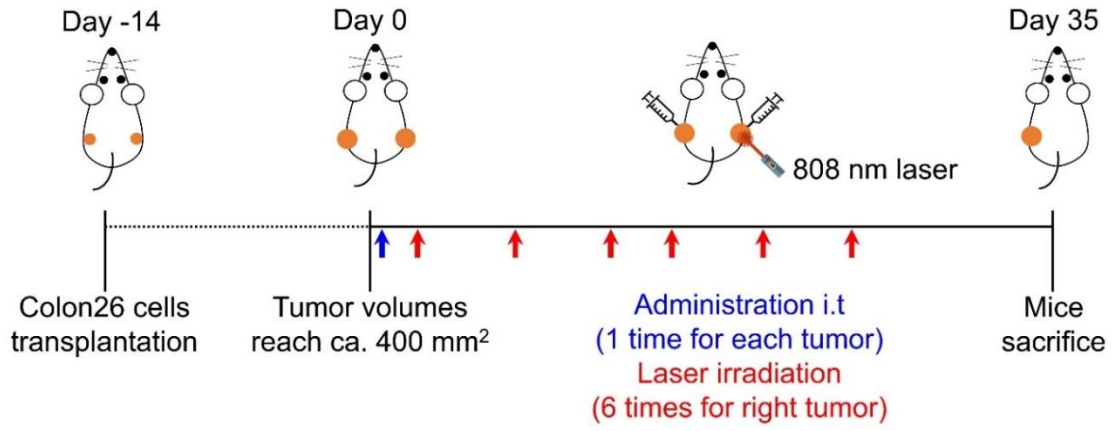

Figure 2.22 Schematic illustration of in vivo antitumor tests using NIR laser-induced ICG–CRE–BB.

Colon26-bearing immunocompetent mice were intratumorally injected with PBS (100 μL) or PBS dispersions containing ICG−CRE−BB, CRE−BB, or BB (100 μL, 5×10^8 CFU of bacteria). Following an overnight bacterial accumulation, the solid tumors were subjected to irradiation using an 808 nm NIR laser at 0.7 W (~36.3 mW/mm^2), for 3 min. Throughout the laser irradiation surface temperature of the mice was monitored using a thermographic camera. (Figure 2.23 a,b).

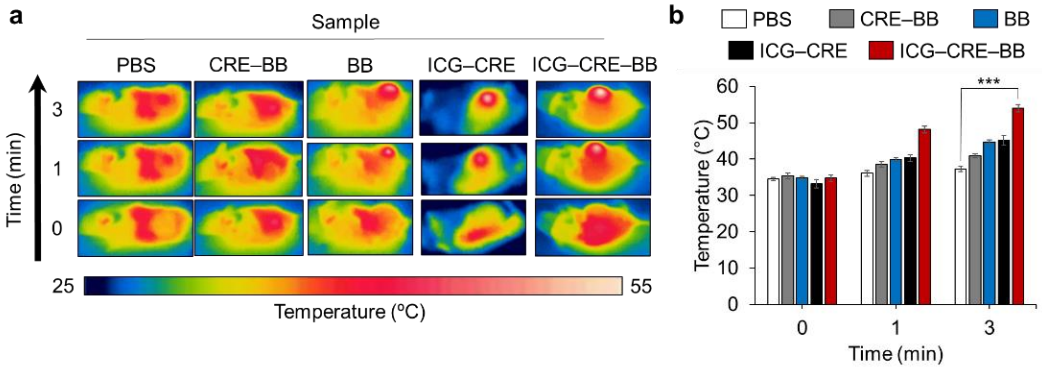

Figure 2.23 In vivo optical tumor destruction. (a) IR thermal images of laser-induced mice at various time points (0, 1, and 3 min). (b) Surface temperature of the solid tumor in Colon26-bearing mice on the 2nd day after injection with ICG−CRE−BB, ICG−CRE, CRE−BB, BB, or PBS, followed by 808 nm laser irradiation for 3 min [laser power = 0.7 W (~36.3 mW/mm^2)]. Concentrations of ICG and BB are approximately 45.8 μg/mL and 2.0×10^9 CFU/mL, respectively. Data are represented as mean ± SEM; n = 3 independent experiments. ***, $p < 0.001$.

The surface temperature of the solid tumors was roughly around 35°C pre- and post-injection of PBS or bacteria. No significant increase in temperature was observed in the mice injected with PBS (maximum temperature was approximately 37 °C) after laser irradiation. On the contrary, the mice injected with ICG−CRE−BB and BB showed a noticeable temperature increase, reaching ∼54 and 44°C, respectively, 3 min post laser irradiation. ICG−CRE nanoparticle resulted in an average surface temperature of the tumor at 45 °C after laser irradiation for 3 min. Furthermore, CRE−BB induced only a minor temperature elevation (∼41 °C) compared to the other bacterial groups. Indeed, the tumors of mice injected with the various types of bacterial dispersions exhibited a darker appearence (blackish color), probably because of thrombosis resulting from bacterial infection. The presence of bacteria possibly triggers an immunological response, which activates blood coagulation factors, leading to the formation of clots. (Figure 2.24).[13,50] The disruption of tumor blood vessels can result in the concentrated blood coagulation within the tumor, a process known to be associated with thrombosis.[13,50] This phenomenon was observed in the tumor of mice injected with bacteria leading to bacterial infection within the tumor. The photothermal conversion performance and optical absorbance could ultimately be improved due to the higher condensation of hemoglobin molecules in blood clots, which occurs when the blood cells are coagulated. Here, we believe that thrombosis also plays a role in the temperature elevation of a tumor during laser irradiation. No change in the tumor color was observed in the PBS-injected control mice. The observed change in tumor color is beneficial for effective NIR light harvesting and its conversion into thermal energy for the effective tumor elimination.[50] Though the NIR laser-triggered temperature elevations were triggered by bacterial infection or ICG−CRE nanoparticles injection, ICG−CRE−BB showed the highest tumor surface temperature (∼54 °C) after the 3 min laser irradiation because of the excellent photoexothermicity of ICG, light absorbable bacterial

infection-triggered thrombosis and effective electron or energy transformation of intracellular ICG (enhancement of photothermal conversion effect).

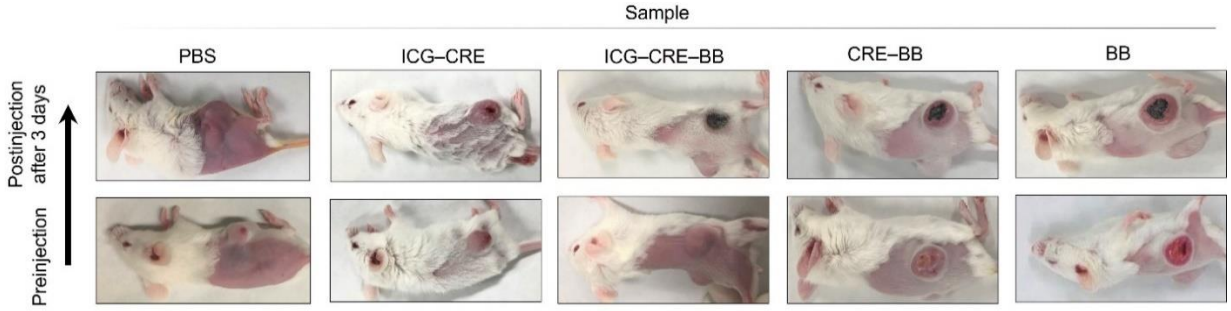

Figure 2.24 Photos of mice pre-injection and 3 days post-injection of PBS, ICG–CRE, ICG–CRE–BB, CRE–BB, and BB.

Due to the significant photothermal conversion of ICG− CRE−BB, laser-induced ICG−CRE−BB exhibited evident antitumor therapeutic effect against tumors; the solid tumors injected with ICG−CRE−BB disappeared after laser irradiation (Figure 2.25a).

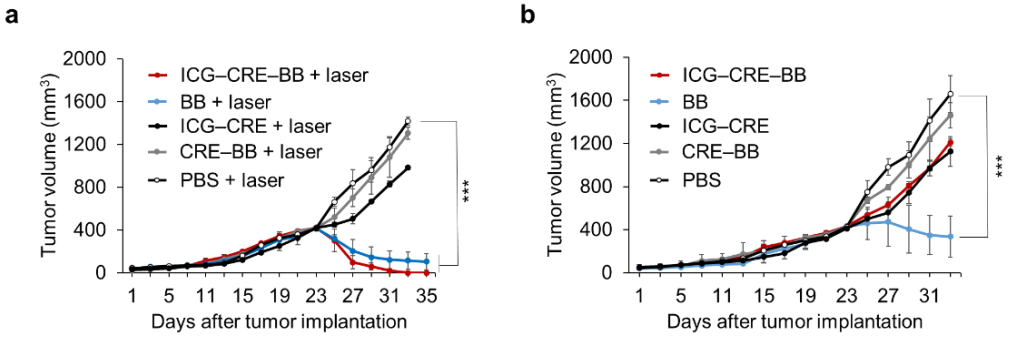

Figure 2.25 (a) Relative volumes of the tumors on the laser-irradiated right flank of mice. PBS or PBS dispersions of CRE−BB, BB, ICG−CRE, or ICG−CRE−BB were intratumorally injected, and the injected tumors were treated with 808 nm laser irradiation [laser power = 713 mW (~36.3 mW/mm^2); irradiation time = 3 min] 24 h after the injections. Concentrations of ICG and BB are approximately 45.8 μg/mL and 2.0×10^9 CFU/mL, respectively. Data are presented as mean ± SEM (n = 3 biologically independent tests), ***$p < 0.001$ (Student's t test of PBS). (b) Relative volumes of the tumors on the left flank of mice after intratumoral injection of PBS or PBS dispersions of CRE−BB, BB, ICG−CRE, or ICG−CRE−BB, without laser irradiation. Concentrations of ICG and BB are approximately 22.9 μg/mL and 1.0×10^9 CFU/mL, respectively. Data are presented as mean ± SEM (n = 3 biologically independent tests), ***$p < 0.001$ (Student's t test for PBS).

Significantly, the complete disappearance of tumor, leading to a prolonged life span, was observed in the mice treated with laser-induced ICG−CRE−BB during the 45-d follow-up period after the experiment (Figure 2.26).

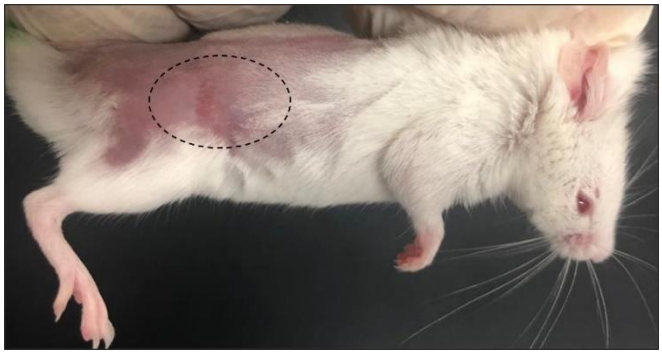

Figure 2.26 Photo of the mouse treated with laser-induced ICG–CRE–BB (Day 45). Dashed circle represents treated area.

Remarkably, even the mice treated with BB displayed drastic reduction in tumor volume owing to the above-mentioned bacterial infection without attenuatable CRE coating (Figure 2.25b). Though the laser-induced BB group showed effective antitumor suppression, its efficacy was comparatively lower than that of the laser-driven ICG−CRE−BB group. We believe that the proposed bionanotechnology offers a significant advantage compared to using bacteria alone for photothermal cancer therapy because the combination of excellent NIR FL of ICG−CRE−BB and potent antitumor efficacy of laser-induced ICG−CRE−BB would be synergistically available as an optical theranostic agent. On the other hand, volume of tumors increased over time in the PBS, PBS + laser, CRE−BB, CRE−BB + laser, and ICG−CRE−BB groups. Additionally, the body weight of the mice remained relatively constant throughout the experimental period in all treatment groups, revealing no side effects, with the exception of the ICG−CRE−BB group (Figure 2.27). Besides, due to the significant elimination of solid tumors (~400 mm^3) on the right flank of the

mice by laser-induced ICG−CRE−BB, a slight reduction in the body weight was observed in the treated mice from day 21. Nevertheless, these mice displayed a recovery in their weight from day 29.

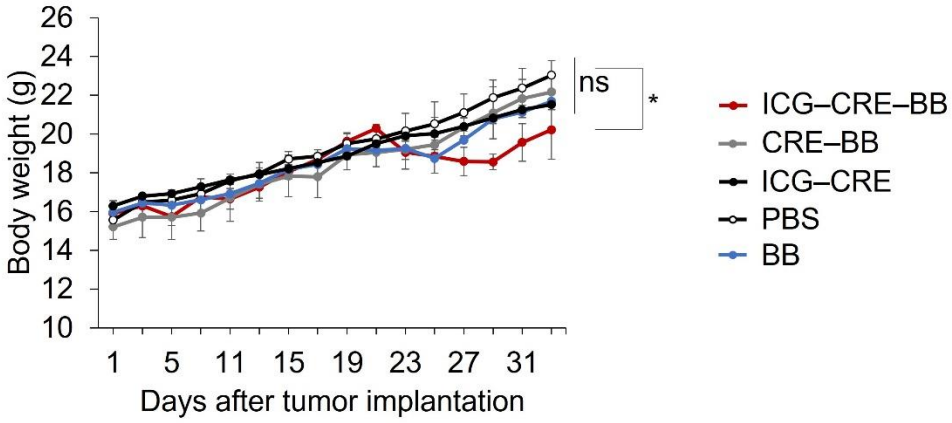

Figure 2.27 Average body weight of the mice after bacterial and control treatments during the treatment period. Data are represented as the mean ±SEM; n = 3 biologically independent mice. ns, not significant; *, $p < 0.05$.

2.3.3 Mechanism of tumor suppression

Simultaneously, mouse survival was examined each day (Figure 2.28). As compared to the control group (PBS and PBS + laser), the survival rate of mice with bacterial therapy (ICG−CRE−BB) in combination with laser was extended, showing a 100% survival rate for at least 45 days. The BB and BB+ laser groups also showed the same life prolongation (45 days) as the ICG−CRE−BB + laser group. The prolonging effects of CRE−BB + laser and CRE−BB groups were better than that of the control groups (PBS and PBS + laser).

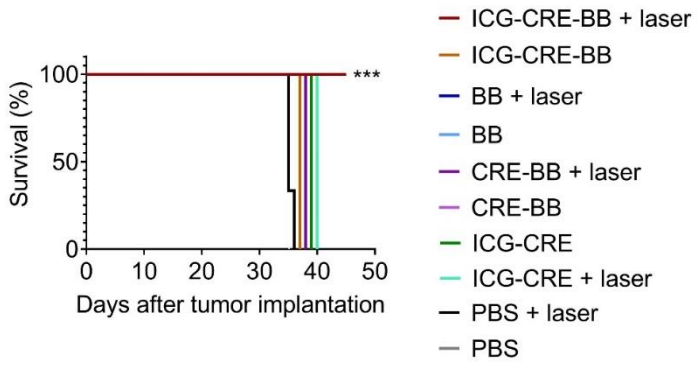

Figure 2.28 Kaplan–Meier survival curves of Conlon26-tumor-bearing mice (n = 3 biologically independent mice) after tumor implantation for 45 days. Statistical significance was calculated in comparison with PBS group. ****, $p < 0.0001$. The groups of ICG–CRE–BB + laser, BB + laser, and BB showed 100% survival rate at least for 45 days.

Besides, intratumoral injection of ICG−CRE−BB did not exhibit any toxicity in the tissues (Figure 2.29). Indeed, hematoxylin and eosin (HE) and terminal deoxynucleotidyl transferase (TdT)-mediated 2′-deoxyuridine, 5′-triphosphate (dUTP) nick end labeling (TUNEL) staining analyses showed that the tissues of ICG−CRE−BB post-intratumoral injection entirely resembles the control tissues (PBS buffer). Also, the mechanism of tumor regression by bacterial treatment was studied by injecting PBS alone or PBS suspensions containing ICG−CRE−BB, BB, or CRE−BB pre- and post-irradiation using HE, TUNEL, and immunohistochemical (IHC) staining analyses (Figure 2.30).

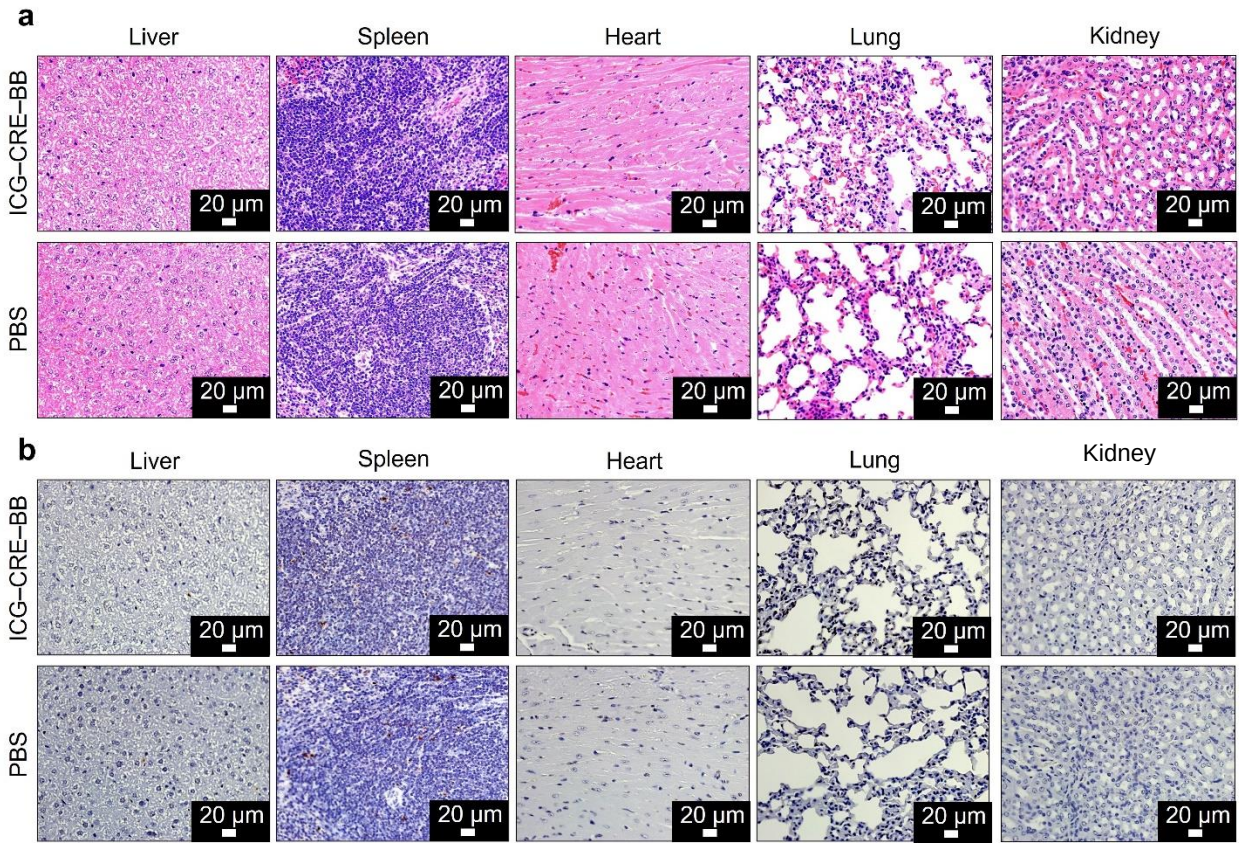

Figure 2.29 (a) H&E and (b) TUNEL stained conventional organ's tissues at day 2 after intratumoral injection of ICG–CRE–BB or PBS buffer.

The HE staining revealed tumor damage with intercellular fragmentation in the ICG−CRE−BB + laser, BB + laser, and BB treated tumor tissues. On the other hand, representative logical features, like tight arrangement and nuclear atypia, were observed in the control groups (PBS + laser, PBS, CRE−BB + laser, CRE−BB, and ICG−CRE−BB). Additionally, the ICG−CRE−BB + laser, BB + laser, and BB treated tissues exhibited increased cancer cell apoptosis, as indicated by the increase in TUNEL- and Caspase-3-positive cells. Nevertheless, the PBS+ laser, PBS, CRE−BB + laser, CRE−BB, and ICG−CRE−BB treated tissues did not exhibit apoptotic TUNEL and Caspase-3 color development within the tumor tissue (Figure 2.30).

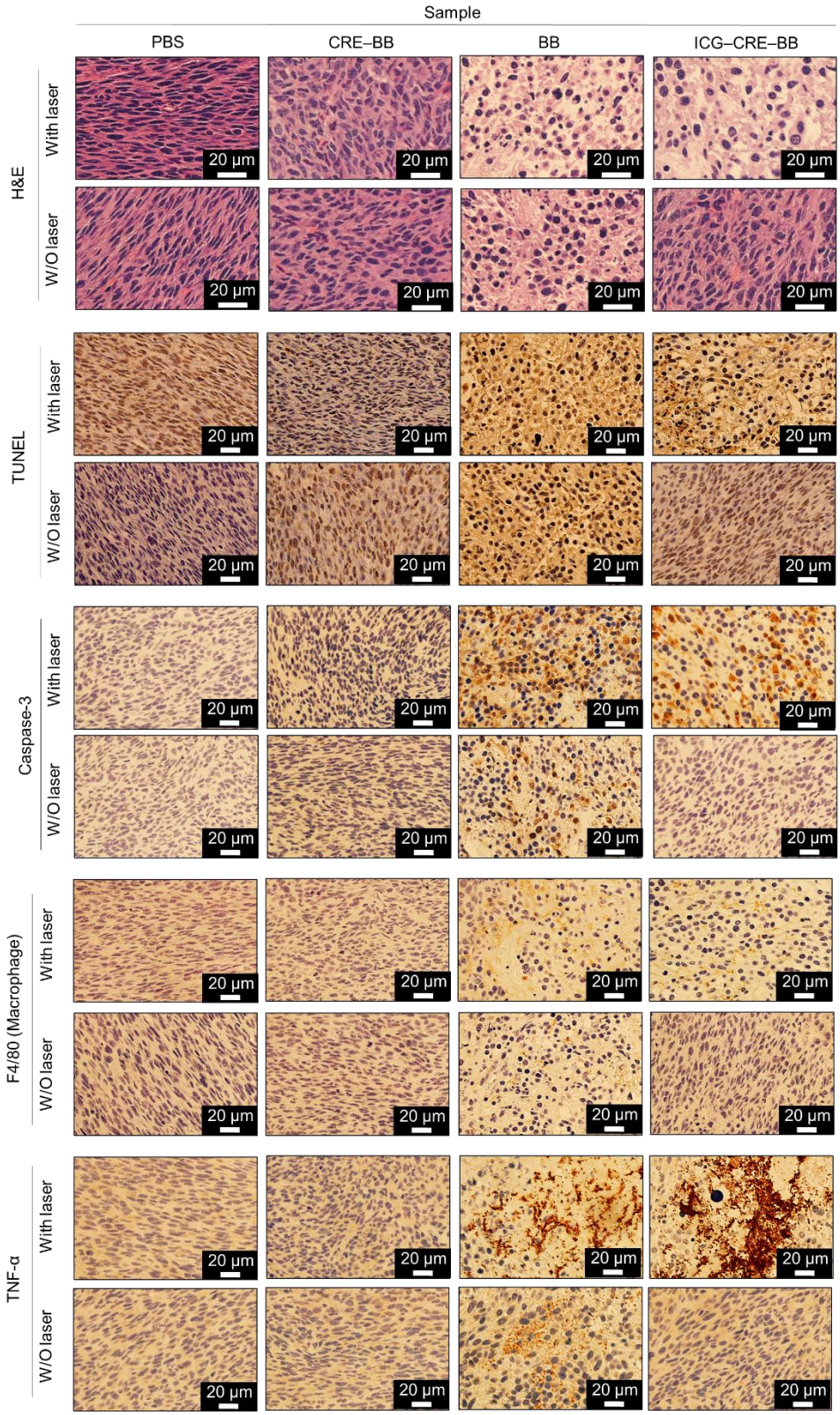

Figure 2.30 HE, TUNEL, and IHC (caspase-3, F4/80, and TNF-α) stained tumor tissues collected from different groups of mice on day 2 after treatment.

These results imply that ICG−CRE−BB + laser, BB and BB+ laser can effectively eliminate cancerous tumors via intracellular apoptotic caspase-3 signaling.

In order to understand the immunological responses associated with the observed tumor suppression in ICG−CRE−BB + laser, BB +laser, and BB groups, IHC staining of CD3 (T cell marker), and F4/80 (macrophage marker) was conducted (Figure 2.30 and Figure 2.31). The expression of F4/80 was observed only in the ICG−CRE−BB + laser, BB, and BB+ laser groups. In fact, only these groups exhibited significant expression of tumor necrosis factor-α (TNF-α), a multifunctional cytokine primarily secreted by the macrophages. Notably, the expression levels of TNF-α were significantly high in the ICG−CRE−BB + laser and BB + laser groups among them. Hence, we concluded that the drastic tumor regression caused by laser-induced ICG−CRE−BB was due to excess TNF-α expression and photothermal conversion. In fact, TNF-α regulates tumor cell proliferation and induces tumor suppression via tumor vasculature inhibition.[51] Also, IHC staining of CD3 expression associated with T cells did not show color change in all groups, and no significant differences observed among them (Figure 2.31).

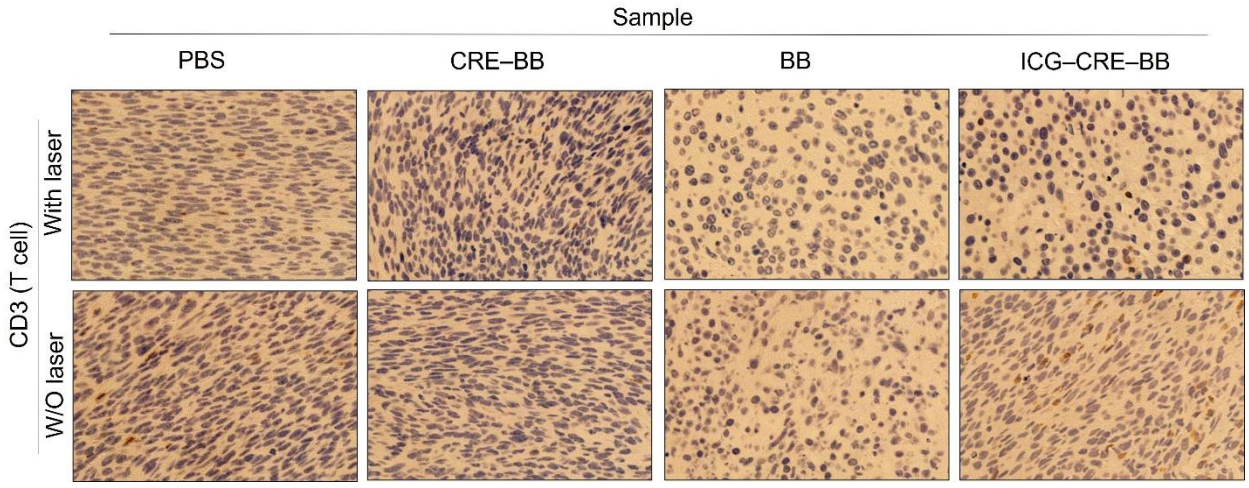

Figure 2.31 IHC-stained (CD3) tumor tissues collected from different groups of mice at day 2 after treatments.

To further reinforce the hypothesis, we examined in vitro TNF-α expression from a murine macrophage cell line (RAW264.7) using an enzyme-linked immuno sorbent (ELISA) assay (Figure 2.32). Significantly, an increased expression of TNF-α was observed following incubation with ICG−CRE−BB and laser irradiation along with lipopolysaccharide from *Escherichia coli* O157, as control. Collectively, we concluded that elimination of tumor was accomplished by laser-driven photothermal conversion of ICG−CRE−BB, with the assistance of macrophages (Figure 2.33).

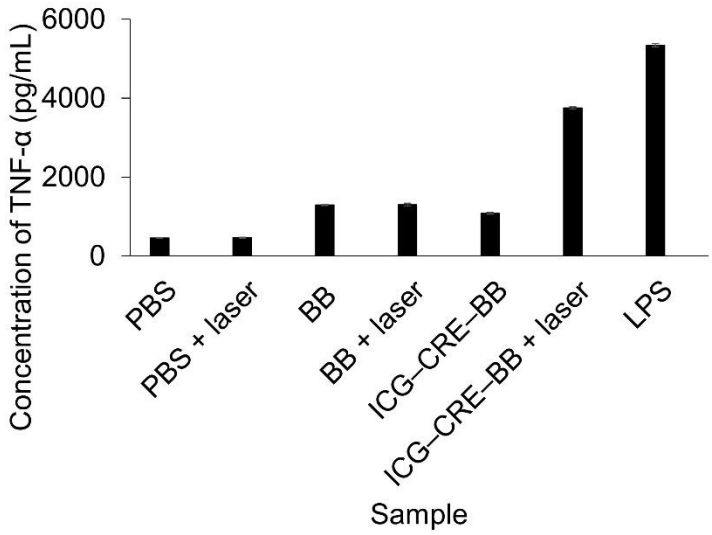

Figure 2.32 In vitro TNF-alpha expression from RAW264.7 cells (4×10^4 cells/mL) after incubation of nanoengineered bacteria or PBS for 4 h. Data are represented as mean ± SEM; n = 3 independent experiments. Concentrations of bacteria and ICG are 1×10^9 CFU/mL and 22.9 μg/mL. Laser power= 1.2 W (~ 61.1mW/mm^2). Laser irradiation time = 2 min.

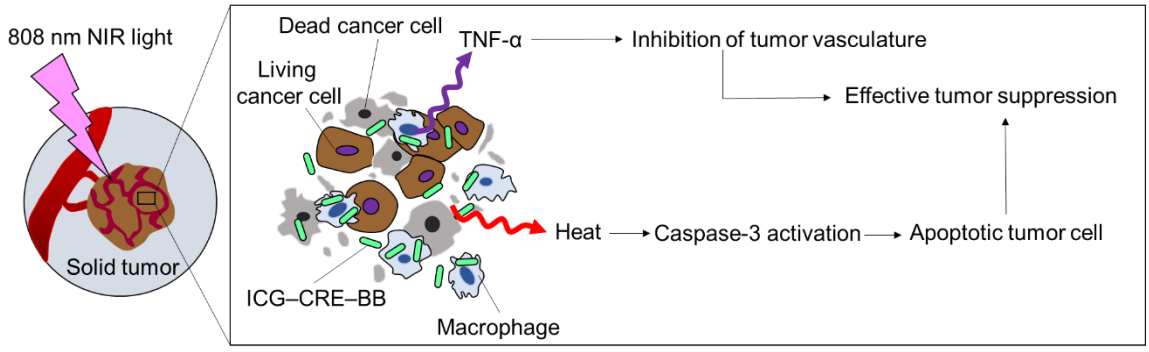

Figure 2.33 Schematic of the proposed mechanism of tumor suppression by NIR light-driven ICG−CRE−BB.

2.4 CONCLUSION

To summarize, we developed nanoparticle-functionalized bacteria utilizing a straightforward modification technique, and we analyzed their optical, structural, cytotoxic, and photothermal

properties in depth. As a result of nanoengineering with ICG-CRE, it was demonstrated that several desirable characteristics, including photothermal conversion, fluorescence, and attenuation, could be introduced to bacteria while maintaining their inherent properties. Compared to previous methods, this approach for enhancing the optical properties of bacteria through nanoengineering is distinct in its use of FDA-approved, biocompatible chemicals and its reliance on practical *Bifidobacterium* microbial technology. Furthermore, the preparation method is straightforward. The demonstration of the potential application of nanoengineered bacteria (CRE−ICG−BB) was done by performing near-infrared fluorescence imaging of tumors in mice. Additionally, the use of near-infrared laser-induced CRE−ICG−BB demonstrated exceptional antitumor efficacy, which was augmented by immune responses. Hence, our research offers a nanoengineering strategy to bestow living bacteria with desirable traits, such as photothermal conversion, fluorescence, and attenuation. Moreover, it was shown that the synthesized nanoparticle-functionalized bacteria exhibited robust tumor suppression capabilities and high fluorescence expression in biological systems, making them a promising candidate for cancer immunotheranostics.

2.5 REFERENCES

(1) Yahya, E. B.; Alqadhi, A. M. Recent Trends in Cancer Therapy: A Review on the Current State of Gene Delivery. *Life Sci.* **2021**, *269*, 119087.

(2) Forbes, N. S. Engineering the Perfect (Bacterial) Cancer Therapy. *Nat. Rev. Cancer* **2010**, *10* (11), 785–794.

(3) DeLucia, D. C.; Lee, J. K. Development of Cancer Immunotherapies. *Cancer Treat. Res.* **2022**, *183*, 1 – 48.

(4) Chen, J.; Li, T.; Liang, J.; Huang, Q.; Huang, J.-D.; Ke, Y.; Sun, H. Current Status of Intratumour Microbiome in Cancer and Engineered Exogenous Microbiota as a Promising Therapeutic Strategy. *Biomed. Pharmacother.* **2022**, *145*.

(5) Chen, F.; Zang, Z.; Chen, Z.; Cui, L.; Chang, Z.; Ma, A.; Yin, T.; Liang, R.; Han, Y.; Wu, Z.; Zheng, M.; Liu, C.; Cai, L. Nanophotosensitizer-Engineered Salmonella Bacteria with Hypoxia Targeting and Photothermal-Assisted Mutual Bioaccumulation for Solid Tumor Therapy. *Biomaterials* **2019**, *214*, 119226.

(6) Yu, Y.; Lin, S.; Chen, Z.; Qin, B.; He, Z.; Cheng, M.; Sun, M.; Sun, J. Bacteria-Driven Bio-Therapy: From Fundamental Studies to Clinical Trials. *Nano Today* **2023**, *48*.

(7) Cao, X. Intestinal Inflammation Induced by Oral Bacteria. *Science* **2017**, *358* (6361), 308–309.

(8) Sun, J. Enteric Bacteria and Cancer Stem Cells. *Cancers (Basel).* **2010**, *3* (1), 285–297.

(9) Massier, L.; Chakaroun, R.; Tabei, S.; Crane, A.; Didt, K. D.; Fallmann, J.; von Bergen, M.; Haange, S.-B.; Heyne, H.; Stumvoll, M.; Gericke, M.; Dietrich, A.; Blüher, M.; Musat, N.; Kovacs, P. Adipose Tissue Derived Bacteria Are Associated with Inflammation in Obesity and Type 2 Diabetes. *Gut* **2020**, *69* (10), 1796–1806.

(10) Wu, L.; Bao, F.; Li, L.; Yin, X.; Hua, Z. Bacterially Mediated Drug Delivery and Therapeutics: Strategies and Advancements. *Adv. Drug Deliv. Rev.* **2022**, *187*, 114363.

(11) Watson, A. J. M.; Collins, P. Treatment of Inflammatory Bowel Disease with Genetically Engineered Bacteria. *Gastroenterology* **2010**, *139* (2), 685–687.

(12) Chen, Y.; Liu, X.; Guo, Y.; Wang, J.; Zhang, D.; Mei, Y.; Shi, J.; Tan, W.; Zheng, J. H. Genetically Engineered Oncolytic Bacteria as Drug Delivery Systems for Targeted Cancer Theranostics. *Acta Biomater.* **2021**, *124*, 72–87.

(13) Hoffman, R. M. *Bacterial Therapy of Cancer: Methods and Protocols*; Hoffman, R. M., Ed.; Humana Press: New York, 2016.

(14) Zhou, S.; Gravekamp, C.; Bermudes, D.; Liu, K. Tumour-Targeting Bacteria Engineered to Fight Cancer. *Nat. Rev. Cancer* **2018**, *18* (12), 727–743.

(15) Brown, J. M.; Wilson, W. R. Exploiting Tumour Hypoxia in Cancer Treatment. *Nat. Rev. Cancer* **2004**, *4* (6), 437–447.

(16) Duong, M. T.-Q.; Qin, Y.; You, S.-H.; Min, J.-J. Bacteria-Cancer Interactions: Bacteria-Based Cancer Therapy. *Exp. Mol. Med.* **2019**, *51* (12), 1–15.

(17) Din, M. O.; Danino, T.; Prindle, A.; Skalak, M.; Selimkhanov, J.; Allen, K.; Julio, E.; Atolia, E.; Tsimring, L. S.; Bhatia, S. N.; Hasty, J. Synchronized Cycles of Bacterial Lysis for in Vivo Delivery. *Nature* **2016**, *536* (7614), 81–85.

(18) Bourdeau, R. W.; Lee-Gosselin, A.; Lakshmanan, A.; Farhadi, A.; Kumar, S. R.; Nety, S. P.; Shapiro, M. G. Acoustic Reporter Genes for Noninvasive Imaging of Microorganisms in Mammalian Hosts. *Nature* **2018**, *553* (7686), 86–90.

(19) Chowdhury, S.; Castro, S.; Coker, C.; Hinchliffe, T. E.; Arpaia, N.; Danino, T. Programmable Bacteria Induce Durable Tumor Regression and Systemic Antitumor Immunity. *Nat. Med.* **2019**, *25* (7), 1057–1063.

(20) Georghiou, P. E.; Blagden, P. A.; Winsor, L.; Williams, D. T. Spontaneous Revertants in Modified S. Typhimurium Mutagenicity Tests Employing Elevated Numbers of the Tester Strain. *Mutat. Res.* **1989**, *225* (1–2), 33–39.

(21) Felfoul, O.; Mohammadi, M.; Taherkhani, S.; de Lanauze, D.; Zhong Xu, Y.; Loghin, D.; Essa, S.; Jancik, S.; Houle, D.; Lafleur, M.; Gaboury, L.; Tabrizian, M.; Kaou, N.; Atkin, M.; Vuong, T.; Batist, G.; Beauchemin, N.; Radzioch, D.; Martel, S. Magneto-Aerotactic Bacteria Deliver Drug-Containing Nanoliposomes to Tumour Hypoxic Regions. *Nat. Nanotechnol.* **2016**, *11* (11), 941–947.

(22) Zheng, D.-W.; Chen, Y.; Li, Z.-H.; Xu, L.; Li, C.-X.; Li, B.; Fan, J.-X.; Cheng, S.-X.; Zhang, X.-Z. Optically-Controlled Bacterial Metabolite for Cancer Therapy. *Nat. Commun.* **2018**, *9* (1), 1680.

(23) Suh, S.; Jo, A.; Traore, M. A.; Zhan, Y.; Coutermarsh-Ott, S. L.; Ringel-Scaia, V. M.; Allen, I. C.; Davis, R. M.; Behkam, B. Nanoscale Bacteria-Enabled Autonomous Drug Delivery System (NanoBEADS) Enhances Intratumoral Transport of Nanomedicine. *Adv. Sci. (Weinheim, Baden-Wurttemberg, Ger.* **2019**, *6* (3), 1801309.

(24) Chen, W.; Guo, Z.; Zhu, Y.; Qiao, N.; Zhang, Z.; Sun, X. Combination of Bacterial-Photothermal Therapy with an Anti-PD-1 Peptide Depot for Enhanced Immunity against Advanced Cancer. *Adv. Funct. Mater.* **2020**, *30* (1), 1906623.

(25) Chen, W.; Wang, Y.; Qin, M.; Zhang, X.; Zhang, Z.; Sun, X.; Gu, Z. Bacteria-Driven Hypoxia Targeting for Combined Biotherapy and Photothermal Therapy. *ACS Nano* **2018**, *12* (6), 5995–6005.

(26) Luo, C.-H.; Huang, C.-T.; Su, C.-H.; Yeh, C.-S. Bacteria-Mediated Hypoxia-Specific Delivery of Nanoparticles for Tumors Imaging and Therapy. *Nano Lett.* **2016**, *16* (6), 3493–3499.

(27) Yang, X.; Komatsu, S.; Reghu, S.; Miyako, E. Optically Activatable Photosynthetic Bacteria-Based Highly Tumor Specific Immunotheranostics. *Nano Today* **2021**, *37*, 101100.

(28) Kumar, N.; Fazal, S.; Miyako, E.; Matsumura, K.; Rajan, R. Avengers against Cancer: A New Era of Nano-Biomaterial-Based Therapeutics. *Mater. Today* **2021**, *51*, 317–349.

(29) Riley, R. S.; June, C. H.; Langer, R.; Mitchell, M. J. Delivery Technologies for Cancer Immunotherapy. *Nat. Rev. Drug Discov.* **2019**, *18* (3), 175–196.

(30) Zhang, C.; Pu, K. Molecular and Nanoengineering Approaches towards Activatable Cancer Immunotherapy. *Chem. Soc. Rev.* **2020**, *49* (13), 4234–4253.

(31) Wei, B.; Pan, J.; Yuan, R.; Shao, B.; Wang, Y.; Guo, X.; Zhou, S. Polarization of Tumor-Associated Macrophages by Nanoparticle-Loaded Escherichia Coli Combined with Immunogenic Cell Death for Cancer Immunotherapy. *Nano Lett.* **2021**, *21* (10), 4231–4240.

(32) Sasaki, T.; Fujimori, M.; Hamaji, Y.; Hama, Y.; Ito, K.-I.; Amano, J.; Taniguchi, S. Genetically Engineered Bifidobacterium Longum for Tumor-Targeting Enzyme-Prodrug Therapy of Autochthonous Mammary Tumors in Rats. *Cancer Sci.* **2006**, *97* (7), 649–657.

(33) Fialho, A., Chakrabarty, A. *Emerging Cancer Therapy: Microbial Approaches and Biotechnological Tools*; Fialho, A., Chakrabarty, A., Eds.; Wiley: New York, 2010.

(34) Yu, Y.; Yang, X.; Reghu, S.; Kaul, S. C.; Wadhwa, R.; Miyako, E. Photothermogenetic Inhibition of Cancer Stemness by Near-Infrared-Light-Activatable Nanocomplexes. *Nat. Commun.* **2020**, *11* (1), 4117.

(35) Chechetka, S. A.; Yu, Y.; Zhen, X.; Pramanik, M.; Pu, K.; Miyako, E. Light-Driven Liquid Metal Nanotransformers for Biomedical Theranostics. *Nat. Commun.* **2017**, *8* (1), 15432.

(36) Miyako, E.; Kono, K.; Yuba, E.; Hosokawa, C.; Nagai, H.; Hagihara, Y. Carbon Nanotube–Liposome Supramolecular Nanotrains for Intelligent Molecular-Transport Systems. *Nat. Commun.* **2012**, *3* (1), 1226.

(37) Sevieri, M.; Silva, F.; Bonizzi, A.; Sitia, L.; Truffi, M.; Mazzucchelli, S.; Corsi, F. Indocyanine Green Nanoparticles: Are They Compelling for Cancer Treatment? *Front. Chem.* **2020**, *8*.

(38) Gelderblom, H.; Verweij, J.; Nooter, K.; Sparreboom, A. Cremophor EL: The Drawbacks and Advantages of Vehicle Selection for Drug Formulation. *Eur. J. Cancer* **2001**, *37* (13), 1590–1598.

(39) Narayanan, K.; Lee, C. W.; Radu, A.; Sim, E. U. H. Escherichia Coli Bactofection Using Lipofectamine. *Anal. Biochem.* **2013**, *439* (2), 142–144.

(40) Iversen, T.-G.; Skotland, T.; Sandvig, K. Endocytosis and Intracellular Transport of Nanoparticles: Present Knowledge and Need for Future Studies. *Nano Today* **2011**, *6* (2), 176–185.

(41) Ma, R.; Alifu, N.; Du, Z.; Chen, S.; Heng, Y.; Wang, J.; Zhu, L.; Ma, C.; Zhang, X. Indocyanine Green-Based Theranostic Nanoplatform for NIR Fluorescence Image-Guided Chemo/Photothermal Therapy of Cervical Cancer. *Int. J. Nanomedicine* **2021**, *16*, 4847–4861.

(42) Shivaji, S.; Prakash, J. S. S. How Do Bacteria Sense and Respond to Low Temperature? *Arch. Microbiol.* **2010**, *192* (2), 85–95.

(43) Egloff-Juras, C.; Bezdetnaya, L.; Dolivet, G.; Lassalle, H.-P. NIR Fluorescence-Guided Tumor Surgery: New Strategies for the Use of Indocyanine Green. *Int. J. Nanomedicine* **2019**, *14*, 7823–7838.

(44) Hessel, C. M.; Pattani, V. P.; Rasch, M.; Panthani, M. G.; Koo, B.; Tunnell, J. W.; Korgel, B. A. Copper Selenide Nanocrystals for Photothermal Therapy. *Nano Lett.* **2011**, *11* (6), 2560–2566.

(45) Li, Y.; Bai, G.; Zeng, S.; Hao, J. Theranostic Carbon Dots with Innovative NIR-II Emission for in Vivo Renal-Excreted Optical Imaging and Photothermal Therapy. *ACS Appl. Mater. Interfaces* **2019**, *11* (5), 4737–4744.

(46) Li, J.; Pu, K. Semiconducting Polymer Nanomaterials as Near-Infrared Photoactivatable Protherapeutics for Cancer. *Acc. Chem. Res.* **2020**, *53* (4), 752–762.

(47) D'souza, A. A.; Shegokar, R. Polyethylene Glycol (PEG): A Versatile Polymer for Pharmaceutical Applications. *Expert Opin. Drug Deliv.* **2016**, *13* (9), 1257–1275.

(48) Rossi-Fanelli, A.; Cavaliere, R., Mondovi, B., Moricca, G. *Selective Heat Sensitivity of Cancer Cells*; Springer: Netherlands, 1977.

(49) Cossart, P.; Helenius, A. Endocytosis of Viruses and Bacteria. *Cold Spring Harb. Perspect. Biol.* **2014**, *6* (8).

(50) Yi, X.; Zhou, H.; Chao, Y.; Xiong, S.; Zhong, J.; Chai, Z.; Yang, K.; Liu, Z. Bacteria-Triggered Tumor-Specific Thrombosis to Enable Potent Photothermal Immunotherapy of Cancer. *Sci. Adv.* **2020**, *6* (33), eaba3546.

(51) Carswell, E. A.; Old, L. J.; Kassel, R. L.; Green, S.; Fiore, N.; Williamson, B. An Endotoxin-Induced Serum Factor That Causes Necrosis of Tumors. *Proc. Natl. Acad. Sci. U. S. A.* **1975**, *72* (9), 3666–3670.

(52) Wei, B.; Pan, J.; Yuan, R.; Shao, B.; Wang, Y.; Guo, X.; Zhou, S. Correction to "Polarization of Tumor-Associated Macrophages by Nanoparticle Loaded Escherichia Coli Combined with Immunogenic Cell Death for Cancer Immunotherapy." *Nano Lett.* **2021**, *21* (13), 5905.

(53) Xing, J.; Yin, T.; Li, S.; Xu, T.; Ma, A.; Chen, Z.; Luo, Y.; Lai, Z.; Lv, Y.; Pan, H.; Liang, R.; Wu, X.; Zheng, M.; Cai, L. Sequential Magneto-Actuated and Optics-Triggered Biomicrorobots for Targeted Cancer Therapy. *Adv. Funct. Mater.* **2021**, *31* (11), 2008262.

(54) Yin, T.; Diao, Z.; Blum, N. T.; Qiu, L.; Ma, A.; Huang, P. Engineering Bacteria and Bionic Bacterial Derivatives with Nanoparticles for Cancer Therapy. *Small* **2022**, *18* (12), 2104643.

(55) Huang, X.; Pan, J.; Xu, F.; Shao, B.; Wang, Y.; Guo, X.; Zhou, S. Bacteria-Based Cancer Immunotherapy. *Adv. Sci.* **2021**, *8* (7), 2003572.

(56) Deschênes, L.; Ells, T. Bacteria-Nanoparticle Interactions in the Context of Nanofouling. *Adv. Colloid Interface Sci.* **2020**, *277*, 102106.

(57) Hajipour, M. J.; Fromm, K. M.; Ashkarran, A. A.; Jimenez de Aberasturi, D.; de Larramendi, I. R.; Rojo, T.; Serpooshan, V.; Parak, W. J.; Mahmoudi, M. Antibacterial Properties of Nanoparticles. *Trends Biotechnol.* **2012**, *30* (10), 499–511.

(58) Miller, K. P.; Wang, L.; Benicewicz, B. C.; Decho, A. W. Inorganic Nanoparticles Engineered to Attack Bacteria. *Chem. Soc. Rev.* **2015**, *44* (21), 7787–7807.

(59) Reghu, S.; Miyako, E. Nanoengineered Bifidobacterium Bifidum with Optical Activity for Photothermal

Cancer Immunotheranostics. *Nano Lett.* **2022**, *22* (5), 1880–1888.

(60) Alberts, B.; Heald, R.; Johnson, A.; Morgan, D. . R. M. . W. W. N. *Molecular Biology of the Cell, 7th Edition*; New York, 2022.

(61) Wang, L.; Shen, Q.; Liao, H.; Fu, H.; Wang, Q.; Yu, J.; Zhang, W.; Chen, C.; Dong, Y.; Yang, X.; Guo, Q.; Zhang, J.; Zhang, J.; Zhang, W.; Lin, H.; Duan, Y. Multi-Arm PEG/Peptidomimetic Conjugate Inhibitors of DR6/APP Interaction Block Hematogenous Tumor Cell Extravasation. *Adv. Sci. (Weinheim, Baden-Wurttemberg, Ger.* **2021**, *8* (11), e2003558.

(62) Sun, X.; Yu, W.; Pang, Q.; Hu, T. Conjugation Reaction with 8-Arm PEG Markedly Improves the Immunogenicity of Mycobacterium Tuberculosis CFP10-TB10.4 Fusion Protein. *Bioconjug. Chem.* **2017**, *28* (6), 1658–1668.

(63) Lee, S.; Kim, K.; Kumar, T. S.; Lee, J.; Kim, S. K.; Lee, D. Y.; Lee, Y.; Byun, Y. Synthesis and Biological Properties of Insulin−Deoxycholic Acid Chemical Conjugates. *Bioconjug. Chem.* **2005**, *16* (3), 615–620.

(64) Kato, K.; Itoh, C.; Yasukouchi, T.; Nagamune, T. Rapid Protein Anchoring into the Membranes of Mammalian Cells Using Oleyl Chain and Poly(Ethylene Glycol) Derivatives. *Biotechnol. Prog.* **2004**, *20* (3), 897–904.

(65) Zhao, Y.; Fan, M.; Chen, Y.; Liu, Z.; Shao, C.; Jin, B.; Wang, X.; Hui, L.; Wang, S.; Liao, Z.; Ling, D.; Tang, R.; Wang, B. Surface-Anchored Framework for Generating RhD-Epitope Stealth Red Blood Cells. *Sci. Adv.* **2020**, *6* (12), eaaw9679.

(66) Becicka, W. M.; Bielecki, P. A.; Lorkowski, M. E.; Moon, T. J.; Zhang, Y.; Atukorale, P. U.; Covarrubias, G.; Karathanasis, E. The Effect of PEGylation on the Efficacy and Uptake of an Immunostimulatory Nanoparticle in the Tumor Immune Microenvironment. *Nanoscale Adv.* **2021**, *3* (17), 4961–4972.

(67) Veronese, F. M.; Mero, A. The Impact of PEGylation on Biological Therapies. *BioDrugs* **2008**, *22* (5), 315–329.

(68) Uher, O.; Caisova, V.; Hansen, P.; Kopecky, J.; Chmelar, J.; Zhuang, Z.; Zenka, J.; Pacak, K. Coley's Immunotherapy Revived: Innate Immunity as a Link in Priming Cancer Cells for an Attack by Adaptive Immunity. *Semin. Oncol.* **2019**, *46* (4–5), 385–392.

(69) Kaiser, E.; Colescott, R. L.; Bossinger, C. D.; Cook, P. I. Color Test for Detection of Free Terminal Amino Groups in the Solid-Phase Synthesis of Peptides. *Anal. Biochem.* **1970**, *34* (2), 595–598.

(70) Ito, F.; Ernstoff, M. *Immune Checkpoint Inhibitors in Cancer, 1st Edition*; Elsevier: Amsterdam, Nederlands, 2018.

(71) De Sousa Linhares, A.; Battin, C.; Jutz, S.; Leitner, J.; Hafner, C.; Tobias, J.; Wiedermann, U.; Kundi, M.; Zlabinger, G. J.; Grabmeier-Pfistershammer, K.; Steinberger, P. Therapeutic PD-L1 Antibodies Are More Effective than PD-1 Antibodies in Blocking PD-1/PD-L1 Signaling. *Sci. Rep.* **2019**, *9* (1), 11472.

(72) André, M.; Besse, S.; Chezal, J.-M.; Mounetou, E. PEGylation Enhances the Tumor Selectivity of Melanoma-Targeted Conjugates. *Org. Biomol. Chem.* **2015**, *13* (2), 388–397.

(73) Suk, J. S.; Xu, Q.; Kim, N.; Hanes, J.; Ensign, L. M. PEGylation as a Strategy for Improving Nanoparticle-Based Drug and Gene Delivery. *Adv. Drug Deliv. Rev.* **2016**, *99* (Pt A), 28–51.

(74) Martínez-Lostao, L.; Anel, A.; Pardo, J. How Do Cytotoxic Lymphocytes Kill Cancer Cells? *Clin. Cancer Res.* **2015**, *21* (22), 5047–5056.

Chapter 3 Cancer Immunotheranostics Using Bioactive Nanocoated Photosynthetic Bacterial Complexes

3.1 INTRODUCTION

For the past few decades, effectively treating malignant tumors through therapy has proven to be a difficult task in the field of cancer treatment.[1] To address limitations associated with conventional treatments, anti-cancer drugs, immune checkpoint inhibitors, oncolytic viruses, nanoparticles, and immune cells could be used in combination with bacteria therapy. Several limitations exist in current treatments, including their inability to target specific hypoxic tumors, produce independent biomarkers, penetrate deep tissues, have programmable therapeutic efficacy, and maintain affordability in production.[2] Attenuated bacteria like *Escherichia*, *Salmonella*, *Listeria* and *Clostridium* are currently being tested in clinical studies as potential immunotherapies for different stages of cancer.

Bacterial therapy can be enhanced further by nanotechnology[3–12] and genetic engineering[13–19]. Yet, there is a genuine concern for patients regarding the possibility of acquiring antibiotic resistance or mutations that may reverse the engineered bacterial phenotype. In comparison, nanotechnology methods often involve complex techniques. Because of the severe chemical modifications induced by the multivalent covalent interactions of bioactive nanoparticles with the bacterial membrane and/or rigid nanocoating of the entire microorganism, the approaches may hinder the biological functions, including the viability and proliferation of the bacteria. The impact and toxicity of nanoparticles on the biological functions of bacteria are reported.[20–22] To develop an advanced therapeutic approach that enhances functionality and biocompatibility, while preserving the inherent medicinal properties of bacteria, it is important to carry out simple and moderate chemical functionalization of natural bacteria, without resorting to genetic engineering.[23]

Some purple photosynthetic bacteria (PPSB) possess promising traits for overcoming these deficiencies and restrictions. Our recent findings indicate that the bacteriochlorophyll (BChl) nanoring-embedded light-harvesting nanocomplexes present in natural PPSBs *Rhodopseudomonas palustris* (RP) and *Blastochloris viridis* can be activated in a spatiotemporally controlled manner using near-infrared (NIR) light that can penetrate tissues. This finding demonstrates the potential of these complexes to serve as valuable agents for targeted optical cancer immunotheranostics.[24] Indeed, because of its limited invasiveness, deep tissue penetrability, and ease of operation, NIR light is a preferred energy source for wireless control of smart anticancer therapy.[25,26] Nevertheless, the NIR light's penetration depth, which cannot exceed 10 cm in living tissue, does not allow for the efficient elimination of entire tumour and metastatic cancer cells. We anticipate that chemical functionalization of PPSB might improve NIR-driven bacterial therapeutics by molecularly engineering bacteria to serve as efficient drug carriers immunostimulators, and photosensitizers.

In this work, we investigated several PPSBs as "hardware" for chemical modification of bacterial membranes via covalent or non-covalent techniques employing functional biomolecules and polyethylene glycol (PEG) derivatives to establish a high-performance anticancer theranostic bacterial modality. We demonstrated that PPSBs can be successfully and efficiently functionalized with bioactive compounds via simple PEGylation. In vitro and in vivo, the functional PPSB complexes showed excellent optical and physiological features. Furthermore, the chemically functionalized NIR light-induced functional PPSBs exhibited remarkable innate fluorescence and potent photothermal conversion properties, which led to specific tumor-targeting NIR fluorescence and substantial anticancer effects in a syngeneic murine colon cancer model. The synthetic molecules utilized in the chemical functionalization also facilitated immunological regulation. By

combining activatable real-time NIR imaging with tumor-specific photo-thermal immunoregulation of functional PPSBs, this approach offers a novel strategy for precise and efficient photo-theranostics.

3.2 Materials and Methods

3.2.1 Bacterial strains and growth

Rhodopseudomonas palustris (RP) (NBRC16661), *Pararhodospirillum oryzae* (NBRC107573), *Pararhodospirillum sulfurexigens* (NBRC104433), *Rhodomicrobium udaipurense* (NBRC109057), *Rhodomicrobium vannielii* (NBRC100050), *Afifella marina* (NBRC100434), *Rhodobacter sphaeroides* (NBRC12203), *Rhodobacter blasticus* (NBRC16437), *Rhodocista centenaria* (NBRC16667), and *Rhodobacter capsulatus* (NBRC16435) were purchased from the National Institute of Technology and Evaluation Biological Resource Center (NBRC) (Chiba, Japan). *Rhodovulum sulfidophilum* (ATCC35886) was obtained from the American Type Culture Collection (ATCC) (Manassas, VA, USA). All bacterial strains in this study were grown anaerobically in 543 ATCC *Rhodopseudomonas* medium under tungsten lamps at 26–30 ℃. All bacterial culture reagents were purchased from FUJIFILM Wako Pure Chemical (Osaka, Japan) and Nacalai Tesque (Kyoto, Japan).

3.2.2 Optical characterizations

The absorption and fluorescent spectra of various bacteria and functional bacterial hybrids were obtained at 20 ºC using a UV–vis–near-infrared (NIR) spectrophotometer (V-730 BIO; Jasco, Tokyo, Japan) and fluorescence spectrometer (FP-8600 NIR Spectrofluorometer; Jasco, Tokyo, Japan), respectively.

3.2.3 Photothermal conversion tests

Bacterial dispersed solution (100 μL) or PBS buffer (100 μL) were irradiated using an 808 nm NIR laser (spot diameter, approximately 5 mm) (CivilLaser, Hangzhou, Zhejiang, China) at 1.2 W (~6.1 W cm^{-2}) or 0.6 W (~3.1 W cm^{-2}) at different time points (1, 2, 3, 4, and 5 min). The temperature of the samples was measured in real time using a temperature sensor (AD-5601A; A&D, Tokyo, Japan).

3.2.4 Cell culture and cell viability assays

Murine colorectal carcinoma cells (Colon26) and human normal diploid fibroblasts (MRC5) were purchased from the Japanese Collection of Research Bioresources Cell Bank (Tokyo, Japan). Murine macrophage (RAW264.7) and human diploid (normal human fibroblast) (WI38) cell lines were obtained from Riken Bio Resource Center (Ibaraki, Japan). Roswell Park Memorial Institute 1640 medium (Nacalai Tesque) containing 10% fetal bovine serum (FBS; Biowest, Nuaillé, France) and 1% penicillin-streptomycin (Pen Strep; Gibco, Grand Island, NY, USA), was used to culture Colon26 cells. Minimum Essential Medium without essential amino acids (Nacalai Tesque, Inc. Kyoto, Japan) containing 10% FBS and 1% Pen-Strep was used to culture WI38 cells. Dulbecco's Modified Eagle's Medium (Gibco, Grand Island, NY, USA) containing 10% FBS and 1% Pen-Strep was used to culture RAW264.7 cells. These cell lines were cultured in a 37 °C incubator with 5% CO_2. Cell viability was assessed using Cell Counting Kit-8 (CCK-8) (Dojindo Laboratories, Kumamoto, Japan) according to the manufacturer's instructions. Briefly, 7×10^3 cells $well^{-1}$ of Colon26, MRC5, RAW264.7, and WI38 cells were seeded in 96-well plates and allowed to adhere overnight. The cells were then exposed to various bacteria for 4 h in a 37 °C incubator with 5% CO_2. After washing with fresh media, the cells were incubated with the CCK-

8 solution for 3 h in a 37 °C incubator. Absorbance at 450/690 nm was then determined using a microplate reader (Infinite 200 PRO M Plex; Tecan, Männedorf, Switzerland).

3.2.5 Heat mapping

The data of heat mapping of Figure 3.1a was prepared using the software (GraphPad Prism 9; MDF, Tokyo, Japan). Briefly, cytotoxicity was obtained by assigning PBS, that showed no cytotoxicity, as the standard value (100%) to compare with various bacterial strains when MRC5 cell was treated with the highest bacterial concentration (3×10^9 CFU mL^{-1}). Average cytotoxicity of PPSBs (NBRC16661, NBRC107573, NBRC104433, NBRC109057, NBRC100050, ATCC35886, NBRC100434, NBRC12203, NBRC16437, NBRC16667, and NBRC16435) were 95, 2.9, 17.7, 54.5, 0, 80.9, 17.7, 57.6, 80, 4.1, and 80%.

Besides, fluorescence was measured by calculation of the fluorescent intensities (top peaks) in a range of values from all excitation frequency of 785-850 nm for each bacterial strain. RP exhibited the highest fluorescent property among all strains. Thus, RP was assigned as the standard value (100%) to compare with other bacterial strains. Fluorescence values of each PPSB (NBRC107573, NBRC104433, NBRC109057, NBRC100050, ATCC35886, NBRC100434, NBRC12203, NBRC16437, NBRC16667, and NBRC16435) and PBS were calculated 58.5, 86.3, 38.8, 76.0, 15.3, 1.1, 22.4, 13.7, 1.6, 10.9 and 0% by the following formula.

Fluorescence (%) = [Total FL intensities of each bacterium in a range of values from 785-850 nm]/ [Total FL intensities of RP strain in a range of values from 785-850 nm] × 100

Meanwhile, photothermal conversions of various PPSBs were calculated from ΔT after 808-nm laser irradiation for 2 min. RP also showed the highest ΔT so that the photothermal conversion value of RP was adjusted 100% as the standard to compare with other strains. Photothermal conversion of PPSBs (NBRC107573, NBRC104433, NBRC109057, NBRC100050, ATCC35886,

NBRC100434, NBRC12203, NBRC16437, NBRC16667, and NBRC16435) and PBS were calculated to 95.5, 93.0, 86.6, 70.7, 59.2, 42.5, 38.1, 30.2, 30.2, 19.6, and 6.7% by the following formula.

Photothermal conversion (%) = [ΔT of each bacterium after 808-nm laser irradiation for 2 min]/ [ΔT of RP after 808-nm laser irradiation for 2 min] × 100

3.2.6 PEGylated bacteria preparation

The PEG derivatives were synthesized as follows. Briefly, 4-arm PEG succinimidyl glutarate ester, 20K (4-arm) (10 mg mL^{-1}; Biopharma PEG Scientific, Watertown, MA, USA), 8-arm PEG succinimidyl carboxy methyl ester, 40K (8-arm) (10 mg mL^{-1}; Biopharma PEG Scientific), α-succinimidyloxysuccinyl-ω-methoxy, polyoxyethylene (50CS) (10 mg mL^{-1}; SUNBRIGHT ME-050 CS, NOF Corporation, Tokyo, Japan), Cremophor® EL (CRE) (5%; Nacalai Tesque), or biocompatible anchor for membrane (BAM) (10 mg mL^{-1}; SUNBRIGHT OE-040 CS, NOF Corporation) were added in PBS and sonicated for 1 min at 20 ºC using a bath-type sonicator (Bransonic M2800-J; Branson Ultrasonics, Brookfield, CT, USA). BAM was incubated at 20 ºC for 24 h to deactivate the N-hydroxysuccinimide groups of the PEG moiety before conjugation with RP. RP (3×10^9 CFU mL^{-1}) was centrifuged (2,300 × g, for 5 min at 4 ℃) to obtain a pellet, and the prepared PEG solution was added to the bacterial pellet. This bacterial suspension was shaken at 20 ºC for 14 h using a bio-shaker (MBR022UP; Taitek, Saitama, Japan). The prepared PEGylated bacterial hybrid dispersions were centrifuged, resuspended in ATCC 543 media, and washed three times to remove the unbound PEG molecules. The amount of attached PEGs on the bacterial membrane was calculated by weighing and subtracting dried unreacted PEGs in supernatants after each PEGylation with bacteria.

BAM (0.5 mg mL^{-1}; SUNBRIGHT OE040CS, NOF Corporation, Tokyo, Japan) was added in PBS and sonicated for 1 min at 20 ºC. After sonication, Alexa Fluor 488-conjugated bovine serum albumin (Alexa488-BSA) (1 mg mL^{-1}; Thermo Fisher Scientific, Waltham, MA, USA) or anti-mouse programmed death ligand monoclonal antibody (anti-PD-L1) (1 mg mL^{-1}; 10F.9G2 Platinum *in vivo* grade; Leinco Technologies, St. Louis, MO, USA) were added to PBS and incubated at 20 ºC for 2 h to synthesize Alexa488-BSA–BAM or anti-PD-L1–BAM conjugates. Alexa488-BSA–BAM was dialyzed (cut off = 12–14 kDa; Spectra/Por) for 2 days at 4 °C and lyophilized to obtain the solid Alexa488-BSA–BAM. The labeling ratio of BAM to fluorescent BSA was measured by molecular weight analysis using the Kaiser test kit (Sigma-Aldrich, Burlington, MA, USA). RP (5×10^9 CFU mL^{-1}) was centrifuged (2,300 × g, for 5 min at 4 °C) to obtain a pellet, and the prepared Alexa488-BSA–BAM or anti-PD-L1–BAM conjugate solutions were added to the bacterial pellet to obtain Alexa488-BSA–BAM–RP and anti-PD-L1–BAM–RP. This bacterial suspension was incubated at 20 ºC for another 30 min. Shortly thereafter, the prepared bacterial hybrid dispersions were centrifuged, resuspended in ATCC 543 media after discarding the supernatant, and washed once to remove the unreacted biomolecule-functionalized BAM conjugates.

Anchored Alexa488-BSA–BAM conjugates on RP were measured as follows. Briefly, prepared Alexa488-BSA–BAM–RP (5×10^9 CFU mL^{-1}) was incubated at 20 ºC for different time points. Detached Alexa488-BSA–BAM was removed by centrifugation, and the sample was then resuspended in ATCC 543 media. The fluorescence intensities of the Alexa488-BSA–BAM–RP were measured by a fluorescent spectrometer to monitor anchored Alexa488-BSA–BAM conjugates on RP.

The viabilities of the functional bacterial hybrids were measured using a bacterial counter (DUAA01NP-H; PHC, Tokyo, Japan), as well as an active colony assay.

The amount of functional proteins loaded on the bacterial membrane was calculated from the collected supernatant of the washed bacteria after modification with Alexa488-BSA–BAM or anti-PD-L1–BAM using a bicinchoninic acid assay kit (Thermo Fisher Scientific) and a microplate reader, according to the manufacturer's instructions. The loading capacity of Anti-PD-L1 on the bacterial membrane was estimated by flow cytometry (CyFlow Cube 6, Sysmex, Kobe, Japan) by analyzing Alexa488-Anti-PD-L1–BAM–RP and natural RP (5×10^7 cells for each sample).

3.2.7 Polydopamine nanocoating

Polydopamine nanocoating on the bacterial membrane of RP was referred to the previous work.[8] Briefly, to prepare functional RP with dopamine concentrations of 1.25, 2.5, 5, and 10 mg mL^{-1}, 1.25, 2.5, 5, and 10 mg of dopamine hydrochloride (Sigma-Aldrich) was suspended in 1 mL of 10 mM Tris−HCl buffer (pH 8.5) and then added 50 μL of bacterial suspension. After strong stirring at room temperature for 2 h, polydopamine coated-RP was obtained by centrifugation at 4000 g for 20 min, suspended in PBS, and stored at 4 °C for immediate use. The viability of the polydopamine-coated bacterial hybrids was measured using a bacterial counter.

3.2.8 Fluorescence microscopy imaging

Various bacterial samples (RP concentration = 5×10^9 CFU mL^{-1}) were plated (10 μL) on a glass slide (AGC Techno Glass, Shizuoka, Japan) with a coverslip and then observed using a fluorescence microscopy system (IX73; Olympus, Tokyo, Japan) and cellSens V3.1 software (Olympus) equipped with a mirror unit (IRDYE800-33LP-A-U01; Semrock, Lake Forest, IL, USA or IX3-FGFPXL, Olympus) and a lens (× 100 magnification, aperture 0.95; UPLSAPO40X,

Olympus) at 20 °C. To confirm intracellular uptake of BAM–RP and RP, Colon-26 cells (5.0×10^5 cells $well^{-1}$) were seeded in poly-L-lysine coated glass bottom dishes and allowed to adhere overnight. Cells were then incubated with 1×10^9 CFU of BAM–RP or 1×10^9 CFU of RP for 4 h at 4 °C or 37 °C in a fridge or a humidified incubator containing 5% CO_2. After washing thoroughly with fresh PBS solution, Colon-26 cells were observed in the same way to evaluate the macrophage phagocytosis behavior.

To observe the macrophage phagocytosis behavior, RAW264.7 cells (5.0×10^5 cells $well^{-1}$) were seeded in a poly-L-lysine-coated glass bottom dish (Iwaki Glass, Tokyo, Japan) and allowed to adhere overnight. Cells were then exposed to 2.4×10^9 CFU/mL of PEGylated RP for 4 h at 37 °C in a humidified chamber containing 5% CO_2. After washing thoroughly with fresh medium, RAW264.7 cells were observed using a fluorescence microscopy system (IX73) equipped with a mirror unit (IRDYE800-33LP-A-U01; Semrock, Lake Forest, IL, USA) and a lens (× 60 magnification, aperture 1.35; UPLSAPO60X, Olympus) at 20 ºC.

To evaluate the green-fluorescent property of Alexa488-BSA–BAM on RP bacterial membrane, the prepared Alexa488-BSA–BAM–RP was observed using a fluorescence microscopy system (IX73) equipped with a mirror unit (IX3-FGFPXL, Olympus) and a lens (× 60 magnification, aperture 1.35; UPLSAPO60X, Olympus) at 20 ºC. Bacterial concentration was 5.0×10^9 CFU mL^{-1}.

3.2.9 Nanostructural characterization

Negative staining was used to observe the morphology and structure of Alexa488-BSA–BAM–RP and RP using a high-resolution transmission electron microscope (TEM, H-7600; Hitachi, Tokyo, Japan) at an acceleration voltage of 100 kV. TEM observations were performed at the Hanaichi Ultrastructure Research Institute Co., Ltd. (Aichi, Japan).

3.2.10 Laser-induced cytotoxicity

Colon26 or WI38 cells at a density of 7×10^3 cells well^{-1} were seeded in 96-well plates. After overnight incubation, RP (100 μL; 5×10^9 CFU mL^{-1}), anti-PD-L1–BAM–RP (100 μL; 5×10^9 CFU mL^{-1}), or PBS (100 μL) were added and irradiated with an 808 nm laser at a power of 1.2 W (~6.1 W cm^{-2}) and 0.6 W (~3.1 W cm^{-2}) for 0, 1, and 3 min in a 37 °C incubator. The sample wells were washed thoroughly, and the cells were resuspended in fresh media. The plates were incubated for another 24 h, and cell viability was determined using the CCK-8 kit. A control treatment without laser irradiation was also performed.

3.2.11 *In vivo* phototherapy

Animal experiments were carried out in accordance with the protocols approved by the Institutional Animal Care and Use Committee of JAIST (No. 01-002). Female BALB/cCrSlc mice (n = 40; 4 weeks old; average weight = 15 g) were purchased from Japan SLC (Hamamatsu, Japan). Colon26 cells were injected in mice, along with a Matrigel (Dow Corning, Corning, NY, USA) mixture (v/v = 1:1; 100 μL) containing 1×10^6 cells into the right flank of the mice. Once the tumor volume reached 100 mm^3, approximately after 10 days, the mice were intratumorally injected with 100 μL of RP (2.5×10^9 CFU mL^{-1} or 5×10^9 CFU mL^{-1}), BAM–RP (5×10^9 CFU mL^{-1}), anti-PD-L1–BAM–RP (2.5×10^9 CFU mL^{-1} or 5×10^9 CFU mL^{-1}), PBS, or PBS containing anti-PD-L1 (2.5 mg kg body weight^{-1}). The tumors were irradiated using an 808 nm laser at 0.7 W (713 mW, 3.6 W cm^{-2}) 24 h after injection for 3 min every other day (two times in total). A clamp was used to aim the laser beam at the center of the solid tumor. Thermographic measurements were obtained during irradiation using IR thermography (i7; FLIR, Nashua, NH, USA). Tumor growth rate and overall body weight were monitored every other day. Furthermore, the tumor volume was calculated using the equation: $V = L \times W^2/2$, where L and W denote the

length and width of the tumor, respectively. The mice were euthanized when the tumor volume reached more than 2,000 mm^3 according to the guidelines of the Institutional Animal Care and Use Committee of JAIST.

3.2.12 *In vivo* fluorescent bio-imaging

Colon26 tumor-bearing mice (female; 7 weeks; n = 3; average weight = 18 g; average tumor size = 400 mm^3; BALB/cCrSIc; Japan SLC) were intravenously injected with 100 μL of RP (5×10^8 CFU), anti-PD-L1–BAM–RP (5×10^8 CFU), or PBS to investigate the chronological changes in FL intensity caused by the tumor-targeting effect of the bacteria. Fluorescence intensity was observed from day 0 to day 8 of post-injection, and the mice were euthanized on day 8 to extract major organs, including the heart, liver, spleen, lung, kidney, and tumor. The treated mice were imaged using an *in vivo* fluorescence imaging system (VISQUE™ InVivo Smart-LF, Vieworks, Anyang, Republic of Korea) with a 3 sec exposure time and an ICG filter (Ex, 740–790 nm; Em, 810–860 nm). The fluorescence images were acquired and analyzed using CleVue™ software (Vieworks).

3.2.13 Biodistribution of bacteria in tumor model

The Colon26 tumor-bearing mice (female, 7 weeks; n = 4; average weight = 18 g; average tumor size ~ 400 mm^3; BALB/cCrSIc; Japan SLC) were intravenously injected in the tail vein with culture medium (100 μL) containing anti-PD-L1–BAM–RP (5×10^9 CFU mL^{-1}) or PBS (100 μL). After 144 h, the organs and tumors were carefully excised and weighed. After homogenizing thoroughly with a homogenizer pestle in 1 mL of PBS solution at 4 ºC, the mixture was shaken for 20 min at a speed of 380 rpm/min at 15 ºC. The supernatant was diluted 0, 10, 100, and 1000 times

with PBS, and then the sample (50 μL) from 1000 times dilution was inoculated onto an agar plate. After anaerobically incubated for 6 days, the formed bacterial colonies were imaged.

3.2.14 Immunohistochemistry (IHC) staining of tumor tissues

To investigate the IHC of tumor tissues, Colon26 tumor-bearing mice were injected with RP (100 μL, 5×10^8 CFU), anti-PD-L1–BAM–RP (100 μL, 5×10^8 CFU), or PBS (100 μL) intratumorally and irradiated with an 808 nm laser 24 h after injection. The control groups were not irradiated with a laser. The mice were euthanized after another 24 h, and tumor tissues from the treatment and control groups were harvested for IHC staining. The IHC analyses were performed by Biopathology Institute Co., Ltd. (Oita, Japan) using standard protocols. Briefly, the primary tumors were surgically removed, fixed in 10% formalin, processed for paraffin embedding, and cut into 3-4 μm-thick sections. After incubation with primary antibodies (listed in Table 3.2), the sections were stained with H&E and examined using light microscopy. The areas showing positive staining in tumor tissues were analyzed using a light microscopy system (BZ-X800, Keyence, Osaka, Japan) and hybrid cell count and microcell count software (Keyence).

3.2.15 Blood tests

The complete blood count (CBC) and biochemical parameters were investigated by Japan SLC and Oriental Yeast Co., Ltd (Tokyo, Japan). The tail vein of BALB/cCrSlc mice (female, 10 weeks; n = 10; average weight = 21 g; Japan SLC) was injected with PBS containing anti-PD-L1–BAM–RP (200 μL, 1.0×10^6 CFU) or PBS alone (200 μL). After 30 days, blood samples were collected from the inferior vena cava of these mice.

3.2.16 Statistical analysis

All experiments were performed in triplicates and repeated three or more times. Quantitative values are expressed as means ± standard error of the mean (SEM) of at least three independent experiments. Statistical differences were identified using Student's two-sided t-test and one-way or two-way analysis of variance (ANOVA).

3.3 RESULTS AND DISCUSSION

3.3.1 Screening of optimal PPSB for phototherapy

By investigating safety (cytotoxicity), NIR fluorescence, and photothermal conversion, the most appropriate bacterium for advanced cancer phototheranostics was screened out from various commercially available PPSBs, such as *Pararhodospirillum oryzae* (NBRC107573), *Pararhodospirillum sulfurexigens* (NBRC104433), *Rhodomicrobium udaipurense* (NBRC109057), *Rhodomicrobium vannielii* (NBRC100050), *Rhodovulum sulfidophilum* (ATCC35886), *Afifella marina* (NBRC100434), *Rhodobacter sphaeroides* (NBRC12203), *Rhodobacter blasticus* (NBRC16437), *Rhodocista centenaria* (NBRC16667), and *Rhodobacter capsulatus* (NBRC16435), as well as RP (NBRC16661), which we used in our previous study[24] (Figures 3.1, 3.2, 3.3 and 3.4). A visible, clinically versatile, and relatively cheap 808 nm NIR laser was used for photothermal conversion tests. The human normal diploid fibroblast cell line MCR5 was utilized for safety experiments. Cell viability was tested after incubation with bacteria for 4 h to avoid misreading the detections caused by the formations of sticky bacterial attachment and biofilm on treated cells after incubation for more than 4 h. RP displayed excellent physicochemical and physiological properties with high biocompatibility. In fact, RP exhibited characteristic optical absorbance in the NIR region derived from intercellular BChl, superior NIR

fluorescence emission, powerful photo-exothermicity, and low cytotoxicity. The strong NIR fluorescence and photothermal conversion of RP can be expressed as BChl via sophisticated energy transformations with higher efficiencies than other PPSBs.[24] Thus, we applied RP as the optimal bacterium, or "platform," for regulating optical and immunological functions and anticancer efficacies through further chemical modification with PEG derivatives and therapeutic functional biomolecules.

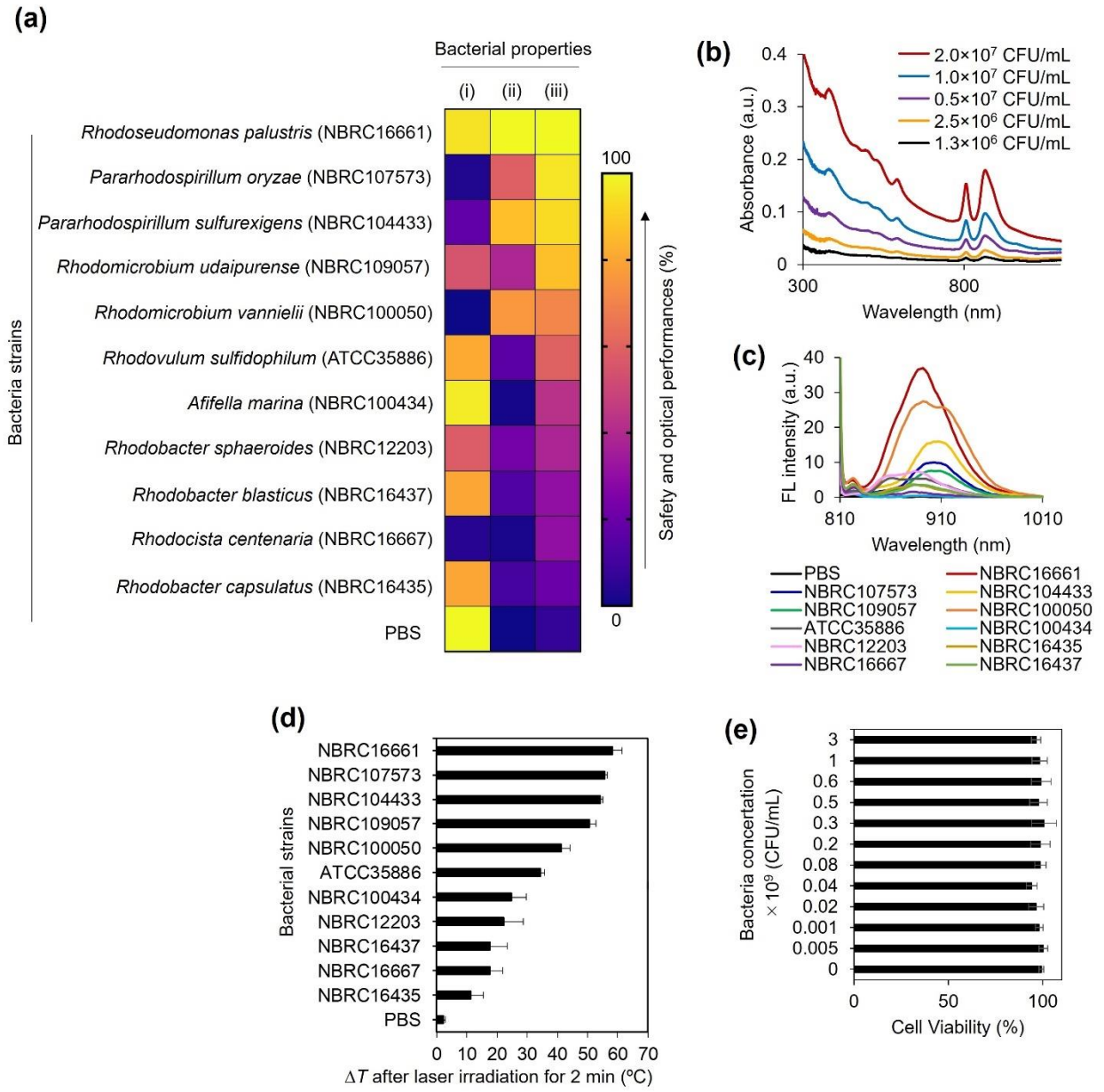

Figure 3.1 Screening for the highest-performing PPSB. (a) Heat map of (i) cytotoxicity, (ii) fluorescence, and (iii) photothermal conversion of various PPSBs. (b) UV–vis–NIR absorbance of RP dispersions at different concentrations. (c) Fluorescence emission spectra of various PPSB dispersions excited at 800 nm. (d) Photothermal conversion of various PPSBs after 808-nm laser irradiation for 2 min. Data are presented as means ± standard errors of the mean (SEM); n = 3 independent experiments. (e) RP cytotoxicity. MRC5 cell viability was tested after 4 h of treatment with RP at different bacterial concentrations. Data are presented as means ± SEM; n = 5 independent experiments. Multiplicity of infections (MOIs) of each bacterial concentration (0.05×10^9, 0.01×10^9, 0.02×10^9, 0.04×10^9, 0.08×10^9, 0.2×109, 0.3×10^9, 0.6×10^9, 1×10^9, and 3×10^9 CFU/mL) are 214, 428, 856, 1712, 3424, 6848, 13696, 27392, 54784, and 109568.

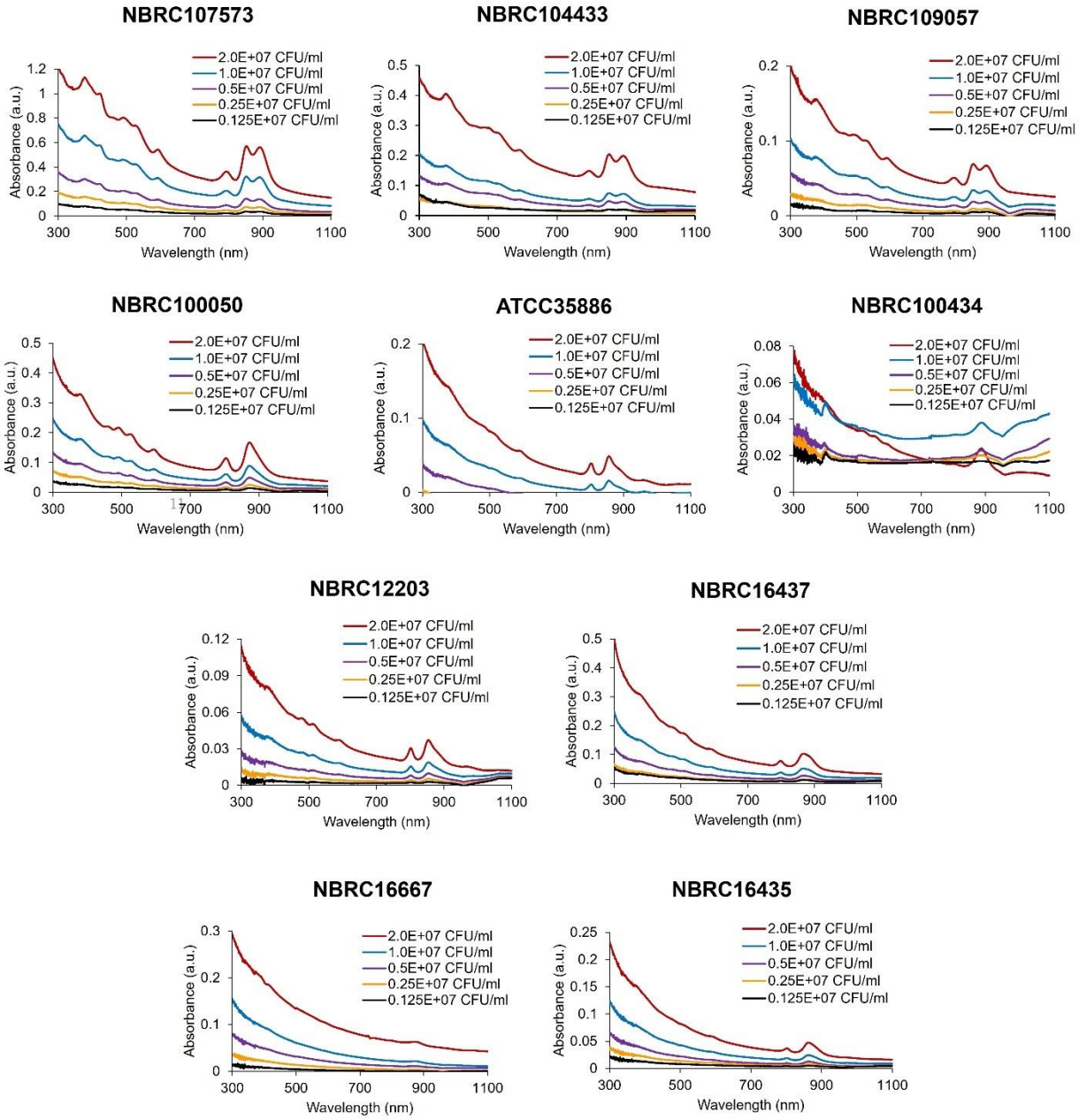

Figure 3.2 UV–vis–NIR absorbance of various purple photosynthetic bacteria (PPSBs) at different concentrations.

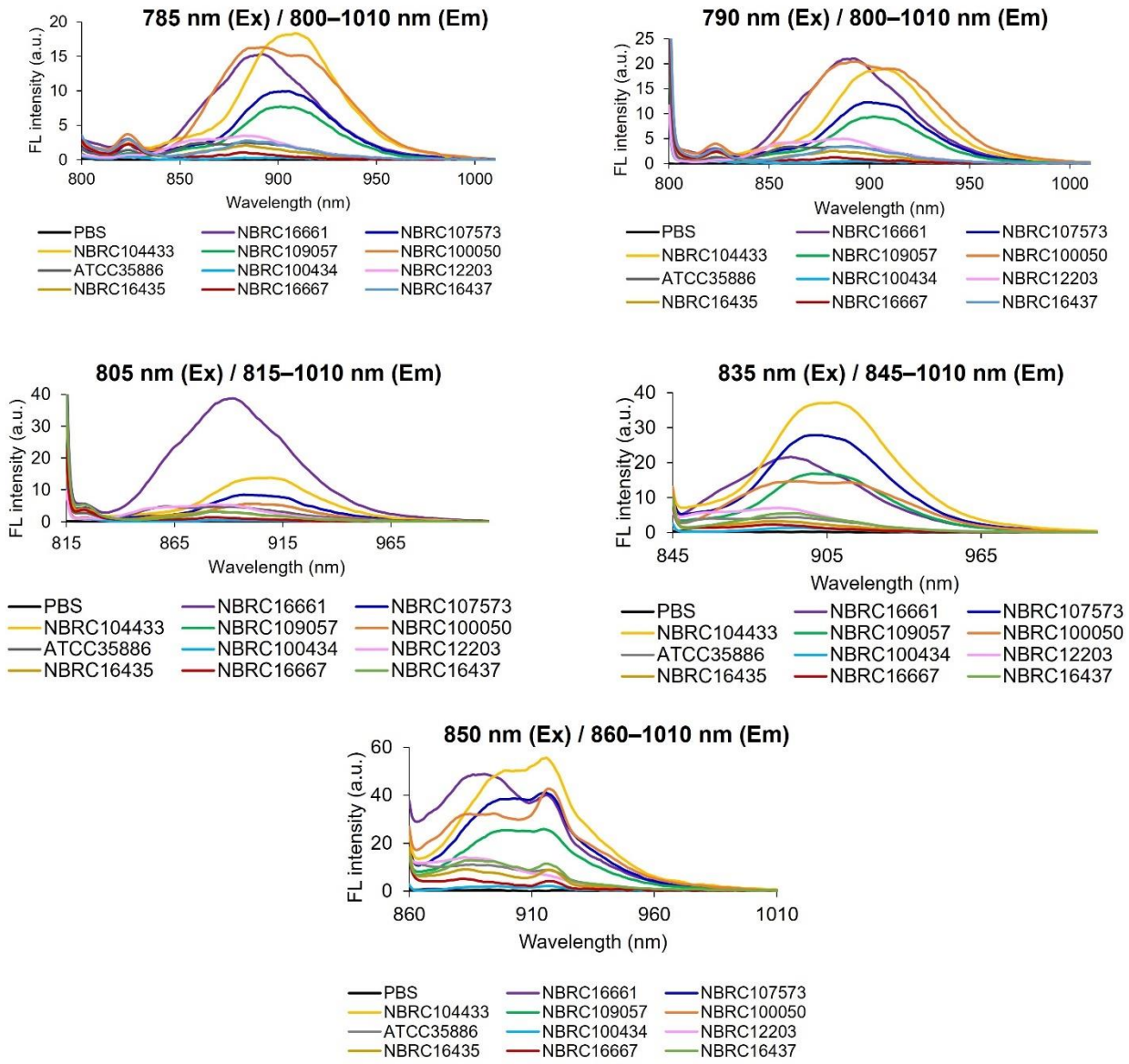

Figure 3.3 Fluorescent emission spectra of various PPSBs excited at different excitation wavelengths (785, 790, 805, 835, and 850 nm).

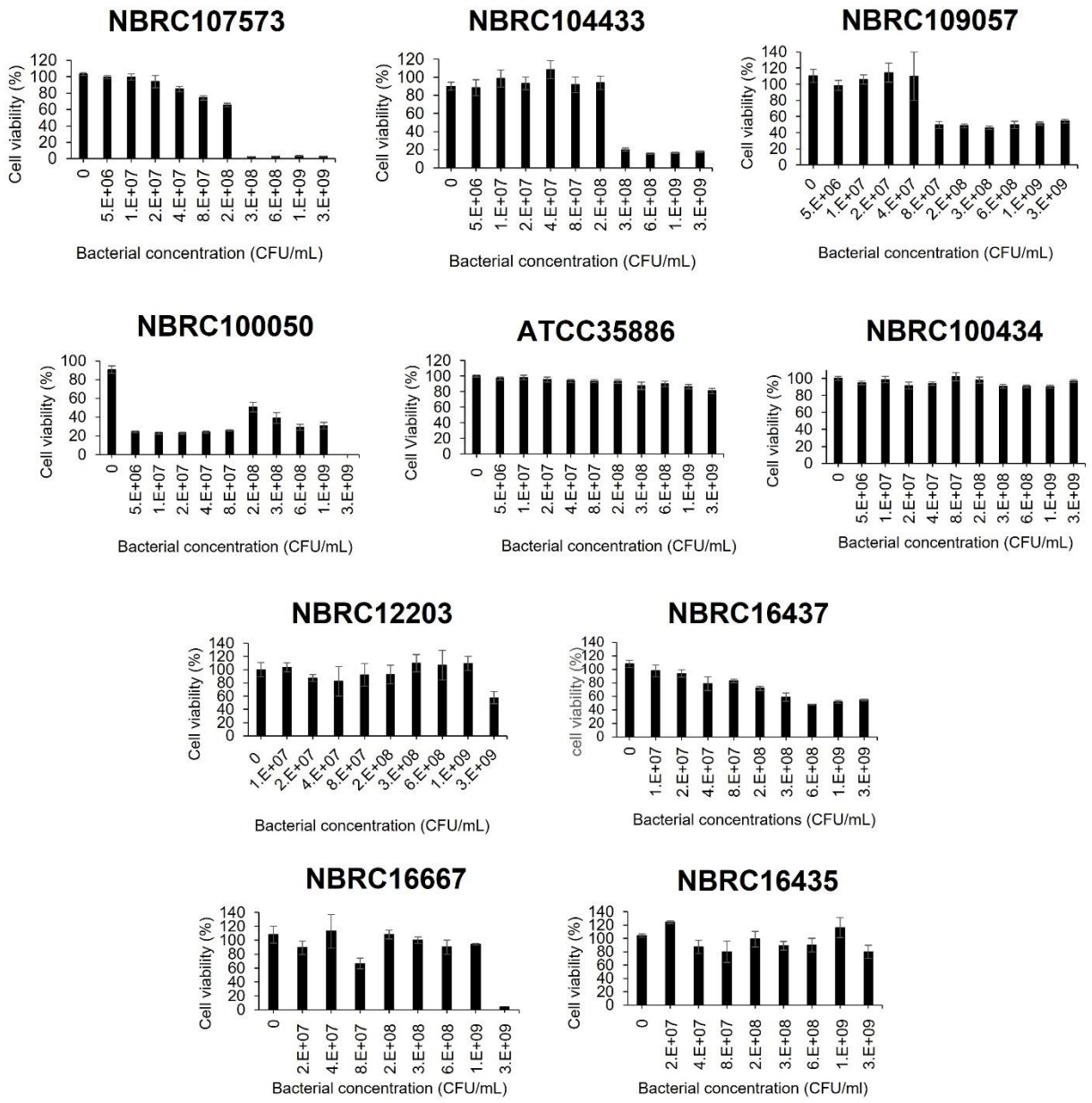

Figure 3.4 Cytotoxicity of various PPSBs. MRC5 cell viability was tested after 4 h of treatment with various PPSBs at different bacterial concentrations. Data are presented as means ± SEM; n = 5 independent experiments. Multiplicity of infections (MOIs) of each bacterial concentration (5×10^6, 1×10^7, 2×10^7, 4×10^7, 8×10^7, 2×10^8, 3×10^8, 6×10^8, 1×10^9, and 3×10^9 CFU/mL) are 214, 428, 857, 1714, 3428, 8570, 12855, 21425, and 64275.

3.3.2 Synthesis of chemically engineered RP hybrids

PEG is a unique hydrophilic and electrical neutralized polymeric material. PEG coating is a crucial factor improving the biophysical and chemical properties of various materials and is widely studied for biomedical applications. Thus, five commercially available functional PEG derivatives, including α-succinimidyloxysuccinyl-ω-methoxy, polyoxyethylene (50CS; PEG chain molecular weight (Mw): 5,000), 4-arm PEG succinimidyl glutarate ester, 20K (4-arm; PEG chain Mw: 20,000), 8-arm PEG succinimidyl carboxy methyl ester, 40K (8-arm; PEG chain Mw: 40,000), Cremophor® EL (CRE; PEG chain Mw: 2,500), and biocompatible anchor for membrane (BAM; PEG chain Mw: 4,000), were utilized for chemical modification of the RP bacterial membrane (Figure 3.5a). RP is a gram-negative bacterium with a double layer of outer and plasma membranes.[27] A gram-negative cell wall typically consists of two or three interconnected peptidoglycan layers surrounded by an outer membrane composed of lipopolysaccharides (LPS) and membrane proteins.[28] Thus, 4-arm, 8-arm, and 50CS were directly conjugated to the primary amines of a bacterial membrane protein through their N-hydroxysuccinimide (NHS) groups via covalent bonding (Figure 3.5b).[29–31] Meanwhile, the three branched alkyl chains of CRE and the oleyl acid chain of BAM were simultaneously inserted into the bacterial lipid layer, resulting in the decollation of PEG brushes onto the bacterial membrane via non-covalent binding (Figure 3.5b).[23,32,33] These PEGylations of the bacterial membrane could be performed through two simple steps of incubation and washing, without complicated organic synthesis (mentioned in Experimental Procedures).

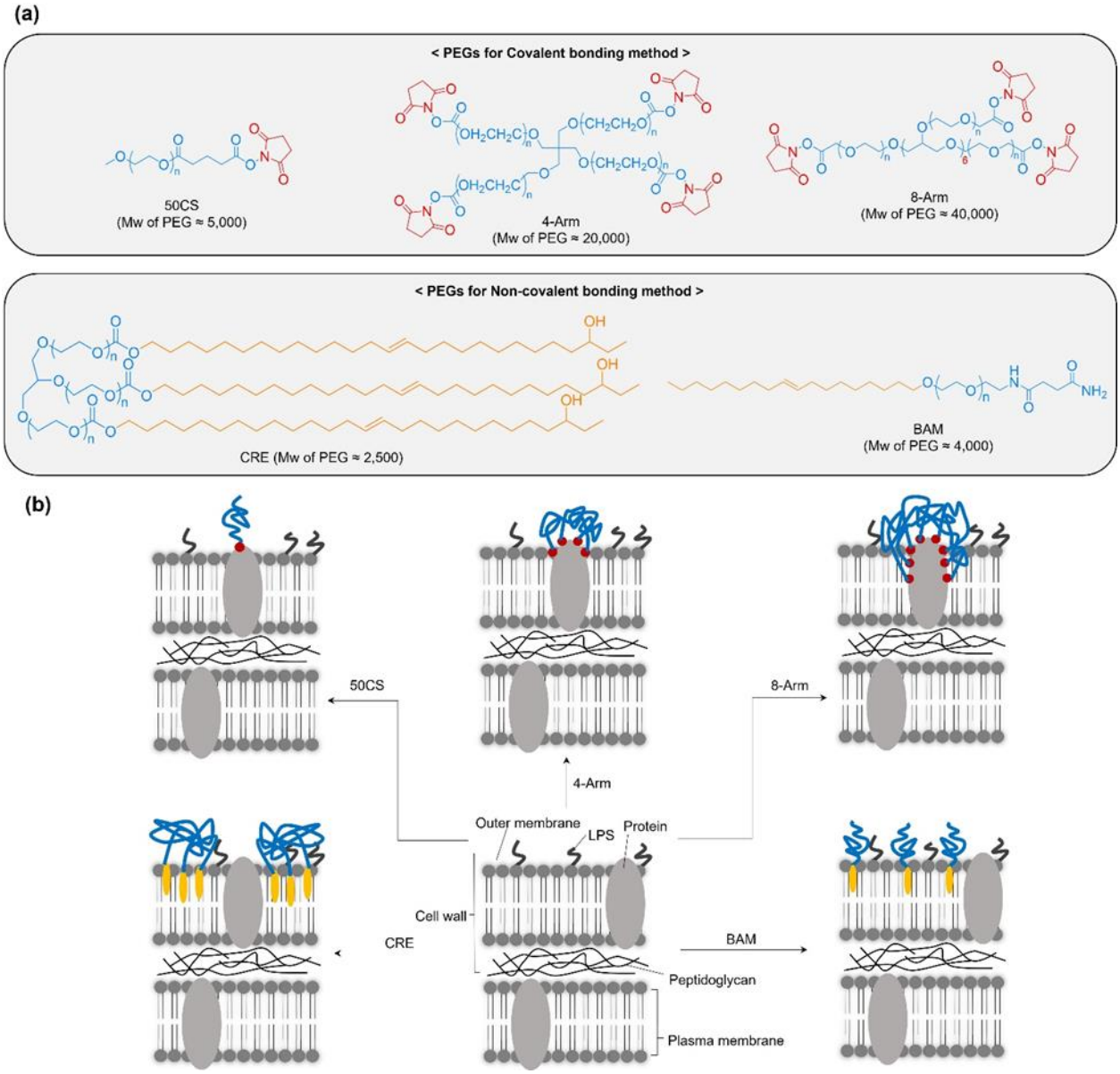

Figure 3.5 PEGylated RP preparation. (a) Chemical structures of various PEG derivatives. (b) Schematic illustration of PEGylations of the RP bacterial membrane through covalent and non-covalent bonding.

Next, the PEGylation effects on the optical and physiological traits of RP were investigated (Figure 3.6). There were no negative effects on RP optical properties and bacterial viability in all types of PEGylation (Figure 3.6a–3.6d). However, bacterial colonization was inhibited by modifications with 4-arm and 8-arm, while PEGylation with 50CS, CRE, and BAM did not influence colony formation (Figure 3.6e). Covalent multi-point connections on membrane proteins with 4-arm or 8-

arm molecules may severely hinder cell division. Besides, polydopamine nanocoating on bacterial membrane, which is one of the popular surface modification methods against bacteria to enhance their photothermal anticancer efficacy,[8] adversely affected the bacterial viability and proliferation in a concentration of dopamine dependent manner even though photothermal conversion property of RP was improved (Figure 3.7).

Although many examples of nanofunctionalization of bacteria show this is not always the case, potential nanotoxicity might be concerned for designing of effective nanoparticles-integrated bacterial complexes. All PEGylated RP hybrids did not exhibit any cytotoxicity to various cell lines, such as MRC5, mouse rectal carcinoma (Colon26), and phagocytic mouse macrophage (RAW264.7) because of the innately high biocompatibility of PEGs[31] and RP[24] (Figures 3.6f and 3.8).

PEGs are frequently used as a protective coating on materials to reduce immunogenicity.[34–36] We thus compared the cellular internalization of the PEGylated RP hybrids with different surface functionalization (Figure 3.6g). Interestingly, most of the 8-arm- and BAM-functionalized RPs (8-arm–RP and BAM–RP) were not phagocytized by RAW264.7, probably because of the aforementioned immune evasion effect of PEG protection. The 4-arm, 50CS-, and CRE-modified bacterial hybrids (4-arm–RP, 50CS–RP, and CRE–RP) and natural RP were actively phagocytized by RAW264.7 cells. As a result, strong NIR fluorescence (pink dots) from RP was observed within the cells. BAM was used as an effective RP modification agent for further experiments in this research because of its encouraging safety and immunological blocking effect against macrophages for cancer treatment. Meanwhile, 50CS (ca. 62 μg; ca. 310 mol), 4-Arm (ca. 49 μg; ca. 980 mol), 8-Arm (ca. 51 μg; 2040 mol), CRE (ca. 225 μg; 563 mol), and BAM (ca. 313 μg; 1252 mol) were modified on RP (3×10^9 CFU mL^{-1}), respectively. These results indicate that both

the PEG molecular weight and the surface PEG density are important for effective immune evasion of functional bacteria.

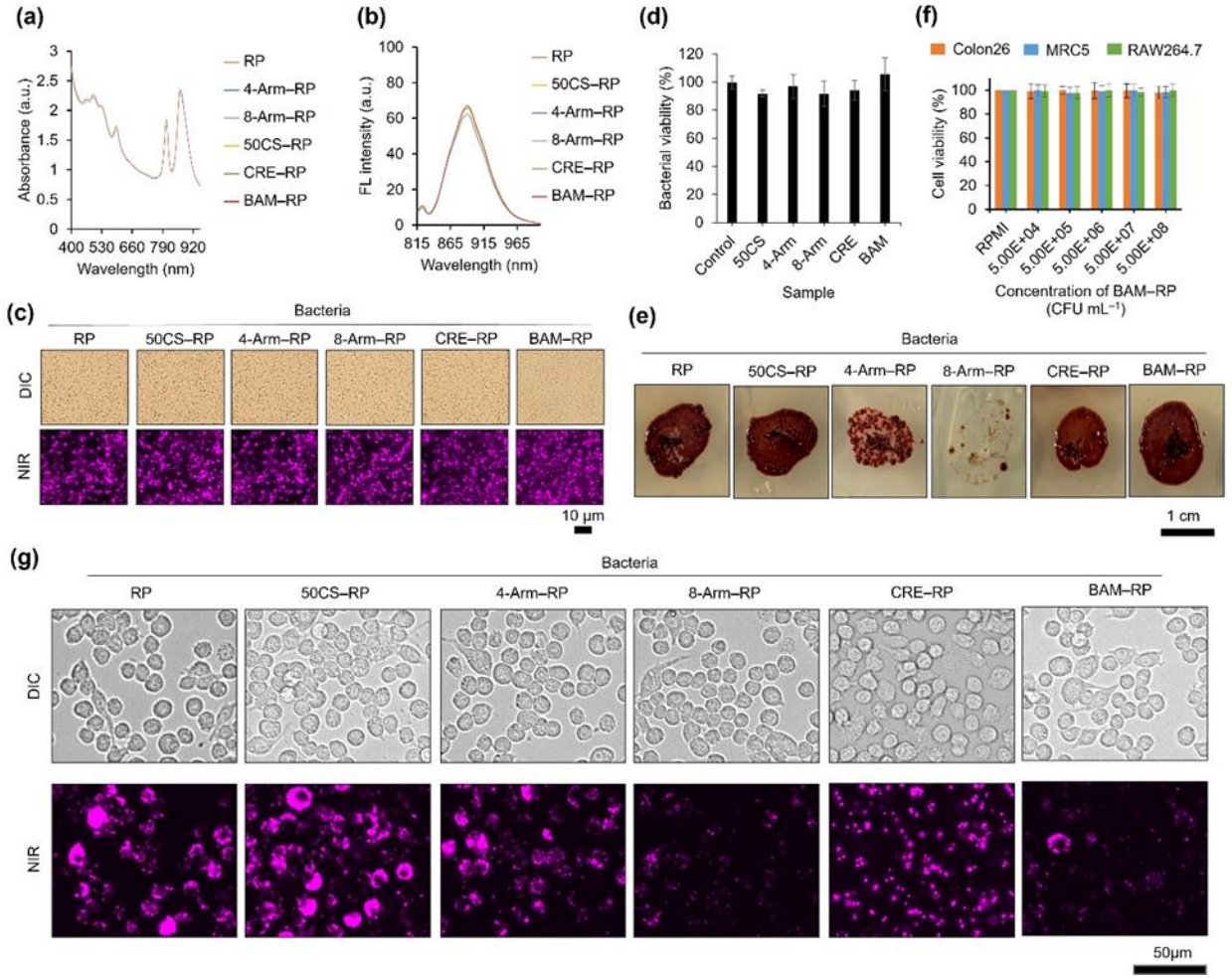

Figure 3.6 Characterization of various PEGylated RPs. (a) UV–vis–NIR absorbance of various PEGylated and conventional RP dispersions. Bacterial concentration was 2.4 × 10^8 CFU mL^{-1}. (b) Fluorescence emission spectra of various PEGylated and conventional RP dispersions excited at 805 nm. Bacterial concentration was 2.4 × 10^8 CFU mL^{-1}. (c) In vitro NIR fluorescence imaging of various PEGylated and conventional RPs. Bacterial centration was 5 × 10^8 CFU mL^{-1}. Pink dots represent bacteria. (d) Bacterial viability after various PEGylations for 24 h. Data are presented as means ± SEM; n = 3 independent experiments. (e) Bacterial colonies after various PEGylations. (f) BAM–RP cytotoxicity. Colon26, MRC5, and RAW264.7 cell viabilities were tested after 4 h of BAM–RP treatment at different bacterial concentrations. Data are presented as means ± SEM; n = 5 independent experiments. Multiplicity of infections (MOIs) of each bacterial concentration (5×10^4, 5×10^5, 5×10^6, 5×10^7, and 5×10^8 CFU/mL) are 2, 21, 214, 2142, and 21428. (g) NIR fluorescence microscopic images of RAW264.7 mouse monocyte macrophage cells after incubation with various PEGylated RPs (2.4 × 109 CFU mL^{-1}) for 4 h. Pink dots show bacterial uptake into cells via macrophage phagocytosis.

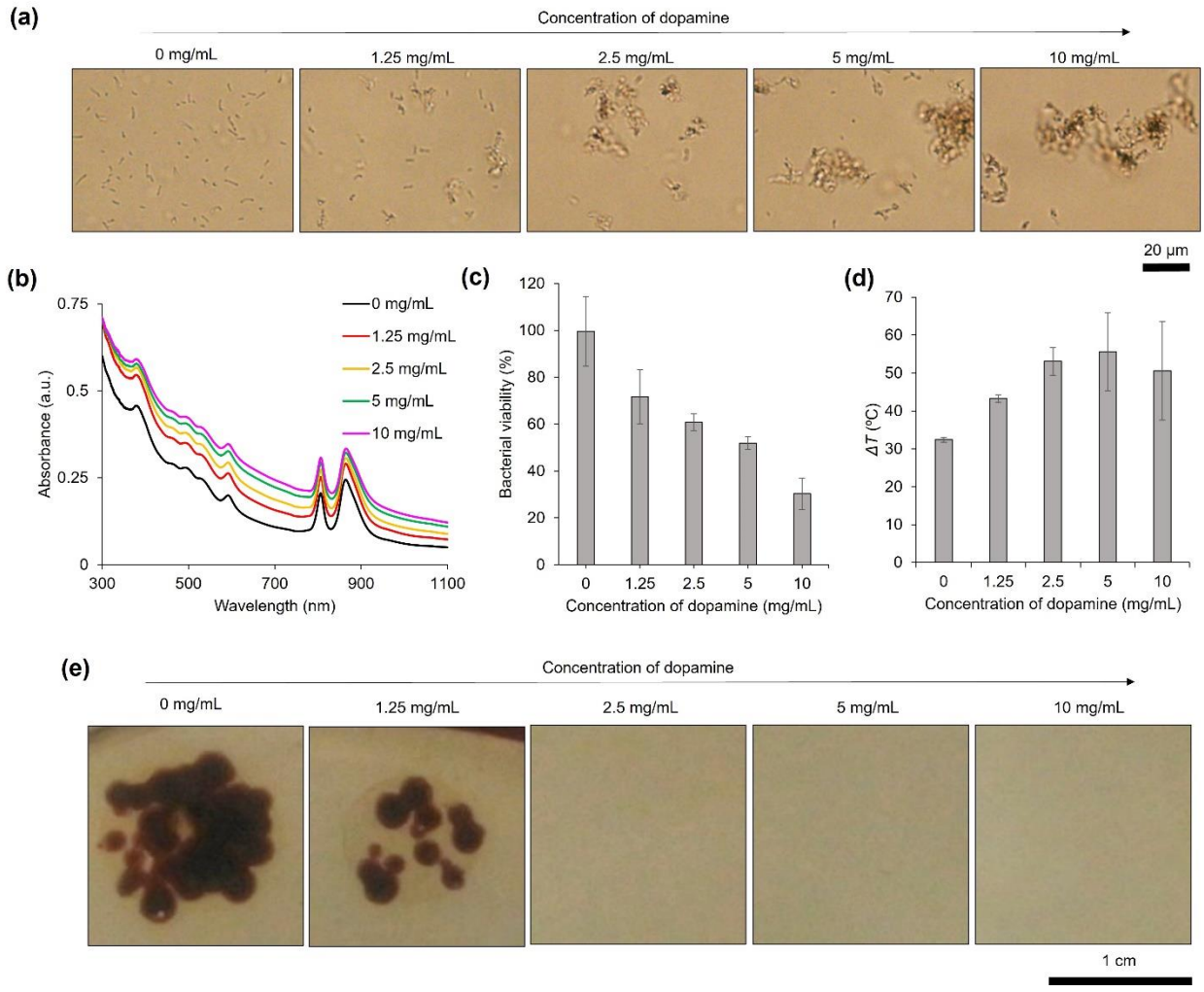

Figure 3.7 Influence of polydopamine nanocoating on biological activities of RP. (a) In vitro differential interference contrast (DIC) imaging of RP after polydopamine nanocoating. Bacterial concentration was 5.0×10^8 CFU mL^{-1}. (b) UV–vis–NIR absorbance of polydopamine-functionalized RP dispersions. Bacterial concentration was 2.5×10^7 CFU mL^{-1}. (c) Bacterial viability after polydopamine nanocoating. Data are presented as means ± SEM; n = 3 independent experiments. (d) Temperature difference (ΔT) of the various sample solutions after irradiation with 808 nm laser at 0.6 W (~3.1 W cm^{-2}) for 1 min. RP concentration was approximately 5.0×10^8 CFU well–1. Data are presented as means ± SEM; n = 3 independent experiments. (e) Bacterial colonies after polydopamine nanocoating.

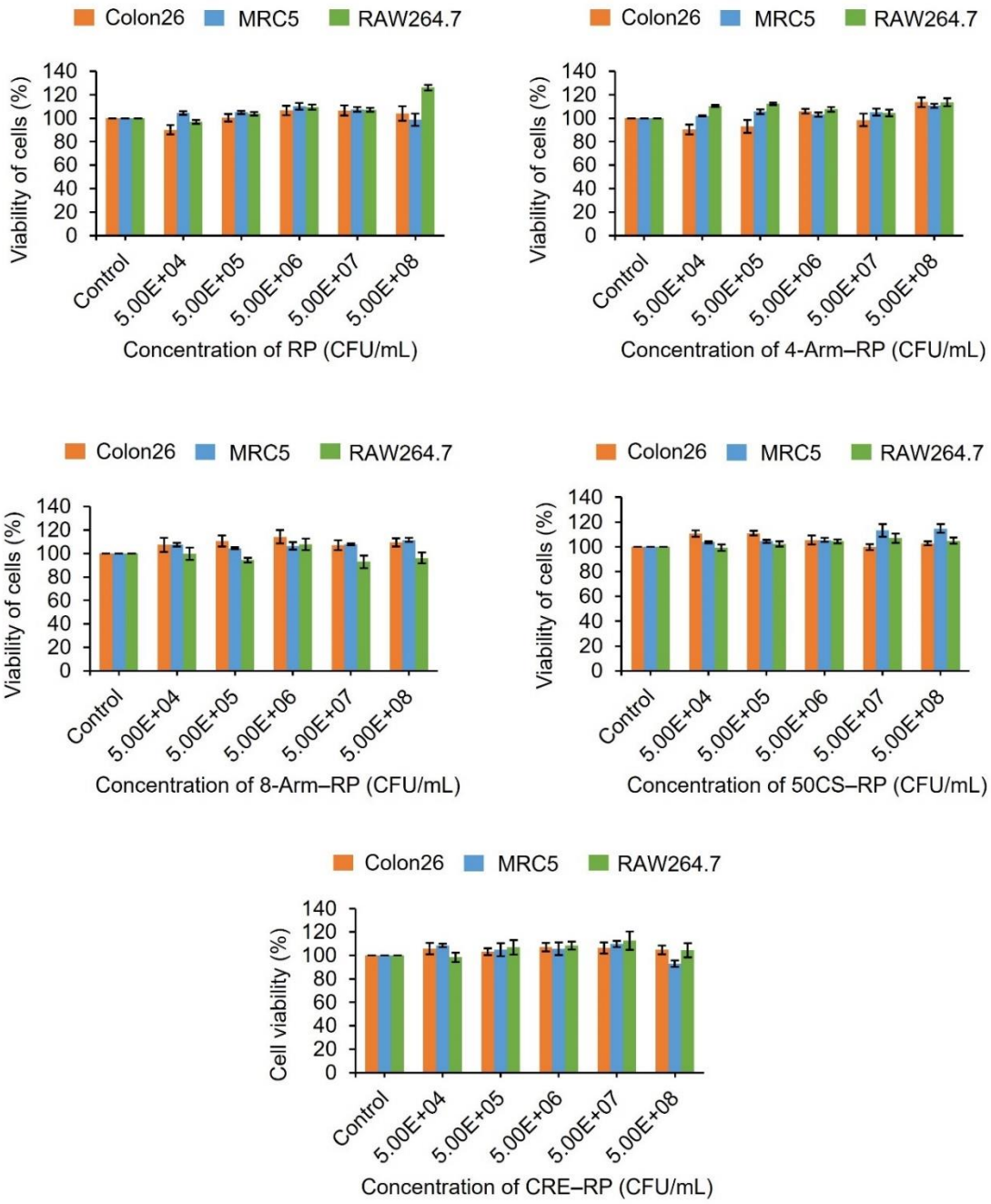

Figure 3.8 Cytotoxicity of various RP conjugates. Colon26, MRC5, and RAW264.7 cell viabilities were tested after 4 h of treatment with various RP conjugates at different bacterial concentrations. Data are presented as means ± SEM; n = 5 independent experiments. Multiplicity of infections (MOIs) of each bacterial concentration (5×10^4, 5×10^5, 5×10^6, 5×10^7, and 5×10^8 CFU/mL) are 2, 21, 214, 2142, and 21428.

The intracellular distribution of BAM–RP in Colon-26 cells was investigated by fluorescence microscopy (Figure 3.9). Intracellular BAM–RP and RP uptake in cells were observed after incubation for 4 h at 4 °C or 37 °C. NIR FL of BAM–RP and RP (pink-colored dots) exhibited their uniform distribution in the cell cytoplasm at 37 °C for 4 h. The FL intensity of BAM–RP is somewhat weaker than that of RP presumably due to the PEGylation. Besides, NIR FL of both BAM–RP and RP were not so strong after incubating cells with BAM–RP and RP at 4 °C for 4 h, suggesting that the bacterial internalization into cells was energy dominant.[37] Herein, we consider that endocytosis and motility are important factors for potential intracellular migrations of PEGylated bacteria.

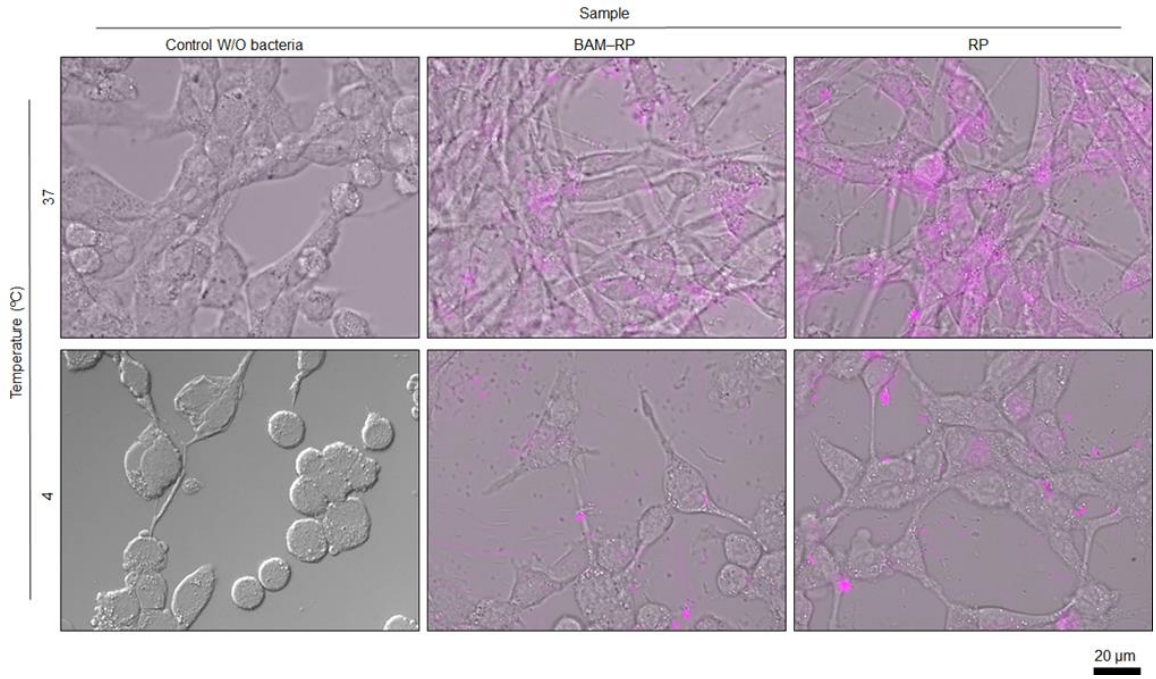

Figure 3.9 FL images of live Colon-26 cells after treatment with BAM–RP and RP for 4 h at 4 °C or 37 °C. The pink FL is from bacteria.

Many researchers have reported rapid and easy BAM anchoring to cell membranes without cytotoxicity.[32,33] In fact, BAM coating did not influence the viability of RP at least for 1 week (Figure 3.10).

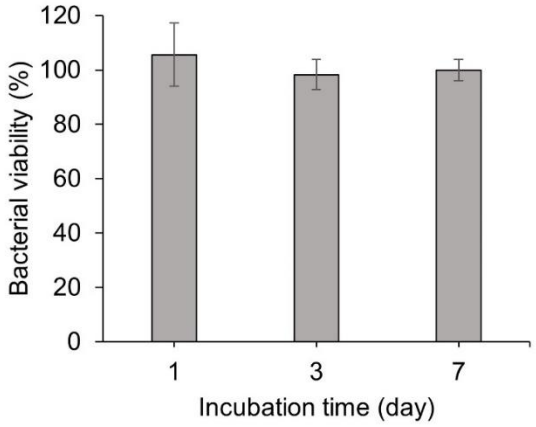

Figure 3.10 Long term safety of BAM coating on RP. The samples in 543 ATCC Rhodopseudomonas medium were kept at 4 ºC before the bacterial viability. Data are presented as means ± SEM; n = 3 independent experiments. The viability of the BAM-coated RP was measured using a bacterial counter.

More importantly, functional molecules, such as Alexa Fluor® 488-conjugated bovine serum albumin (Alexa488-BSA), could be modified through its primary amines to the NHS group at the end of the PEG chain of BAM (Figure 3.11a). The oleyl acid chain of BAM was inserted into the bacterial lipid layer, thereby simultaneously anchoring Alexa488-BSA to the cell membrane through simple incubation and washing processes. The labeling ratio of BAM to fluorescent BSA was determined to be 2 ± 1 by molecular weight analysis using the Kaiser test.[38] Transmission electron microscopy (TEM) indicated that an Alexa488-BSA–BAM nanolayer (ca. 15–20 nm thickness) obviously formed on the RP bacterial surface (Figure 3.11b). Fluorescence microscopic analysis showed that bacteria became fluorescent when they were incubated with the Alexa488-BSA–BAM conjugate (Figure 3.11c). Meanwhile, no nanolayer formation or fluorescence were observed in RP without Alexa488-BSA–BAM (Figures 3.12 and 3.13).

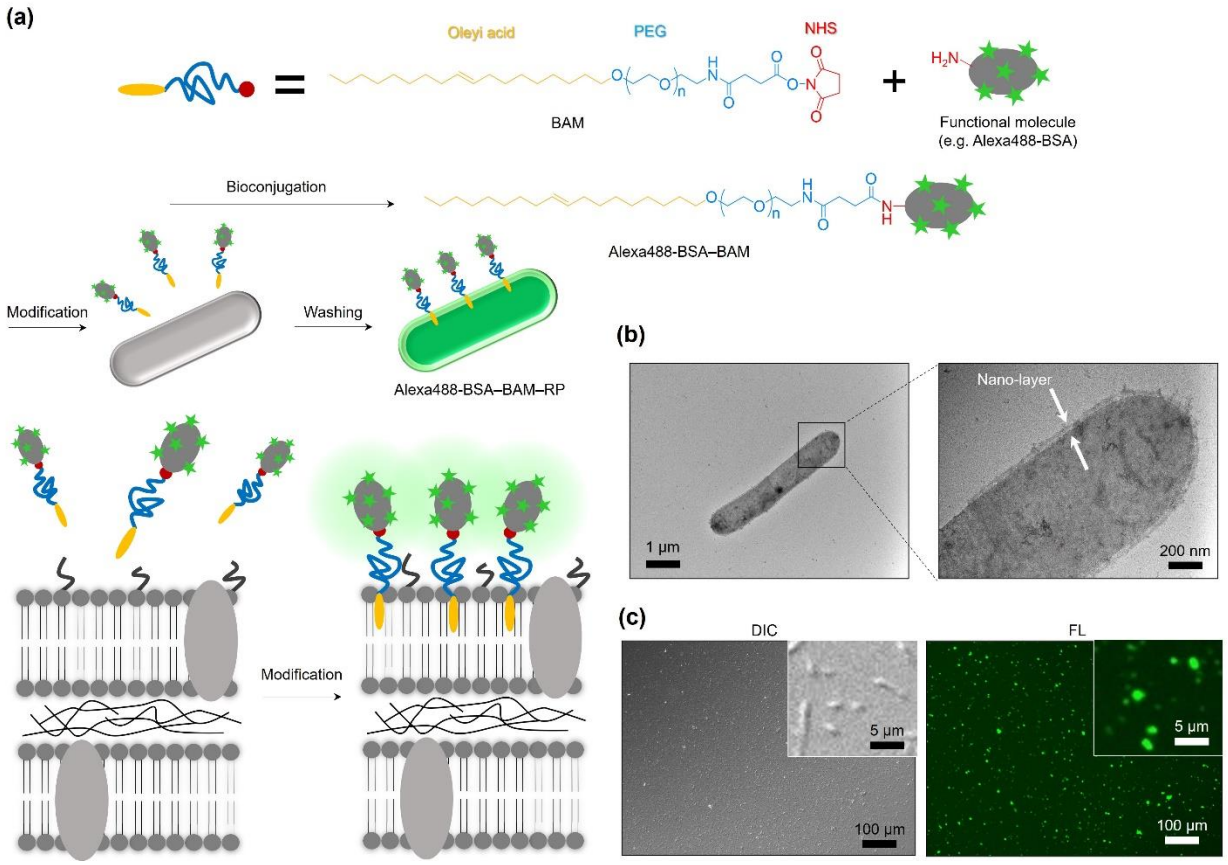

Figure 3.11 Synthesis of functional molecules–BAM-modified RP. (a) Schematic illustration of Alexa488-BSA–BAM–RP preparation. (b) TEM images of Alexa488-BSA–BAM–RP. The right image represents a higher magnification of the boxed area. (c) In vitro differential interference contrast (DIC) (left) and NIR fluorescence (right) imaging of Alexa488-BSA–BAM–RP. Bacterial concentration was 5.0 × 109 CFU mL−1. The upper right images represent higher magnification for each DIC and NIR fluorescence picture.

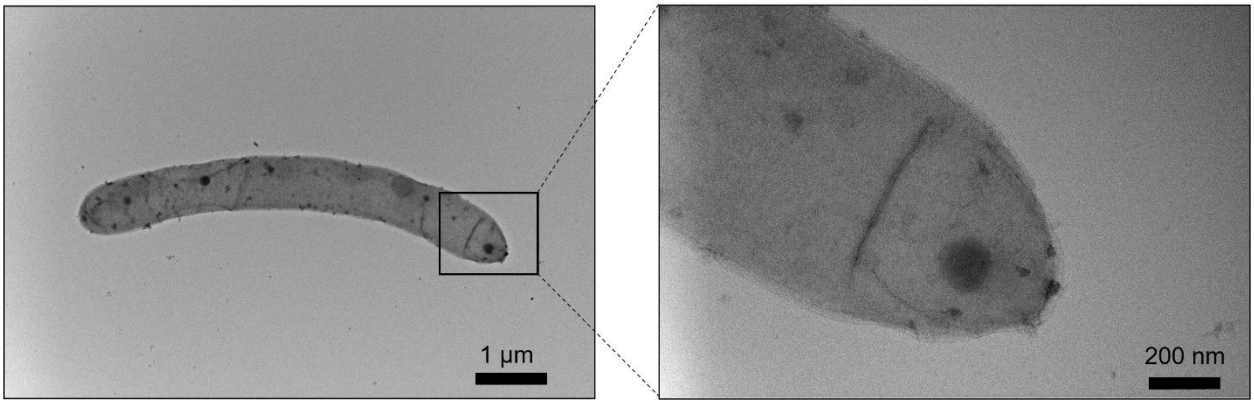

Figure 3.12 TEM images of control RP without Alexa488-BSA–BAM conjugates.

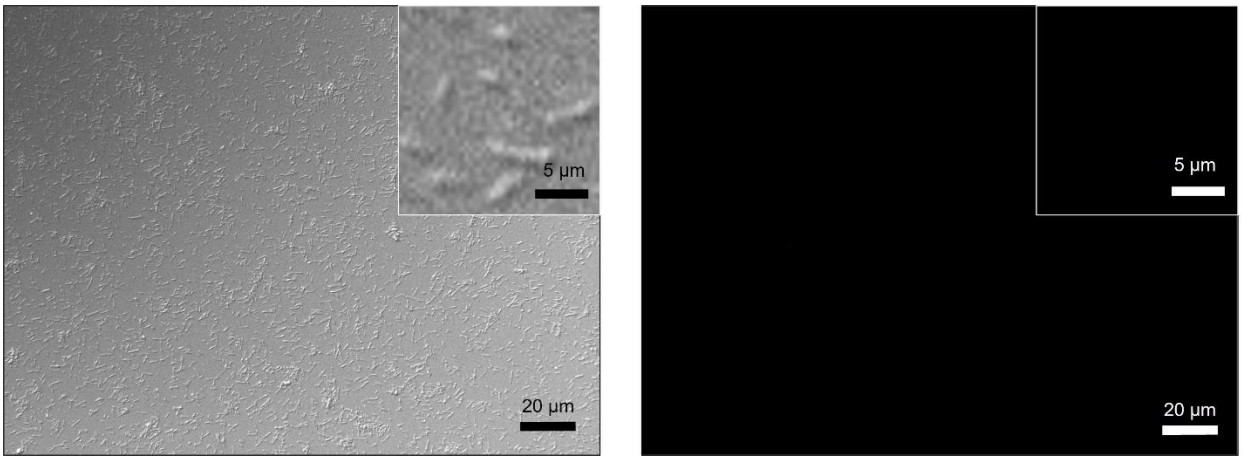

Figure 3.13 In vitro differential interference contrast (DIC) (left) and green fluorescence (right) imaging of RP. Bacterial concentration was 5.0×10^9 CFU mL^{-1}. The upper right images represent higher magnification for each DIC and green fluorescence picture.

The Alexa488-BSA loading concentration was calculated as ~582 µg mL^{-1} to 5×10^9 CFU mL^{-1} of RP through a bicinchoninic acid assay. Anchored Alexa488-BSA–BAM conjugates were maintained on bacterial membrane for about 12 h (Figure 3.14). These results clearly demonstrated that BAM bioconjugates could be effectively and safely bound to the RP bacterial membrane though simple synthesis steps.

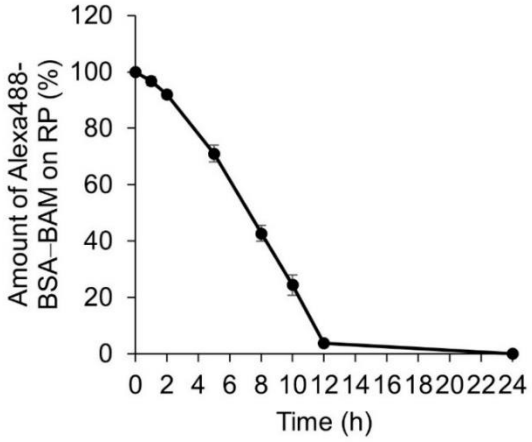

Figure 3.14 Retention times of Alexa488-BSA–BAM conjugates anchored onto bacterial cell membrane. Data are presented as means ± SEM; n = 3 independent experiments

3.3.3 *In vivo* tumor elimination using NIR light-driven functional RPs

Immune checkpoint inhibitor antibodies have revolutionized immunotherapy in cancer.[39] In particular, this includes the use of programmed cell-death protein 1 (PD-1) and programmed cell-death ligand 1 (PD-L1) inhibitors as standard therapy for first-line or second-line treatment of cancer patients. Besides, systemic half-life of antibodies is a critical factor for effective treatment against various diseases. Basically, IgG including anti-PD-1 and anti-PD-L1 has a relatively long-term half-life in blood (ca. 3 weeks).[40] Moreover, considering the fact that there are numerous excellent achievements of the immune checkpoint inhibitors for clinical applications, the efficacy and bioavailability of these inhibitors in vivo are outstanding. In this study, anti-mouse PD-L1 monoclonal antibody (anti-PD-L1) was anchored to the RP membrane as a model therapeutic molecule via BAM coating using the same preparation as Alexa488-BSA–BAM–RP to regulate in vivo immunological functions in the tumor microenvironment (Figure 3.15).

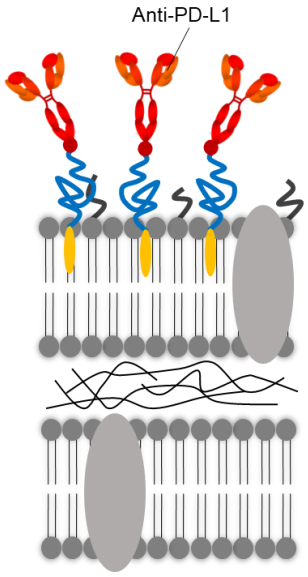

Figure 3.15 Schematic illustration of modified anti-PD-L1–PEG molecules on the RP membrane.

The concentration for successful modification of anti-PD-L1 onto the RP membrane was ~475 μg mL^{-1} against 5×10^9 CFU mL^{-1} of RP. The loading capacity of Anti-PD-L1 on bacterial membrane could be also estimated at approximately 96.1% by flow cytometry analyses of Alexa Fluor® 488-conjugated Anti-PD-L1 (Alexa488-Anti-PD-L1)-modified BAM–RP (Alexa488-Anti-PD-L1–BAM–RP) and natural RP (Figure 3.16).

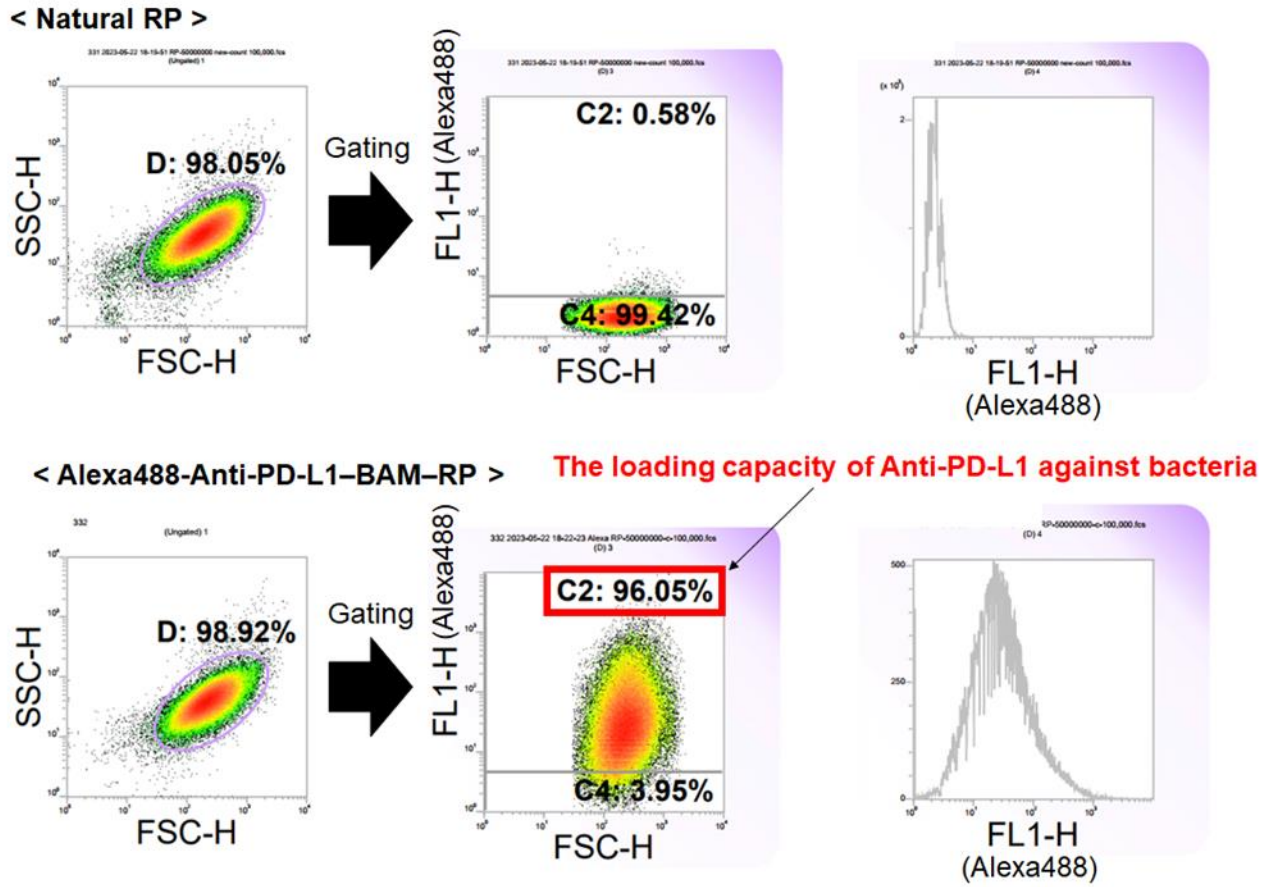

Figure 3.16 Flow cytometry analyses of Alexa488-Anti-PD-L1–BMA–RP and natural RP

To evaluate whether the prepared anti-PD-L1-modified RP via BAM (anti-PD-L1–BAM–RP) can be applied for cancer phototherapy, its photothermal conversion properties were first determined using an 808 nm laser (Figure 3.17). Both anti-PD-L1–BAM–RP and natural RP exhibited

powerful photothermal conversion owing to the strong optical ability of the light-driven BChl molecules within the cells (Figure 3.17a). Notably, anti-PD-L1–BAM–RP showed excellent photothermal stability (Figure 3.17b and 3.17c). Maximum temperatures were fundamentally unchanged even after five heating and cooling seamless cycles at 0.6 W (~3.1 W cm^{-2}) laser power.

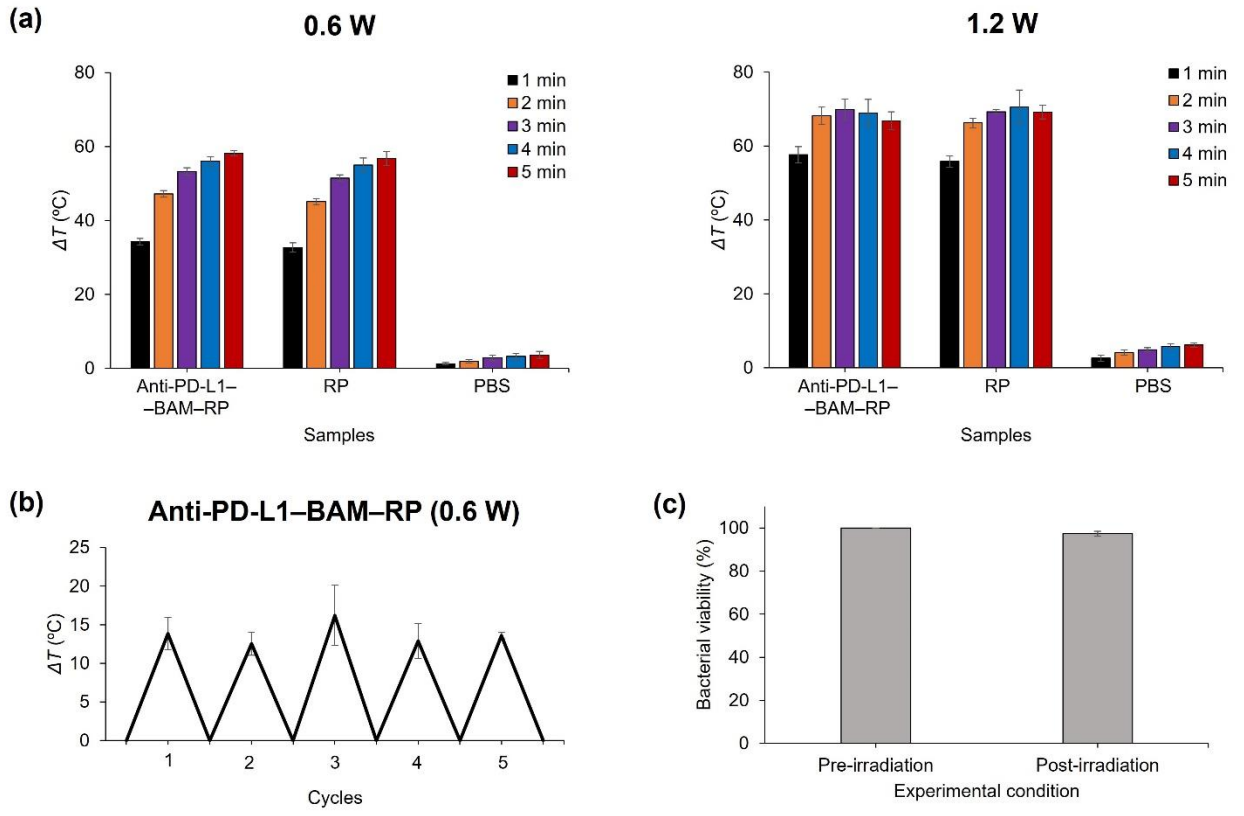

Figure 3.17 Photothermal conversion of anti-PD-L1–BAM–RP. (a) Temperature difference (ΔT) of the various sample solutions after irradiation with 808 nm laser at 0.6 W (~3.1 W cm^{-2}) (left figure) and 1.2 W (~6.1 W cm^{-2}) (right figure) at different time points (1, 2, 3, 4, and 5 min). RP concentration was approximately 5.0×10^8 CFU well–1. Data are presented as means ± SEM; n = 3 independent experiments. (b) Stability testing of the anti-PD-L1–BAM–RP solution under photothermal heating and natural cooling cycles under 808 nm laser irradiation at 0.6 W (~3.1 W cm^{-2}) power. RP concentration was approximately 2.5×10^8 CFU $well^{-1}$. Data are presented as means ± SEM; n = 3 independent experiments. (c) Photothermal stability of anti-PD-L1–BAM–RP after laser irradiation at 0.7 W (~3.6 W cm^{-2}) for two times. RP concentration was approximately 5.0×10^8 CFU $well^{-1}$. Data are presented as means ± SEM; n = 3 independent experiments.

Next, the in vitro anticancer therapeutic efficacy of laser-induced anti-PD-L1–BAM–RP was investigated using the human diploid (WI38) and Colon26 cell lines (Figure 3.18). The cells were incubated with various anti-PD-L1–BAM–RP concentrations in 96-well plates for 4 h without NIR laser exposure to confirm the cytotoxicity against normal and cancer cells (Figure 3.18a). Anti-PD-L1–BAM–RP did not show strong cytotoxicity for these cells. Subsequently, the laser-induced cytotoxicity of anti-PD-L1– BAM–RP was evaluated (Figure 3.18b). Cells were effectively eliminated after laser irradiation for only 5 min at 1.2 W (~6.1 W cm^{-2}) of power owing to the potent photothermal conversion of anti-PD-L1–BAM–RP.

Next, the in vivo biological distributions and tumor-targeting effects of anti-PD-L1–BAM–RP were investigated using near-infrared window (NIR-I, 700–900 nm) fluorescence bioimaging. We have already verified that RP itself exhibits excellent tumor-targeting.[24] Nevertheless, based on in vivo NIR bioimaging analyses, the prepared anti-PD-L1–BAM–RP displayed higher tumor selectivity in Colon26-bearing immunocompetent mice, compared with natural RP, owing to PEG coating (Figures 3.19a). Bright NIR fluorescence from RP was observed in the targeted tumor after intravenous injection of anti-PD-L1–BAM–RP for 8 days. In contrast, pristine RP mainly accumulated in the liver and spleen, in addition to the tumor. The high water solubility and superior immunological blocking of PEG brushes on the bacterial membrane could facilitate long-term blood circulation of anti-PD-L1–BAM–RP, giving them higher tumor selectivity.[41,42] Colony assay also demonstrated specific tumor-targeting property of anti-PD-L1–BAM–RP (Figure 3.20). Although colony assay says that natural RP also has a high tumor-targeting effect (Figure 3.20). However, as shown in Figure 3.21, bright FL in liver and spleen attributed from bacterial pigments after treatment with natural RP indicate that RP is reluctantly distributed in these organs, and potentially cause side effects and misdiagnosis during treatment, especially when the target tumors

are existed in liver and spleen. In any case, these results demonstrate that anti-PD-L1–BAM–RP exhibit high tumor selectivity and does not physiologically interfere with vital organs, potentially reducing side effects and medical mishaps.

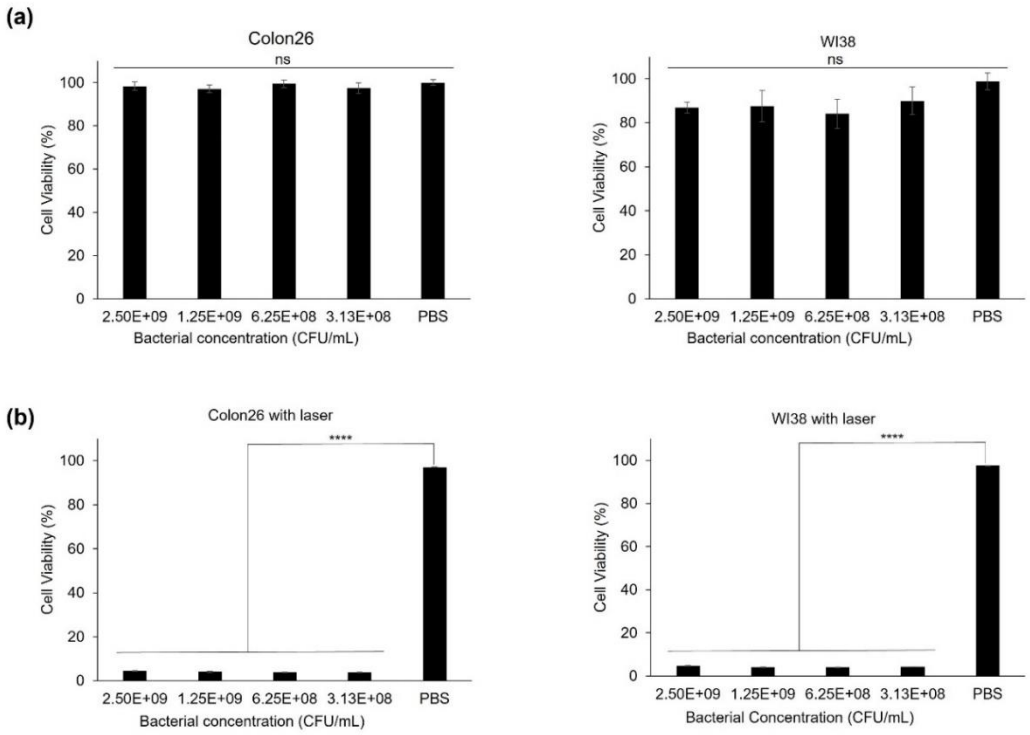

Figure 3.18 Laser-induced cytotoxicity of anti-PD-L1–BAM–RP. (a) Viability of Colon26 and WI38 cells treated with PBS buffer (control) and anti-PD-L1–BAM–RP at various bacterial concentrations without laser irradiation. Cell viability was tested after incubation with 4 h treatment of bacteria. Data are presented as means ± SEM; n = 5 biologically independent tests; ns, not significant. (b) Anti-PD-L1–BAM–RP cytotoxicity evaluation in Colon26 and WI38 cells after 4 h of treatment with 5 min laser irradiation [1.2 W (ca. 6.1 W cm^{-2})] at various bacterial concentrations. Data are presented as means ± SEM; n = 3 biologically independent tests. ***** $P < 0.0001$ vs. control (Student's t-test). Multiplicity of infections (MOIs) of each bacterial concentration (3.13×10^8, 6.25×10^8, 1.25×10^9, and 2.5×10^9 CFU/mL) are 13413, 26827, 52655, and 107311.

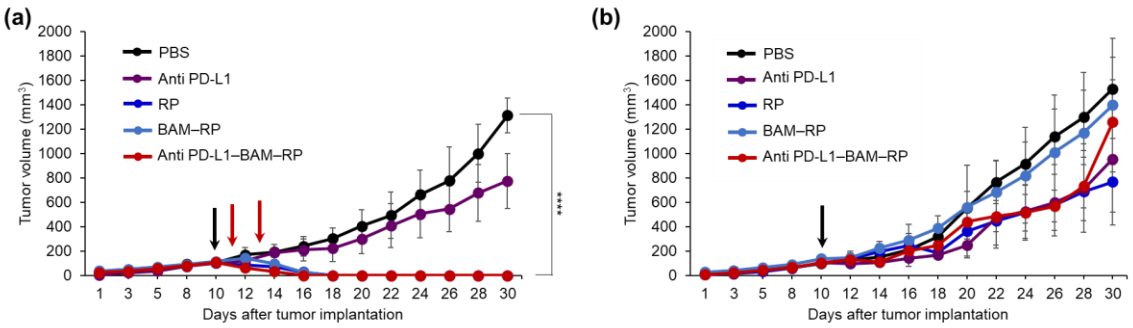

Figure 3.19 In vivo antitumor efficacies of anti-PD-L1–BAM–RP with and without laser irradiation. (a) Relative tumor volumes on the mouse right flank after i.t. injection of PBS or PBS dispersions of anti-PD-L1, RP, BAM–RP, or anti-PD-L1–BAM–RP with-out laser irradiation. RP concentration was approximately 5.0×10^8 CFU tumor^{-1}. Data are presented as means ± SEM (n = 4 biologically independent tests). The black arrow indicates the time point of bacterial injection. (b) Relative tumor volumes on the laser-irradiated mouse right flank. PBS or PBS dispersions of Anti-PD-L1, RP, BAM–RP, or Anti-PD-L1–BAM–RP were injected i.t., and the injected tumors were treated with 808 nm laser irradiation [laser power = 713 mW (~3.6 W cm^{-2}); irradiation time = 3 min] 24 h after the injections. RP concentration was approximately 5.0×10^8 CFU tumor^{-1}. Data are presented as means ± SEM (n = 4 biologically independent tests), ****P < 0.0001 (Student's t-test for PBS). Black and red arrows represent the time points of bacterial injection (day 10) and laser irradiations (day 11 and day 13), respectively.

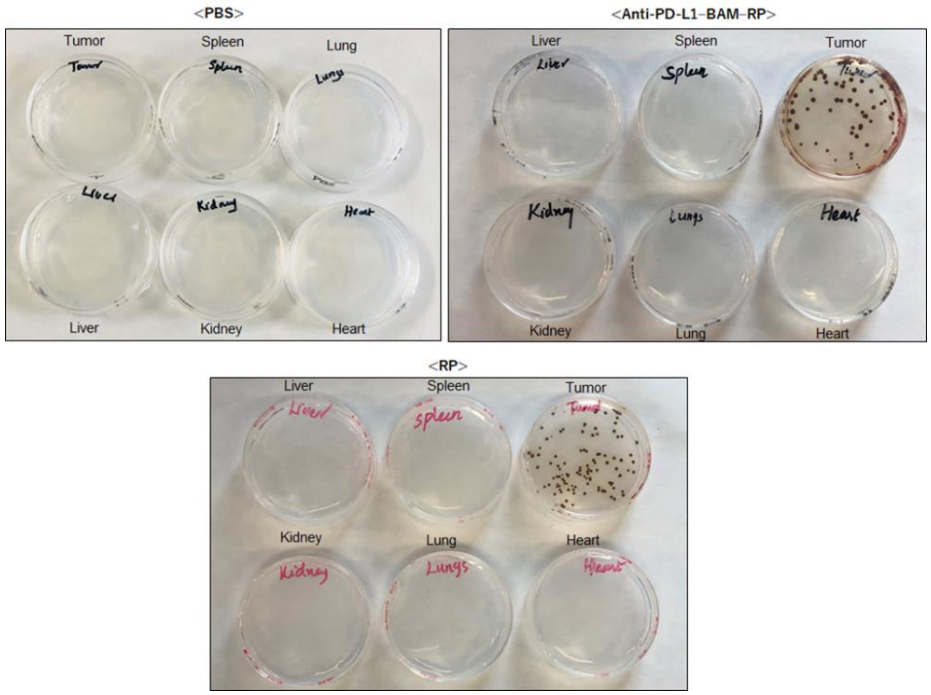

Figure 3.20 Tumor targeting effect of Anti-PD-L1–BAM–RP. Bacteria colony of organs/tumors of Colon26 tumor-bearing mice over time after intravenous injection of PBS (100 μL), Anti-PD-L1–BAM–RP (100 μL, 5×10^9 CFU mL–1) or RP (100 μL, 5×10^9 CFU mL–1) for 144 h.

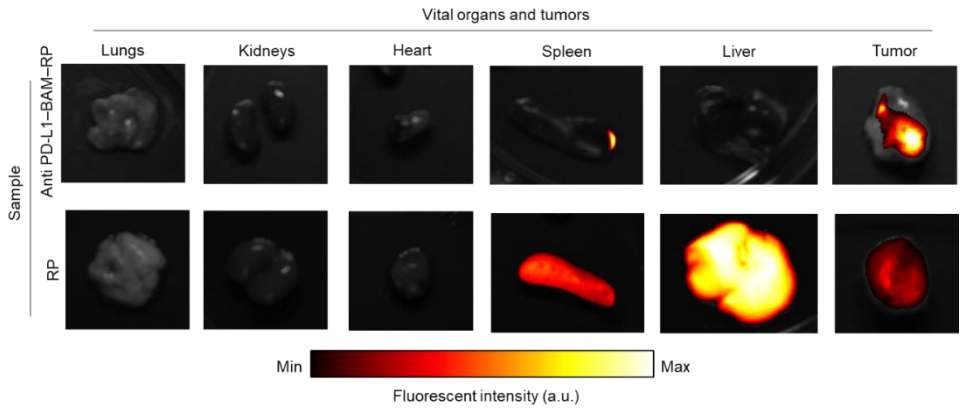

Figure 3.21 NIR fluorescence imaging of Colon26 tumors and major organs 192 h post-i.v. injection of anti-PD-L1–BAM–RP (200 μL, 5.0×10^8 CFU) (upper) and conventional RP (200 μL, 5.0×10^8 CFU) (lower). Tumor volume was about 400 mm^3.

The laser-induced anticancer therapeutic efficacies of anti-PD-L1–BAM–RP were further investigated using a Colon26-bearing syngeneic model (Figure 3.22).

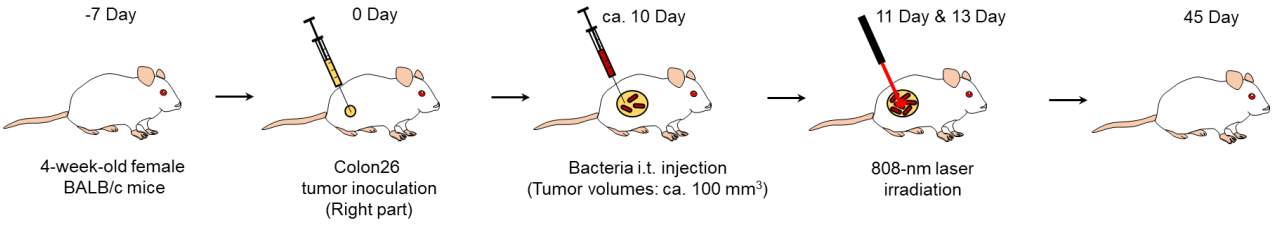

Figure 3.22 Schematic illustration of in vivo Colon26 carcinoma antitumor tests using laser-induced Anti-PD-L1–BAM–RP

Colon26-bearing mice were intratumorally injected with 100 μL of RP (5×10^9 CFU mL^{-1}), anti-PD-L1–BAM–RP (RP, 5×10^9 CFU mL^{-1}; anti-PD-L1, 475 μg mL^{-1}), PBS, or PBS containing anti-PD-L1 (2.5 mg kg body weight–1, 475 μg mL^{-1}). After bacterial accumulation for 24 h, the NIR-I fluorescence of anti-PD-L1–BAM–RP was confirmed to identify the tumor location (Figure 3.23), and the solid tumors were then irradiated using an NIR laser at 0.7 W (~3.6 W cm^{-2}) for 3 min. Subsequently, the body surface temperature was monitored and analyzed using an infrared thermographic camera during laser irradiation (Figure 3.24a and 3.24b). The maximum surface temperatures of the solid tumors in the mice were reached at 55 ºC after injection of anti-PD-L1–BAM–RP or RP alone with laser irradiation for 3 min. In contrast, the control PBS and anti-PD-L1 groups did not show high surface temperature after laser irradiation due to the lack of photothermal conversion properties.

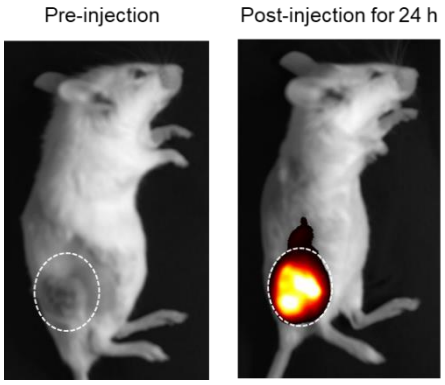

Figure 3.23 Fluorescence imaging of Colon26 tumor-bearing mice after i.t injection of Anti-PD-L1–BAM–RP (100 µL, 5×10^8 CFU). White dashed circles represent tumor locations.

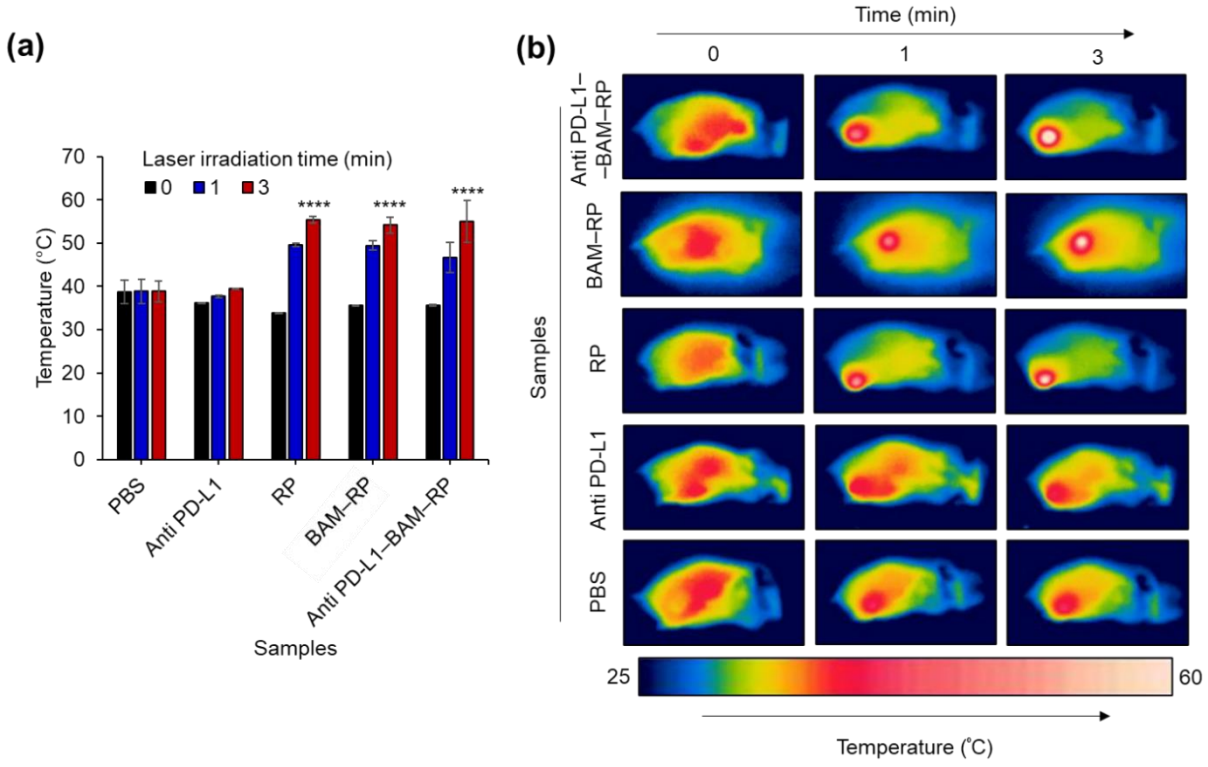

Figure 3.24 (a) Surface temperature of the solid tumor in Colon26-bearing mice on the 2nd day after i.t. injection with PBS, anti-PD-L1, RP, or anti-PD-L1–BAM–RP, followed by 808 nm laser irradiation [laser power = 0.7 W (~3.6 W cm^{-2})] at different time points (0, 1, and 3 min). RP concentration was approximately 5.0×10^8 CFU $tumor^{-1}$. Data are presented as means ± SEM; n = 3 independent experiments. Statistical significance was calculated through comparison with the PBS group. ****, $P < 0.0001$. (b) Infrared thermal images of laser-induced mice at various time points (0, 1, and 3 min).

Although anti-PD-L1–BAM–RP, RP and anti-PD-L1 inhibited tumor growth (Figure 3.19b), laser-induced anti- PD-L1–BAM–RP, laser-induced BAM–RP, and laser-induced RP demonstrated an especially dramatic anticancer effect. The solid tumors disappeared completely after laser irradiation with anti-PD-L1–BAM–RP, BAM–RP, or RP (Figure 3.19a). As a result, 100% complete responses were achieved in anti-PD-L1–BAM–RP, BAM–RP, and RP via laser irradiation at the bacterial concentration (5.0×10^8 CFU tumor^{-1}) during the 30-day follow-up period after the experiment, owing to the powerful photothermal conversion effect of bacteria (Figure 3.25). Among them, laser-induced anti- PD-L1–BAM–RP exhibited the strongest efficacy in the primary treatment stage (Figure 3.26). Notably, treatment with anti-PD-L1–BAM–RP with laser irradiation apparently cured tumors and injured parts faster than laser-induced RP and laser-induced BAM–RP owing to the stronger immunological efficacy of anti-PD-L1–BAM–RP (Figure 3.27).

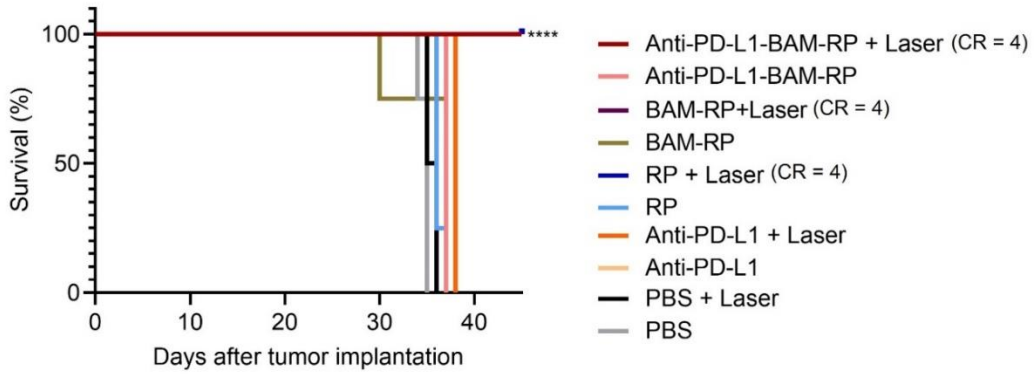

Figure 3.25 Kaplan–Meier survival curves of Conlon26-tumor-bearing mice (n = 3 biologically independent mice) after tumor implantation for 45 days. Statistical significance was calculated in comparison with PBS group. ****, $p < 0.0001$. The groups of Anti-PD-L1–BAM–RP + laser and RP + laser showed 100% survival rate at least for 45 days.

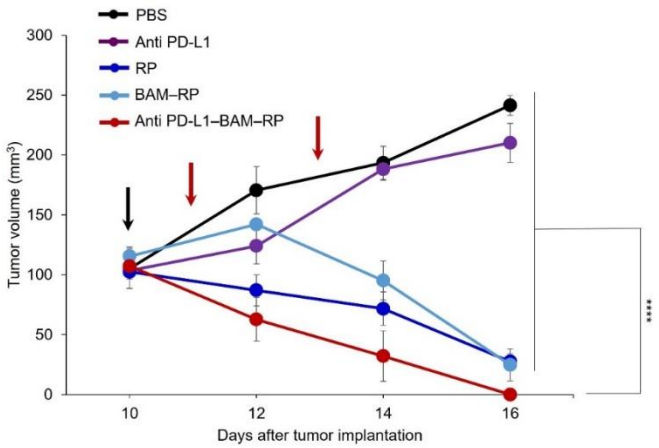

Figure 3.26 In vivo antitumor efficacies of various functional bacterial complexes with laser irradiation (magnified view of graph from day 10 to day 16 in Figure 3.19b). Relative tumor volumes on the laser-irradiated mouse right flank. PBS or PBS dispersions of Anti-PD-L1, RP, BAM–RP, or Anti-PD-L1–BAM–RP were injected i.t., and the injected tumors were treated with 808 nm laser irradiation [laser power = 713 mW (~3.6 W cm^{-2}); irradiation time = 3 min] 24 h after the injections. RP concentration was approximately 5.0×10^8 CFU $tumor^{-1}$. Data are presented as means ± SEM (n = 4 biologically independent tests), ****P < 0.0001 (two-way ANOVA). Black and red arrows represent the time points of bacterial injection (day 10) and laser irradiations (day 11 and day 13), respectively.

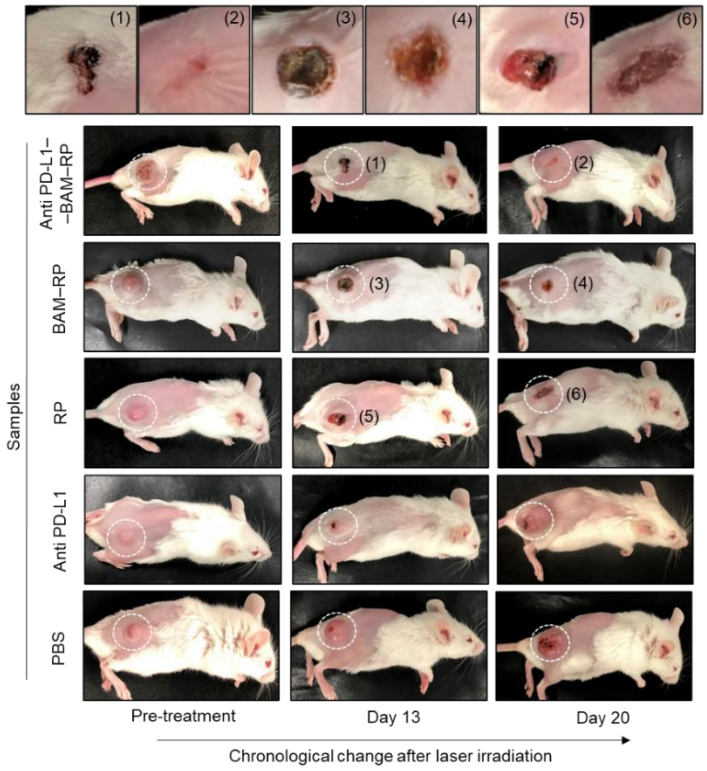

Figure 3.27 Images of mice after each treatment. The upmost images (1, 2, 3, and 4) represent higher magnification of each numbered area in the lower images.

Moreover, the antitumor efficacy of laser-induced anti-PD-L1–BAM–RP is also better than that of laser-induced RP at the low bacterial concentration (2.5×10^8 CFU tumor^{-1}) (Figure 3.28). In contrast, the anti-PD-L1 groups showed somewhat effective tumor suppression with or without laser irradiation, compared with the control PBS groups. There was no severe body weight reduction after bacteria injection with or without laser irradiation, indicating no side effects (Figure 3.29). Furthermore, anti-PD-L1–BAM–RP did not show in vivo toxicity according to blood tests (Table 3.1).

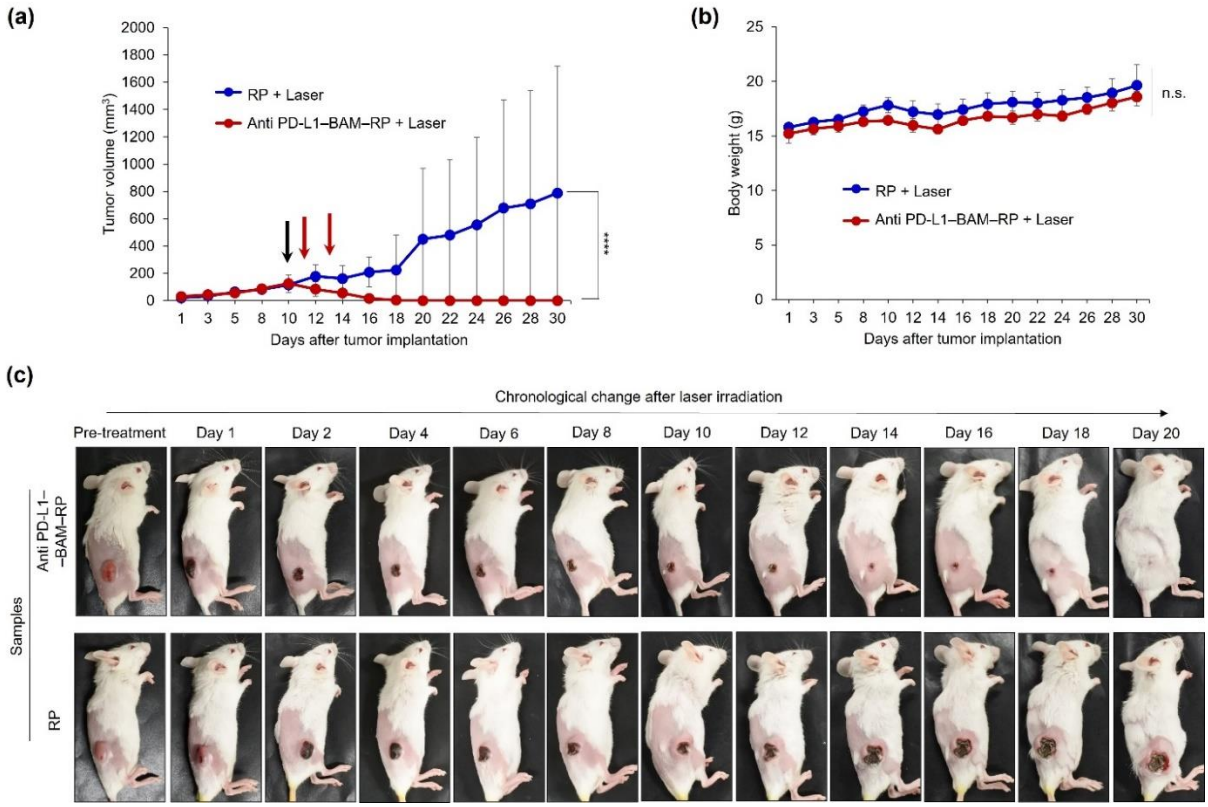

Figure 3.28 In vivo antitumor efficacies of laser-induced anti-PD-L1–BAM–RP and RP at the low bacterial concentration. (a) Relative tumor volumes on the laser-irradiated mouse right flank. PBS dispersions of RP or Anti-PD-L1–BAM–RP were injected i.t., and the injected tumors were treated with 808 nm laser irradiation [laser power = 713 mW (~3.6 W cm^{-2}); irradiation time = 3 min] 24 h after the injections. RP concentration was approximately 2.5×10^8 CFU $tumor^{-1}$. Data are presented as means ± SEM (n = 4 biologically independent tests), ****P < 0.0001 (Student's t-test for PBS). Black and red arrows represent the time points of bacterial injection (day 10) and laser irradiations (day 11 and day 13), respectively. (b) Average mouse body weight after treatments during the treatment period. (c) Images of mice after each treatment.

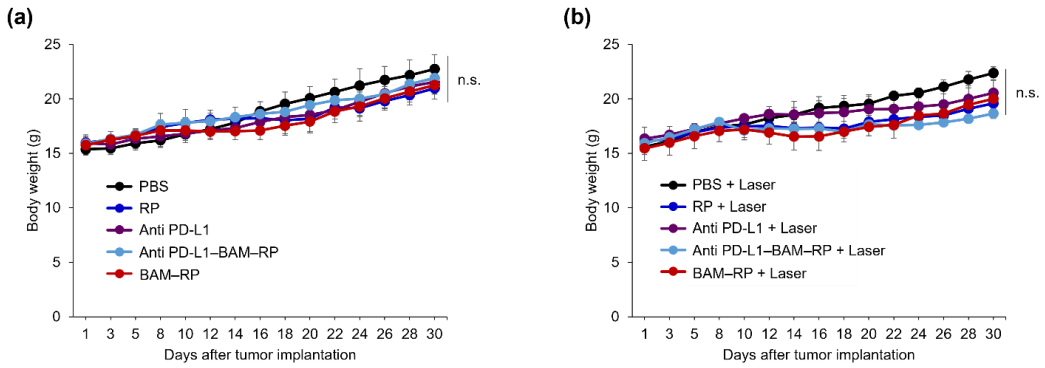

Figure 3.29 Average mouse body weight after bacterial and control treatments during the treatment period (a) without and (b) with laser irradiation. Data are presented as means ±SEM; n = 4 biologically independent mice. ns, not significant.

After 30 days, there was no statistically significant difference in the complete blood count or biochemical parameters of mice intravenously injected with PBS or anti-PD-L1–BAM–RP suspension. Meanwhile, the maximum permissible exposure for skin using an 808-nm laser is approximately 0.33 W cm^{-2} according to the American National Standard.[43] Notably, a higher-powered laser density (ca. 3.6 W cm^{-2}) itself used in this study did not indicate any damage against skin and tissue presumably because of short-term irradiation (only 3 min for each treatment). In fact, the irradiated parts of living mice were not burned at all even after repetitive irradiations with PBS i.t. administration (Figure 27). We also confirmed that laser-induced functional bacteria complexes can safely keep their rigid photo-thermal stability in the tumor milieu as well as photothermal conversion and anticancer efficacy are actually controllable by the high-powered laser while not inducing photo toxicity and dark toxicity.[44] These results clearly indicate that the laser-driven bacterial treatment is not only photothermally effective but also optically safe. These results clearly indicated that the bioactive PEGylated bacteria hybrid was effective and safe as an in vivo photothermal agent, and both photothermal conversion and immunological stimulation could exert synergetic antitumor therapeutic effects.

Table 3:1 CBCs and biochemical parameters of the mice injected with PBS or Anti-PD-L1–BAM–RP dispersion after 30 days.

Measured value	Entry	Unit	PBS (n = 10)	Anti-PD-L1–BAM–RP (n = 10)	P value
CBC	WBC	$\times 10^2\ \mu L^{-1}$	87.2 ± 13.22	76.6 ± 19.51	> 0.05
	RBC	$\times 10^4\ \mu L^{-1}$	953.8 ± 46.07	926.8 ± 33.11	> 0.05
	HGB	$g\ dL^{-1}$	14.1 ± 0.66	13.6 ± 0.41	> 0.05
	HCT	%	44.1 ± 1.92	43.3 ± 1.34	> 0.05
	MCV	fL	46.3 ± 0.47	46.7 ± 0.71	> 0.05
	MCH	pg	14.8 ± 0.11	14.7 ± 0.22	> 0.05
	MCHC	$g\ dL^{-1}$	31.9 ± 0.37	31.4 ± 0.35	> 0.05
	PLT	$\times 10^4\ \mu L^{-1}$	71.0 ± 5.32	63.2 ± 5.32	> 0.05
Biochemical parameters	TP	$g\ dL^{-1}$	3.9 ± 0.12	4.0 ± 0.17	> 0.05
	ALB	$g\ dL^{-1}$	2.6 ± 0.07	2.7 ± 0.08	> 0.05
	BUN	$mg\ dL^{-1}$	24.3 ± 3.03	24.8 ± 3.05	> 0.05
	CRE	$mg\ dL^{-1}$	0.1 ± 0.02	0.1 ± 0.01	> 0.05
	Na	$mEq\ L^{-1}$	152.2 ± 1.14	153.0 ± 1.16	> 0.05
	K	$mEq\ L^{-1}$	3.8 ± 0.29	3.8 ± 0.26	> 0.05
	Cl	$mEq\ L^{-1}$	117.4 ± 1.84	118.7 ± 1.42	> 0.05
	AST	$IU\ L^{-1}$	60.2 ± 6.86	74.6 ± 31.4	> 0.05
	ALT	$IU\ L^{-1}$	40.0 ± 10.35	47.3 ± 17.24	> 0.05
	LDH	$IU\ L^{-1}$	269.0 ± 42.35	264.1 ± 129.65	> 0.05
	AMY	$IU\ L^{-1}$	1853.1 ±153.60	1808.7 ± 114.07	> 0.05
	CK	$IU\ L^{-1}$	155.9 ± 66.42	135.9 ± 88.81	> 0.05

Data are represented as means ± standard errors of the mean (s.e.m.); n = 5 biologically independent mice. Statistical analyses comprise the two-way ANOVA test.

Abbreviations: ALB, albumin; ALT, alanine transaminase; AMY, amylase; AST, aspartate aminotransferase; BUN, blood urea nitrogen; Cl, chlorine; CK, creatine kinase; CRE, creatinine; HCT, hematocrit; HGB, hemoglobin; K, potassium; LDH, lactate dehydrogenase; MCH, mean corpuscular hemoglobin; MCHC, mean corpuscular hemoglobin concentration; MCV, mean corpuscular volume; Na, sodium; PLT, platelet; RBC, red blood cell; TP, total protein; WBC, white blood cell.

3.3.4 Tumor suppression mechanism using NIR light-driven functional RP hybrid

The immunological mechanism of solid tumor suppression via laser-induced functional bacteria was investigated using hematoxylin and eosin (H&E) and immunohistochemical (IHC) staining analyses (Figure 3.30 and Figure 31-33). The samples were collected from the treated mice at 48 h for IHC staining because the tumors were drastically destructed after treatments of laser-induced bacteria more than 48 h. To assess tissue apoptotic levels, the tumors were collected and fixed with 4% paraformaldehyde for H&E staining, terminal deoxynucleotidyl transferase-mediated dUTP-biotin nick end labeling (TUNEL) staining, and cleaved caspase-3 staining. Anti PD-L1–BAM–RP, BAM–RP, or RP with laser irradiation caused obvious tumor damage, with intercellular fragmentation, necrosis, and apoptosis in tumor tissues. Encouragingly, anti PD-L1–BAM–RP with laser irradiation evoked the most obvious cell damage with dramatic denaturation of tumor cells and the strongest brown pigmentation among these treatments. The control groups (PBS alone and PBS + laser) did not exhibit intercellular denaturation and apoptotic TUNEL and cleaved caspase-3 color development within the tumor mass.

To unveil the immunological reactions underlying the tumor suppression by laser-induced anti-PD-L1–BAM–RP, IHC staining of F4/80 (macrophage marker) and CD3 (T cell marker) was performed. Interestingly, although there were no significant F4/80 and tumor necrosis factor-α (TNF-α) color developments in laser-induced anti-PD-L1–BAM–RP, tumor tissues clearly exhibited CD3 expression in the anti-PD-L1– BAM–RP + laser and anti-PD-L1–BAM–RP alone groups. This indicates that immunological aggressive T cells are immersed in the tumor milieu thanks to the activity of anti-PD-L1 on the bacterial membrane, in addition to the protection against macrophages owing to RP PEGylation, as shown in Figure 3.6g. Furthermore, anti-PD-L1 and anti-PD-L1–BAM–RP also showed strong CD3 expression regardless of laser irradiation. Anti-

PD-L1 can block the PD-L1 receptor on cancer cells, facilitating their destruction by cytotoxic T cells with the pore-forming protein perforin and serine protease granzymes.[45] On the other hand, macrophages are presumably an immunologically dominant factor to eliminate colorectal cancerous tumor in RP with and without laser irradiation because of their strong F4/80 and TNF-α color developments. TNF-α is a cytotoxic functional cytokine secreted primarily by macrophages. The PBS alone and PBS + laser groups did not show significant pigmentations in the TNF-α, F4/80, and CD3 slices. To further explore the therapeutic mechanism, other T cell makers (CD4, CD8, and PD-1) and NK cell markers (IFN-γ and NKp46) were qualitatively and quantitatively analyzed in tumor tissues and spleens after the treatment of each sample (Figure 3.31–3.33). The anti-PD-L1–BAM–RP + laser group showed apparent T cell activation in tumor tissues thanks to the synergetic effects of photothermal conversion of bacteria with the help of successful T cell stimulations by anti-PD-L1 molecule. Besides, anti-PD-L1–BAM–RP also displayed significant color developments with regard to T cell markers of both CD4 and CD8 in spleens because of effective T cell activation by anti-PD-L1 and immunogenic bacterial stimulants. The color developments involved with NK cell stimulations were not so obvious in any groups in both tumors and spleens. Collectively, we consider that laser-induced anti-PD-L1–BAM–RP demonstrated obvious tumor suppression and fast injury healing due to synergistic cytotoxic T cell activation and exothermic eradication of cancer cells by effective blocking of PD-L1 on cancer cells and powerful photothermal conversion of anti-PD-L1–BAM–RP (Figure 3.34).

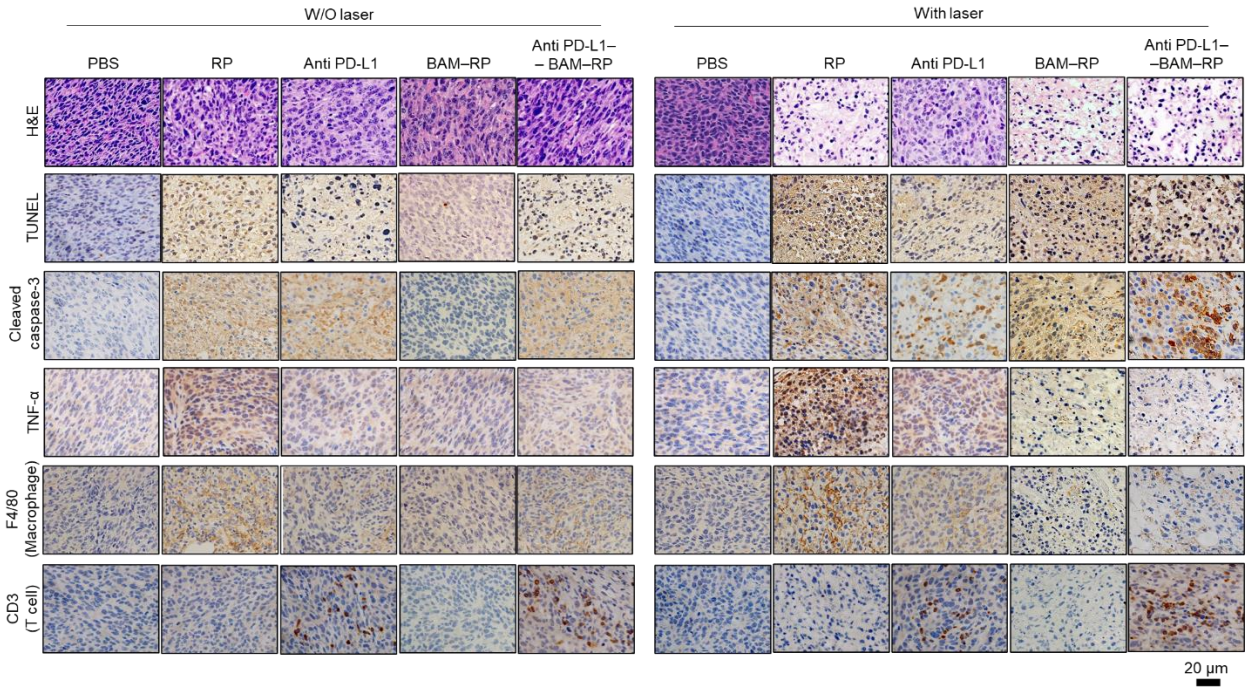

Figure 3.30 Mechanism of tumor suppression by NIR light-driven anti-PD-L1–BAM–RP. (a) H&E, TUNEL, and IHC (caspase-3, F4/80, TNF-α, F4/80, and CD3)-stained tumor tissues collected from different groups of mice on day 2 after treatments.

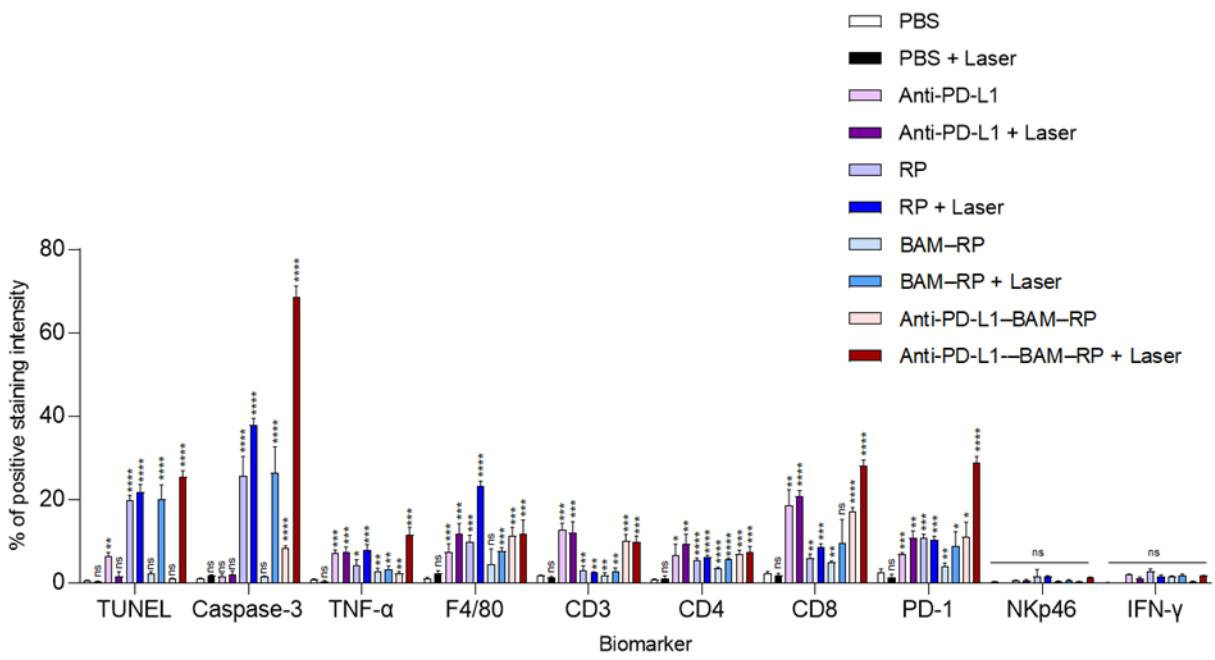

Figure 3.31 Statistical analyses of IHC (caspase-3, TNF-α, F4/80, CD3, IFN-γ, PD-1, CD8, CD4, and NKp46) and TUNEL-positive stained tumor tissues in Figure 7A and Figure S20 after i.t. injection of each sample with or without laser irradiation. Data are represented as mean ± SEM; n = 3 independent areas (region of interest) in each tumor tissue collected from the groups of mice on day 1 after treatments. Statistical significance was calculated in comparison with the PBS group. ns, not significant, *, $p < 0.05$, **, $p < 0.01$, ***, $p < 0.001$, and ****, $p < 0.0001$, by Student's t two-sided test.

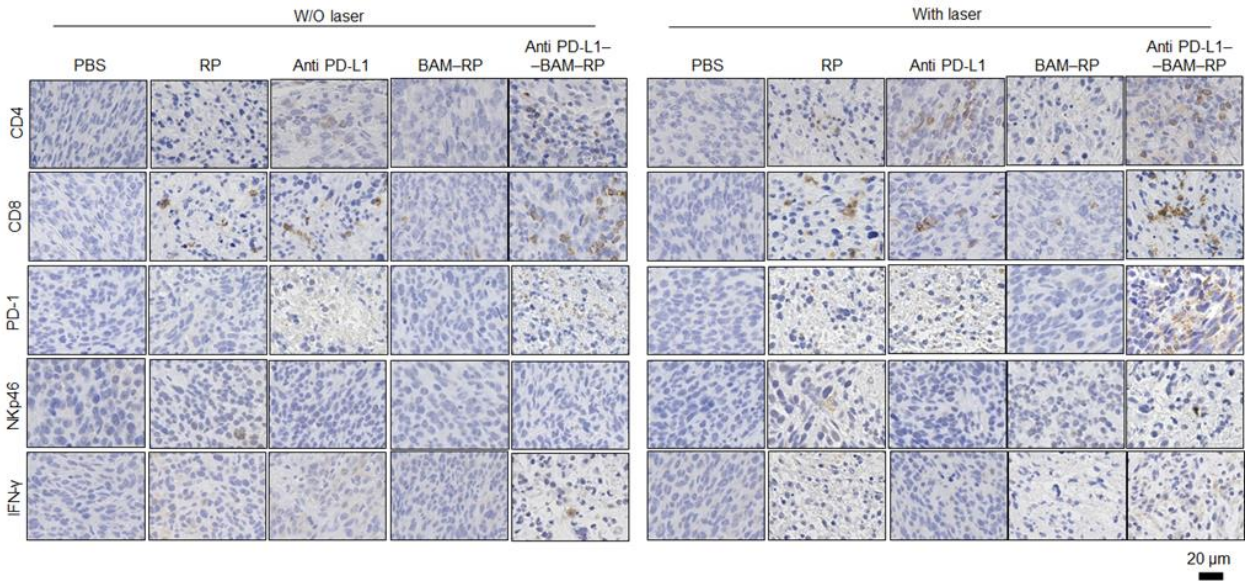

Figure 3.32 IHC staining for IFN-γ, PD-1, CD8, CD4, and NKp46 in tumor tissues after i.t. injection of each sample with or without laser irradiation.

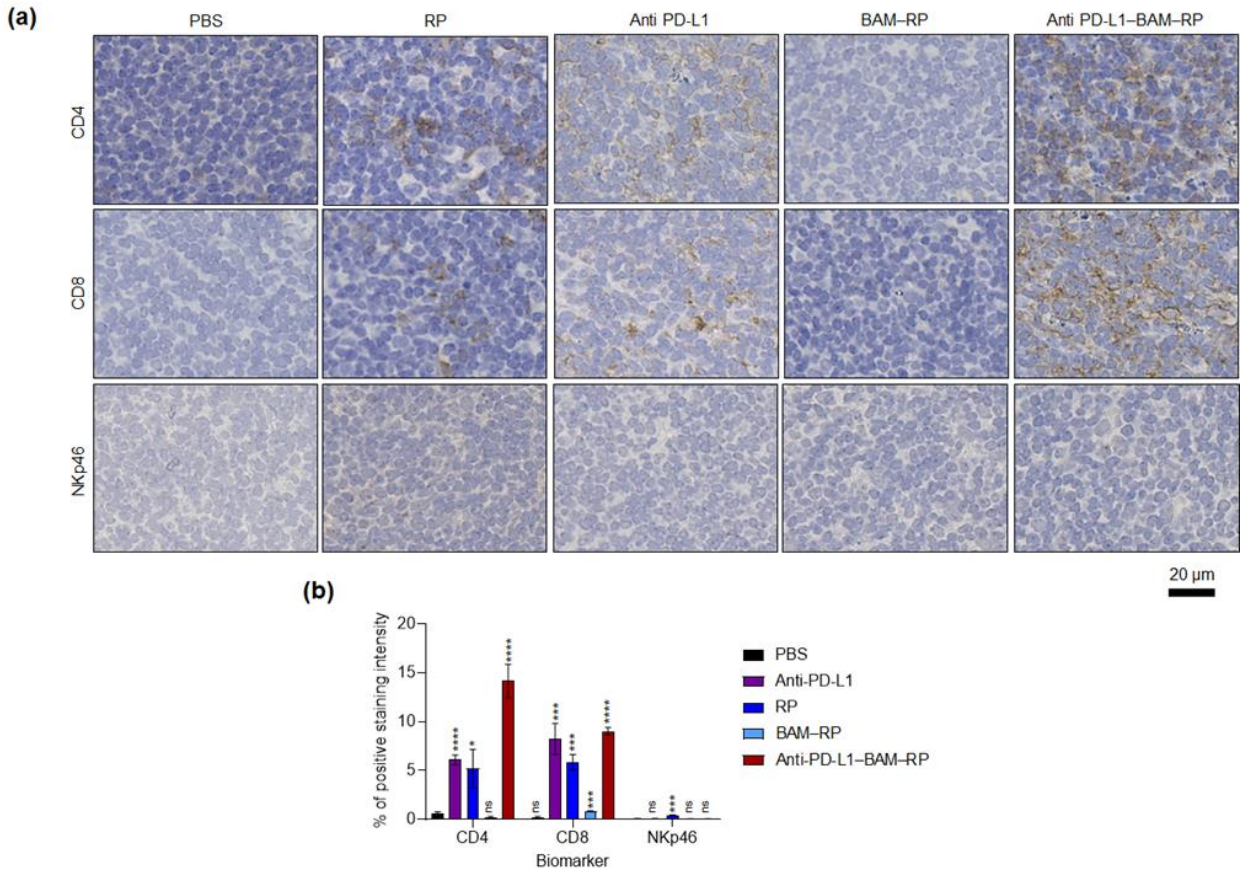

Figure 3.33 (a) Qualitative and (b) quantitative analyses of IHC staining for CD8, CD4, and NKp46 in spleens after i.v. injection of each sample. Data are represented as mean ± SEM; n = 3 independent areas (region of interest) in each tumor tissue collected from the groups of mice on day 1 after treatments. Statistical significance was calculated in comparison with the PBS group. ns, not significant, *, $p < 0.05$, **, $p < 0.01$, ***, $p < 0.001$, and ****, $p < 0.0001$, by Student's t two-sided test.

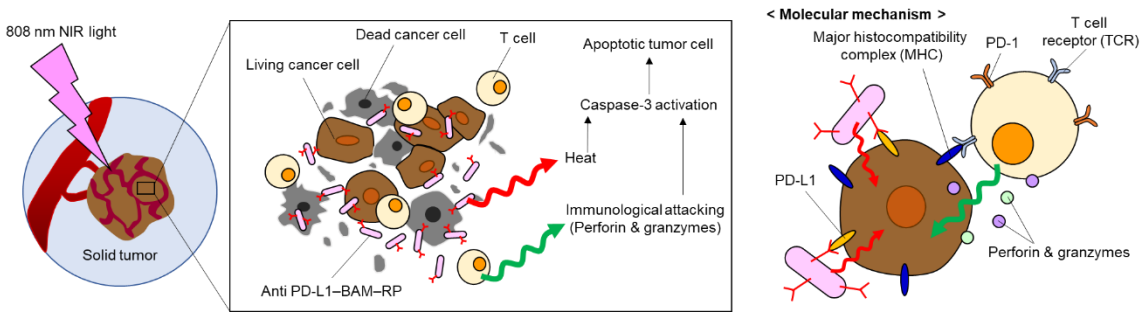

Figure 3.34 Scheme of the proposed mechanism of tumor suppression by NIR light-driven anti-PD-L1–BAM–RP

Table 3:2 Antibodies used in this study.

Antibody	Type	Source	Catalog No.	Application
Anti-digoxigenin-peroxidase	Sheep Polyclonal	Merck Millipore	S7100	Tunel
Caspase-3	Rabbit Polyclonal	Cell Signaling Technology	9661S	IHC (1:100)
TNF-α	Rabbit Polyclonal	Abcam	ab6671	IHC (1:100)
F4/80	Mouse Monoclonal	BMA Biomedicals	T-2028	IHC (1:50)
CD3	Rabbit Monoclonal	Abcam	ab16669	IHC (1:100)
CD4	Rabbit Monoclonal	Cell Signaling Technology	25229	IHC (1:100)
CD8	Rabbit Monoclonal	Cell Signaling Technology	98941	IHC (1:200)
NKp46	Rabbit Polyclonal	Affinity Biosciences	DF7599	IHC (1:100)
IFN-γ	Rabbit Polyclonal	Abcam	ab9657	IHC (1:100)
PD-1	Rabbit Polyclonal	Bioss	bs-1867R	IHC (1:200)

3.4 CONCLUSION

To sum up, several bacterial strains were screened and a potent PPSB, RP, with high performance was identified for efficient cancer phototherapy. Using a range of PEG compounds and biomolecules, chemically modified RP complexes were created utilizing incubation and washing procedures to further improve RP functioning. The bioactive PEGylated RPs, particularly those that included a BAM macromolecule, demonstrated robust NIR absorbance and fluorescence, high biocompatibility, possess the ability to form healthy bacterial colony, effective photothermal conversion, and the ability to evade the immune system. Using biologically penetrating NIR light, we also demonstrated how an immuno-activatable anti-PD-L1 molecule-coated RP with BAM might be used as an optical theranostic agent. Due to T cell activation by anti-PD-L1, strong photothermal conversion and high tumor selectivity of RP, and immunological avoidance due to PEGylation, NIR laser-induced anti-PD-L1–BAM–RP displayed potent antitumor activity with successful tumor targeting. This study offers, to the best of our knowledge, the first instance of chemical functionalization of living microorganisms for optically activated bacteria-based theranostics with immunoregulatory characteristics. This approach and the bioengineering of bacterial complexes that have been chemically functionalized have generated a great deal of interest in creating multifaceted therapeutic techniques for the treatment of cancer in the future. Furthermore, as illustrated in Figure 3.14, addressing the reduction of bioactive PEGs produced during bacterial division could be a potential area of improvement for the suggested approach. The retention duration of anchoring of bioactive PEGs on the bacterial surface may be improved by using different structural BAM molecules that have relatively high molecular weights of PEG and/or double oleyl chain derivatives.[32] BAM gelation generated by an enzymatic process may enhance the strong anchorage of bioactive PEGs on membranes.[33] We believe that combining the

innate anti-cancer properties found in natural bacteria, such as multiple immunological activations and enhanced conversion,[46] with synthetic therapeutic materials is essential for advancing medical applications in the future. Further exploration and expansion of these properties is crucial.

3.5 REFERENCES

(1) Kumar, N.; Fazal, S.; Miyako, E.; Matsumura, K.; Rajan, R. Avengers against Cancer: A New Era of Nano-Biomaterial-Based Therapeutics. *Mater. Today* **2021**, *51*, 317–349.

(2) Hoffman, R. M. *Bacterial Therapy of Cancer: Methods and Protocols*; Hoffman, R. M., Ed.; Humana Press: New York, 2016.

(3) Felfoul, O.; Mohammadi, M.; Taherkhani, S.; de Lanauze, D.; Zhong Xu, Y.; Loghin, D.; Essa, S.; Jancik, S.; Houle, D.; Lafleur, M.; Gaboury, L.; Tabrizian, M.; Kaou, N.; Atkin, M.; Vuong, T.; Batist, G.; Beauchemin, N.; Radzioch, D.; Martel, S. Magneto-Aerotactic Bacteria Deliver Drug-Containing Nanoliposomes to Tumour Hypoxic Regions. *Nat. Nanotechnol.* **2016**, *11* (11), 941–947.

(4) Zheng, D.-W.; Chen, Y.; Li, Z.-H.; Xu, L.; Li, C.-X.; Li, B.; Fan, J.-X.; Cheng, S.-X.; Zhang, X.-Z. Optically-Controlled Bacterial Metabolite for Cancer Therapy. *Nat. Commun.* **2018**, *9* (1), 1680.

(5) Suh, S.; Jo, A.; Traore, M. A.; Zhan, Y.; Coutermarsh-Ott, S. L.; Ringel-Scaia, V. M.; Allen, I. C.; Davis, R. M.; Behkam, B. Nanoscale Bacteria-Enabled Autonomous Drug Delivery System (NanoBEADS) Enhances Intratumoral Transport of Nanomedicine. *Adv. Sci. (Weinheim, Baden-Wurttemberg, Ger.* **2019**, *6* (3), 1801309.

(6) Wei, B.; Pan, J.; Yuan, R.; Shao, B.; Wang, Y.; Guo, X.; Zhou, S. Correction to "Polarization of Tumor-Associated Macrophages by Nanoparticle Loaded Escherichia Coli Combined with Immunogenic Cell Death for Cancer Immunotherapy." *Nano Lett.* **2021**, *21* (13), 5905.

(7) Xing, J.; Yin, T.; Li, S.; Xu, T.; Ma, A.; Chen, Z.; Luo, Y.; Lai, Z.; Lv, Y.; Pan, H.; Liang, R.; Wu, X.; Zheng, M.; Cai, L. Sequential Magneto-Actuated and Optics-Triggered Biomicrorobots for Targeted Cancer Therapy. *Adv. Funct. Mater.* **2021**, *31* (11), 2008262.

(8) Chen, W.; Wang, Y.; Qin, M.; Zhang, X.; Zhang, Z.; Sun, X.; Gu, Z. Bacteria-Driven Hypoxia Targeting for Combined Biotherapy and Photothermal Therapy. *ACS Nano* **2018**, *12* (6), 5995–6005.

(9) Luo, C.-H.; Huang, C.-T.; Su, C.-H.; Yeh, C.-S. Bacteria-Mediated Hypoxia-Specific Delivery of Nanoparticles for Tumors Imaging and Therapy. *Nano Lett.* **2016**, *16* (6), 3493–3499.

(10) Chen, F.; Zang, Z.; Chen, Z.; Cui, L.; Chang, Z.; Ma, A.; Yin, T.; Liang, R.; Han, Y.; Wu, Z.; Zheng, M.; Liu, C.; Cai, L. Nanophotosensitizer-Engineered Salmonella Bacteria with Hypoxia Targeting and Photothermal-Assisted Mutual Bioaccumulation for Solid Tumor Therapy. *Biomaterials* **2019**, *214*, 119226.

(11) Yin, T.; Diao, Z.; Blum, N. T.; Qiu, L.; Ma, A.; Huang, P. Engineering Bacteria and Bionic Bacterial Derivatives with Nanoparticles for Cancer Therapy. *Small* **2022**, *18* (12), 2104643.

(12) Huang, X.; Pan, J.; Xu, F.; Shao, B.; Wang, Y.; Guo, X.; Zhou, S. Bacteria-Based Cancer Immunotherapy. *Adv. Sci.* **2021**, *8* (7), 2003572.

(13) Zhou, S.; Gravekamp, C.; Bermudes, D.; Liu, K. Tumour-Targeting Bacteria Engineered to Fight Cancer. *Nat. Rev. Cancer* **2018**, *18* (12), 727–743.

(14) Forbes, N. S. Engineering the Perfect (Bacterial) Cancer Therapy. *Nat. Rev. Cancer* **2010**, *10* (11), 785–794.

(15) Brown, J. M.; Wilson, W. R. Exploiting Tumour Hypoxia in Cancer Treatment. *Nat. Rev. Cancer* **2004**, *4* (6), 437–447.

(16) Duong, M. T.-Q.; Qin, Y.; You, S.-H.; Min, J.-J. Bacteria-Cancer Interactions: Bacteria-Based Cancer Therapy. *Exp. Mol. Med.* **2019**, *51* (12), 1–15.

(17) Din, M. O.; Danino, T.; Prindle, A.; Skalak, M.; Selimkhanov, J.; Allen, K.; Julio, E.; Atolia, E.; Tsimring, L. S.; Bhatia, S. N.; Hasty, J. Synchronized Cycles of Bacterial Lysis for in Vivo Delivery. *Nature* **2016**, *536* (7614), 81–85.

(18) Bourdeau, R. W.; Lee-Gosselin, A.; Lakshmanan, A.; Farhadi, A.; Kumar, S. R.; Nety, S. P.; Shapiro, M. G. Acoustic Reporter Genes for Noninvasive Imaging of Microorganisms in Mammalian Hosts. *Nature* **2018**, *553* (7686), 86–90.

(19) Chowdhury, S.; Castro, S.; Coker, C.; Hinchliffe, T. E.; Arpaia, N.; Danino, T. Programmable Bacteria Induce Durable Tumor Regression and Systemic Antitumor Immunity. *Nat. Med.* **2019**, *25* (7), 1057–1063.

(20) Deschênes, L.; Ells, T. Bacteria-Nanoparticle Interactions in the Context of Nanofouling. *Adv. Colloid Interface Sci.* **2020**, *277*, 102106.

(21) Hajipour, M. J.; Fromm, K. M.; Ashkarran, A. A.; Jimenez de Aberasturi, D.; de Larramendi, I. R.; Rojo, T.; Serpooshan, V.; Parak, W. J.; Mahmoudi, M. Antibacterial Properties of Nanoparticles. *Trends Biotechnol.* **2012**, *30* (10), 499–511.

(22) Miller, K. P.; Wang, L.; Benicewicz, B. C.; Decho, A. W. Inorganic Nanoparticles Engineered to Attack Bacteria. *Chem. Soc. Rev.* **2015**, *44* (21), 7787–7807.

(23) Reghu, S.; Miyako, E. Nanoengineered Bifidobacterium Bifidum with Optical Activity for Photothermal Cancer Immunotheranostics. *Nano Lett.* **2022**, *22* (5), 1880–1888.

(24) Yang, X.; Komatsu, S.; Reghu, S.; Miyako, E. Optically Activatable Photosynthetic Bacteria-Based Highly Tumor Specific Immunotheranostics. *Nano Today* **2021**, *37*, 101100.

(25) Yu, Y.; Yang, X.; Reghu, S.; Kaul, S. C.; Wadhwa, R.; Miyako, E. Photothermogenetic Inhibition of Cancer Stemness by Near-Infrared-Light-Activatable Nanocomplexes. *Nat. Commun.* **2020**, *11* (1), 4117.

(26) Chechetka, S. A.; Yu, Y.; Zhen, X.; Pramanik, M.; Pu, K.; Miyako, E. Light-Driven Liquid Metal Nanotransformers for Biomedical Theranostics. *Nat. Commun.* **2017**, *8* (1), 15432.

(27) Alberts, B.; Heald, R.; Johnson, A.; Morgan, D. . R. M. . W. W. N. *Molecular Biology of the Cell, 7th Edition*; New York, 2022.

(28) Kuhn, A. The Bacterial Cell Wall and Membrane-A Treasure Chest for Antibiotic Targets. *Subcell. Biochem.* **2019**, *92*, 1–5. https://doi.org/10.1007/978-3-030-18768-2_1.

(29) Wang, L.; Shen, Q.; Liao, H.; Fu, H.; Wang, Q.; Yu, J.; Zhang, W.; Chen, C.; Dong, Y.; Yang, X.; Guo, Q.; Zhang, J.; Zhang, J.; Zhang, W.; Lin, H.; Duan, Y. Multi-Arm PEG/Peptidomimetic Conjugate Inhibitors of DR6/APP Interaction Block Hematogenous Tumor Cell Extravasation. *Adv. Sci. (Weinheim, Baden-Wurttemberg, Ger.* **2021**, *8* (11), e2003558.

(30) Sun, X.; Yu, W.; Pang, Q.; Hu, T. Conjugation Reaction with 8-Arm PEG Markedly Improves the Immunogenicity of Mycobacterium Tuberculosis CFP10-TB10.4 Fusion Protein. *Bioconjug. Chem.* **2017**, *28* (6), 1658–1668.

(31) Lee, S.; Kim, K.; Kumar, T. S.; Lee, J.; Kim, S. K.; Lee, D. Y.; Lee, Y.; Byun, Y. Synthesis and Biological Properties of Insulin−Deoxycholic Acid Chemical Conjugates. *Bioconjug. Chem.* **2005**, *16* (3), 615–620.

(32) Kato, K.; Itoh, C.; Yasukouchi, T.; Nagamune, T. Rapid Protein Anchoring into the Membranes of Mammalian Cells Using Oleyl Chain and Poly(Ethylene Glycol) Derivatives. *Biotechnol. Prog.* **2004**, *20* (3), 897–904.

(33) Zhao, Y.; Fan, M.; Chen, Y.; Liu, Z.; Shao, C.; Jin, B.; Wang, X.; Hui, L.; Wang, S.; Liao, Z.; Ling, D.; Tang, R.; Wang, B. Surface-Anchored Framework for Generating RhD-Epitope Stealth Red Blood Cells. *Sci. Adv.* **2020**, *6* (12), eaaw9679.

(34) Becicka, W. M.; Bielecki, P. A.; Lorkowski, M. E.; Moon, T. J.; Zhang, Y.; Atukorale, P. U.; Covarrubias, G.; Karathanasis, E. The Effect of PEGylation on the Efficacy and Uptake of an Immunostimulatory Nanoparticle in the Tumor Immune Microenvironment. *Nanoscale Adv.* **2021**, *3* (17), 4961–4972.

(35) Veronese, F. M.; Mero, A. The Impact of PEGylation on Biological Therapies. *BioDrugs* **2008**, *22* (5), 315–329.

(36) Uher, O.; Caisova, V.; Hansen, P.; Kopecky, J.; Chmelar, J.; Zhuang, Z.; Zenka, J.; Pacak, K. Coley's Immunotherapy Revived: Innate Immunity as a Link in Priming Cancer Cells for an Attack by Adaptive Immunity. *Semin. Oncol.* **2019**, *46* (4–5), 385–392.

(37) Cossart, P.; Helenius, A. Endocytosis of Viruses and Bacteria. *Cold Spring Harb. Perspect. Biol.* **2014**, *6* (8).

(38) Kaiser, E.; Colescott, R. L.; Bossinger, C. D.; Cook, P. I. Color Test for Detection of Free Terminal Amino Groups in the Solid-Phase Synthesis of Peptides. *Anal. Biochem.* **1970**, *34* (2), 595–598.

(39) Ito, F.; Ernstoff, M. *Immune Checkpoint Inhibitors in Cancer, 1st Edition*; Elsevier: Amsterdam, Nederlands, 2018.

(40) De Sousa Linhares, A.; Battin, C.; Jutz, S.; Leitner, J.; Hafner, C.; Tobias, J.; Wiedermann, U.; Kundi, M.; Zlabinger, G. J.; Grabmeier-Pfistershammer, K.; Steinberger, P. Therapeutic PD-L1 Antibodies Are More Effective than PD-1 Antibodies in Blocking PD-1/PD-L1 Signaling. *Sci. Rep.* **2019**, *9* (1), 11472.

(41) André, M.; Besse, S.; Chezal, J.-M.; Mounetou, E. PEGylation Enhances the Tumor Selectivity of Melanoma-Targeted Conjugates. *Org. Biomol. Chem.* **2015**, *13* (2), 388–397.

(42) Suk, J. S.; Xu, Q.; Kim, N.; Hanes, J.; Ensign, L. M. PEGylation as a Strategy for Improving Nanoparticle-Based Drug and Gene Delivery. *Adv. Drug Deliv. Rev.* **2016**, *99* (Pt A), 28–51.

(43) Thomas, R. J.; Rockwell, B. A.; Marshall, W. J.; Aldrich, R. C.; Zimmerman, S. A.; Rockwell R. James, J. A Procedure for Multiple-Pulse Maximum Permissible Exposure Determination under the Z136.1-2000 American National Standard for Safe Use of Lasers. *J. Laser Appl.* **2001**, *13* (4), 134–140. https://doi.org/10.2351/1.1386796.

(44) Allison, R. R.; Moghissi, K. Photodynamic Therapy (PDT): PDT Mechanisms. *Clin. Endosc.* **2013**, *46* (1), 24–29. https://doi.org/10.5946/ce.2013.46.1.24.

(45) Martínez-Lostao, L.; Anel, A.; Pardo, J. How Do Cytotoxic Lymphocytes Kill Cancer Cells? *Clin. Cancer Res.* **2015**, *21* (22), 5047–5056.

(46) Goto, Y.; Iwata, S.; Miyahara, M.; Miyako, E. Discovery of Intratumoral Oncolytic Bacteria Toward Targeted Anticancer Theranostics. *Adv. Sci. (Weinheim, Baden-Wurttemberg, Ger.* **2023**, e2301679. https://doi.org/10.1002/advs.202301679.

Chapter 4 General Conclusion

GENERAL CONCLUSION

In recent years, cancer research has made enormous strides in comprehending the complexity of cancer biology, finding critical therapeutic targets, and providing innovative remedies. Nonetheless, cancer continues to be a significant health issue, and continued research efforts are crucial to furthering our knowledge about it and creating efficient cures. Furthermore, ongoing investment in research is required to create superior diagnostic equipment, enhance early detection, and offer patients with better drugs or remedies. The advent of innovative technological advances in cancer research has created new opportunities for comprehending cancer's biology and designing potential treatment options. Immunotherapy has shown remarkable results in harnessing the immune system to fight cancer cells, while developments in genetics have led to a clearer knowledge of the genetic mutations that drive the cancer's spread and proliferation.

The prevalence of cancer is increasing globally despite major advancements in research, prevention, and treatment making it a huge public health concern. Identifying novel therapeutic modalities that can selectively and accurately target cancerous cells while sparing normal cells, with increased specificity poses a significant challenge in cancer research. Tailored treatments that target cancer cells have significantly revolutionized the landscape of cancer therapy. The utilization of these therapies can lead to better patient results, decreased side effects, and a betterment in their overall quality of life. Chemotherapy is still an essential component of treatment in the current era and a key weapon in the struggle against this life-threatening condition. As more precise and personalized treatments become available, the use of chemotherapy may be scaled back or improved due to its associated side effects.

Bacteria therapy offers a major advantage in that as it can effectively target diseases while minimizing any adverse effects. A scientist named William Coley conducted pioneering research

with bacterial therapies and performed groundbreaking and controversial works on cancer and his legacy has an ongoing impact on this therapy. This therapy has demonstrated remarkable outcomes in recent studies, and many consider it to be a superior alternative to conventional cancer treatments like radiation and chemotherapy. By adopting this targeted approach, not only is the risk of adverse effects reduced, but the efficacy of the treatment is also enhanced. It has the added advantage of being able to fight against the growing problem of antibiotic resistance. Furthermore, bacteria can be genetically modified to generate certain drugs or proteins that strengthen their anti-cancer properties. While there are potential downsides, such as the requirement for precise monitoring of bacterial dosage and the possibility of bacterial resistance, the advantages of bacteria therapy over traditional cancer treatments remain significant. For instance, it can be used in conjunction with other treatments, such as chemotherapy and radiation, to boost their efficacy. If Coley had been allowed to continue his research into bacterial therapy, it is possible that his findings would have accelerated the acceptance of immunotherapy as a mainstream anticancer therapy.

Photothermal therapy (PTT) (which transforms light energy into thermal energy) is another area of active research in the field of cancer treatment. We obtained the optimal results by merging bacterial therapy with photothermal therapy and their combination offered several advantages such as excellent targeting, low cytotoxicity, excellent treatment efficacy, resulted in drastic tumor regression. Furthermore, we performed several chemical modifications on the bacteria utilized in this research to enhance their therapeutic effectiveness. Our findings suggest that these modifications can serve as a potent tool for optimizing bacterial therapy and augmenting its efficacy in treatment options.

The findings presented in Chapter 2 demonstrate that the bacteria can be modified without resorting to any genetic manipulation, but rather through a simpler method of altering the bacterial membrane, thereby increasing its efficiency. In this study, we performed a chemical modification of the anaerobic bacteria BB, which possesses intrinsic anticancer properties, by conjugating it with a photothermal agent, ICG and a formulation vehicle, CRE. This resulted in the development of a novel modified bacteria ICG-CRE-BB that exhibited excellent fluorescence properties, which was utilized for cancer therapeutics. This study demonstrates alternative methods for modifying bacteria without resorting to genetic manipulation, which effectively reduces the risk of creating virulent revertants. Furthermore, these methods have low cytotoxicity, making them a safer option for modifying bacteria. To summarize our findings in this chapter, our research provides evidence supporting the feasibility of utilizing biocompatible chemicals to chemically modify anaerobic bacteria as a foundation for cancer therapeutics. Likewise, this approach exhibits potential for further refinement and optimization, ultimately leading to its clinical application.

Monoclonal antibody-based cancer research is currently experiencing significant growth, with multiple recent breakthroughs. The findings presented in Chapter 3 showcase tumor regression using the application of the Anti PD-L1 in combination with anaerobic bacteria, RP, which has previously demonstrated impressive efficacy in selectively targeting cancer cells. After conducting a comprehensive screening process to evaluate various PPSBs for their fluorescence, toxicity, and photothermal conversion, RP emerged as the most promising candidate with exceptional results across all parameters. We were able to non-covalently attach Anti PD-L1 using BAM, onto the RP membrane, resulting in the generation of a modified RP that exhibited significantly improved anticancer efficacy. Our findings also showed that this modified RP was able to achieve faster tumor reduction.

In conclusion, our research about nanoengineering of bacteria has yielded promising results in demonstrating the potential of utilizing anaerobic and non-toxic bacteria to develop effective remedies for life-threatening diseases such as cancer, which continues to pose a major global challenge. In the current landscape of bacteria therapy research, the predominant focus has been on utilizing toxic bacteria such as *Salmonella*, *Listeria* and *Clostridium species* or genetically modified bacteria. However, our approach of chemical modification offers a unique perspective that has the potential to make a significant effect and potentially impactful departure from these prevailing methods, offering a new avenue for further exploration in the field of bacteria therapy. We believe that our approach to treatment, following advancements, holds an immense potential to serve as a transformative strategy in the development of advanced, next-generation anticancer therapeutics.

List of publications

LIST OF PUBLICATIONS RELATED TO THE THESIS

- **Sheethal Reghu**, Seigo Iwata, Satoru Komatsu, Takafumi Nakajo, and Eijiro Miyako, Cancer immunotheranostics using bioactive nanocoated photosynthetic bacterial complexes, **Nano Today**, 2023, 52-101966.
- **Sheethal Reghu** and Eijiro Miyako, Nanoengineered *Bifidobacterium bifidum* with Optical Activity for Photothermal Cancer Immunotheranostics, **Nano Letters**, 2022, (5), 1880-1888.

OTHER PUBLICATIONS

- Zhangyong Si, Jianguo Li, Lin Ruan, **Sheethal Reghu**, Ying Jie Ooi, Peng Li, Yabin Zhu, Paula T Hammond, Chandra S Verma, Guillermo C Bazan, Kevin Pethe, Mary B Chan-Park, Designer co-beta-peptide copolymer selectively targets resistant and biofilm Gram-negative bacteria, **Biomaterials,** 2023, 294, 122004.

- Chan-Jin Kim, Zhangyong Si, **Sheethal Reghu**, Zhong Guo, Kaixi Zhang, Jianghua Li & Mary B. Chan-Park, DNA-derived nanostructures selectively capture gram-positive bacteria, **Drug Delivery and Translational Research**, 2021 11, 1438–1450.

- Xi Yang, Satoru Komatsu, **Sheethal Reghu**, Eijiro Miyako, Optically activatable photosynthetic bacteria-based highly tumor specific immunotheranostics, **Nano Today**, 2021,37, 101100.

- Yue Yu, Xi Yang, **Sheethal Reghu**, Sunil C. Kaul, Renu Wadhwa and Eijiro Miyako, Photothermogenetic inhibition of cancer stemness by near-infrared-light-activatable nanocomplexes, **Nature Communications**, 2020, 11, 4117.

- Zheng Hou, Yang Wu, Chen Xu, **Sheethal Reghu**, Zifang Shang, Jingjie Chen, Dicky Pranantyo, Kalisvar Marimuth, Partha Pratim De, Oon Tek Ng, Kevin Pethe, En-Tang Kang, Peng Li, and Mary B. Chan-Park, Precisely Structured Nitric-Oxide-Releasing Copolymer Brush Defeats Broad-Spectrum Catheter-Associated Biofilm Infections *In Vivo*, **ACS Central Science**, 2020, 6, 2031-2045.

- Suresh Kumar Raman Pillai, **Sheethal Reghu**, Yogesh Vikhe, Hou Zheng, Chong Hui Koh, Mary B. Chan-Park, Novel Antimicrobial Coating on Silicone Contact Lens Using Glycidyl Methacrylate and Polyethyleneimine Based Polymers, **Macromolecular Rapid Communications**, 2020, 41, 2000175.

- **Sheethal Reghu**, Hui You, Kalaivani Seenivasan, Shun Nishimura, Toshiaki Taniike, and Eijiro Miyako, Design and Control of Bioinspired Millibots, **Advanced Intelligent Systems**, 2020, 2, 2000059.

- Guangmin Wei, Diep Nguyen, **Sheethal Reghu**, Jianghua Li, ChunSong Chua, Yoshiki Ishida, and Mary B. Chan-Park, Fast-Bactericidal Effect of Polyion Complex Nanoparticles on Gram-Negative Bacteria, **ACS Applied Nano Materials,** 2020, 3, 2654−2664.

- Zhangyong Si, Hui Wen Lim, Moon Y. F. Tay, Yu Du, Lin Ruan, Haofeng Qiu, Rub& Zamudio-Vazquez, **Sheethal Reghu**, Yahua Chen, Wen Shuo Tiong, Kalisvar Marimuthu, Partha Pratim De, Oon Tek Ng, Yabin Zhu, Yunn-Hwen Gan, Yonggui Robin Chi, Hongwei Duan, Guillermo C. Bazan, E. Peter Greenberg, Mary B. Chan-Park and Kevin Pethe, A glycosylated cationic block poly(beta-peptide) reverses intrinsic antibiotic resistance in all ESKAPE Gram-negative bacteria, **Angewandte Chemie.** 2020, 59, 6819 – 6826**.**

- Kaixi Zhang, Yu Du, Zhangyong Si, Yang Liu, Michelle Turvey, Cheerlavancha Raju, Damien Keogh, Lin Ruan, Subramanion Jothy, **Sheethal Reghu**, Kalisvar Marimuthu, Partha De, Oon Tek Ng, José Mediavilla, Barry Kreiswirth, Yonggui Robin Chi, Jinghua Ren, Kam Tam, Xuewei Liu, Hongwei Duan, Yabin Zhu, Yuguang Mu, Paula Hammond, Guillermo Bazan, Kevin Pethe, and Mary Chan-Park, Enantiomeric glycosylated cationic block co-beta-peptides eradicate *Staphylococcus aureus* biofilms and antibiotic-tolerant persisters, **Nature Communications,** 2019, 10, 4972.

- Yuan Xu, Kaixi Zhang, **Sheethal Reghu**, Yichao Lin, Mary B. Chan-Park, and Xue-Wei Liu, Synthesis of Antibacterial Glycosylated Polycaprolactones Bearing Imidazoliums with Reduced Hemolytic Activity, **Biomacromolecules**, 2019, 20 (2), pp 949–958.

International conferences

- Sheethal Reghu and Eijiro Miyako, Chemically modified *Bifidobacterium bifidum* for cancer immunotheranostics using photothermal therapy. 2022 MRS Fall Meeting & Exhibit | Boston, Massachusetts, U.S., November 27 – December 2, 2022.

Awards and grants

- Monbukagakusho (MEXT) Scholarship for Doctoral Study by the Japanese Government; Issued by Ministry of Education, Culture, Sports, Science and Technology, Japan (October 2020 to September 2023).

- JAIST Foundation Research Grant for Students for attending conference (year 2022).

Acknowledgements

I would like to express my sincere gratitude to everyone who has contributed to the successful completion of my doctoral thesis.

First and foremost, I would like to extend my heartfelt appreciation to my supervisor Prof. Dr. Eijiro Miyako, who has been an invaluable guide and mentor throughout my doctoral research. His unwavering support, expertise, and encouragement have been instrumental in shaping my research direction and helping me overcome the challenges that came along the way.

I am also deeply thankful to my second supervisor Prof. Dr. Kazuaki Matsumura and minor supervisor Prof. Dr. Toshifumi Tsukahara, whose valuable insights, constructive feedback, and technical expertise have been invaluable in shaping my research direction and helping me navigate the challenges of doctoral research.

I am also deeply grateful to the members of my lab who have supported me through their valuable discussions, feedback, and technical assistance. Their constructive criticism and helpful suggestions have played a crucial role in shaping my research and pushing me to pursue excellence. I am grateful to the MEXT scholarship for supporting me with a scholarship throughout my doctoral studies.

I am also grateful to my friends who have been a constant source of motivation, support, and encouragement, particularly during challenging times. Their belief in me has been a source of strength and inspiration, and I cannot thank them enough.

Last but not least, I am deeply indebted to my family, husband, parents and my sister, whose support, and encouragement have been the foundation of my academic pursuits. Their unwavering support and understanding have been a constant source of motivation, and I could not have reached this milestone without them.

Finally, I would like to express my appreciation to everyone else who has supported me in any way throughout my academic journey. Your support has been instrumental in making this thesis a reality, and I am deeply grateful.

ACS Publications
Most Trusted. Most Cited. Most Read.

Nanoengineered Bifidobacterium bifidum with Optical Activity for Photothermal Cancer Immunotheranostics

Author: Sheethal Reghu, Eijiro Miyako

Publication: Nano Letters
Publisher: American Chemical Society
Date: Mar 1, 2022

PERMISSION/LICENSE IS GRANTED FOR YOUR ORDER AT NO CHARGE

This type of permission/license, instead of the standard Terms and Conditions, is sent to you because no fee is being charged for your order. Please note the following:

- Permission is granted for your request in both print and electronic formats, and translations.
- If figures and/or tables were requested, they may be adapted or used in part.
- Please print this page for your records and send a copy of it to your publisher/graduate school.
- Appropriate credit for the requested material should be given as follows: "Reprinted (adapted) with permission from {COMPLETE REFERENCE CITATION}. Copyright {YEAR} American Chemical Society." Insert appropriate information in place of the capitalized words.
- One-time permission is granted only for the use specified in your RightsLink request. No additional uses are granted (such as derivative works or other editions). For any uses, please submit a new request.

If credit is given to another source for the material you requested from RightsLink, permission must be obtained from that source.

BACK CLOSE WINDOW

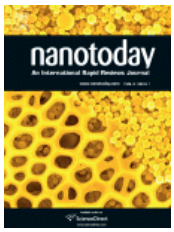

Cancer immunotheranostics using bioactive nanocoated photosynthetic bacterial complexes

Author: Sheethal Reghu,Seigo Iwata,Satoru Komatsu,Takafumi Nakajo,Eijiro Miyako

Publication: Nano Today

Publisher: Elsevier

Date: October 2023